A MULTI-PHYSICS PLANNING PARADIGM FOR ROBOT ASSISTED ORTHOPAEDIC SURGERY

by

Amirhossein Farvardin

A dissertation submitted to The Johns Hopkins University in conformity with the requirements for the degree of Doctor of Philosophy.

Baltimore, Maryland

October, 2020

Abstract

Osteoporosis or severe reduction in bone mineral density is a disease that primarily affects elderly people. Osteoporotic hip fracture rates increase exponentially with age in both men and women. In addition to the high mortality rate for those sustaining such fractures, less than half of the survivors return to their pre-fracture status concerning the quality of daily living. Augmentation of the proximal femur with Polymethylmethacrylate (PMMA) bone cement (femoroplasty) has been identified as a potential preventive approach to reduce the risk of fracture. Femoroplasty, however, is associated with a risk of thermal damage as well as the leakage of cement or blockage of blood supply when large volumes of PMMA are introduced inside the bone. Several recent studies have proposed injection strategies to reduce the injection volume in simulations. This thesis describes the methods and tools developed for multi-physics planning and the execution of femoroplasty. To this end, computational models are developed to simulate how bone augmentation affects the biomechanical properties of the bone. These models are used to plan femoropasty for ca-

daveric specimens and showed the superiority of planned-based augmentation over generic injection strategies. Experimental tests confirmed the findings of simulations and showed a significant increase in fracture-related biomechanical properties of the augmented compared to those left intact. In addition to biomechanical studies for femoroplasty, a heat-transfer model was developed to estimate bone temperatures during augmentation. Furthermore, a curved injection strategy was introduced and validated in simulations. These developments and modeling capabilities can be extended to various augmentation surgeries including vertebroplasty and core decompression.

ABSTRACT

Primary Reader and Advisor:

Mehran Armand, PhD

Research Professor of Mechanical Engineering

Johns Hopkins University

Secondary Readers:

Russell H. Taylor, PhD

John C. Malone Professor of Computer Science

Johns Hopkins University

Iulian Iordachita, PhD

Research Professor of Mechanical Engineering

Johns Hopkins University

Juluis K. Oni, MD

Assistant Professor of Orthopaedic Surgery

Johns Hopkins Medical Institutions

Acknowledgments

I would like to express my deepest appreciation to my adviser and mentor, Dr. Mehran Armand. It was for him that I had the opportunity to work with some of the most brilliant minds in the field of computer-assisted surgery. This work would not have been possible without his endless support, guidance, and patience throughout my years as a graduate student.

Sincere thanks to Dr. Russell Taylor of Computer Science, Dr. Iulian Iordachita of Mechanical Engineering, and Dr. Juluis Oni of Orthopaedic Surgery from whom I have learned a lot, either in classes or research meetings. They have also graciously taken the time to read this dissertation and be on my defense committee.

Special thanks to Mahsan Bakhtiarinejad, Dr. Ehsan Basafa, Dr. Hao Liu, Dr. Ryan Murphy, and Cong Gao, who closely collaborated with me and contributed to many aspects of this project. I'd also like to thank the current and former lab-mates—Dr. Robert Grupp, Dr. Farshid Alambeigi, Dr. Shahriar Sefati, Joshua Liu, Henry Phalen, Wei-lun Huang, Alireza Chamani, and Justin

ACKNOWLEDGMENTS

Ma—for putting up with me in the lab and working through questions whenever I had them.

Many thanks go to Dr. Stephen Belkoff and Mr. Demetries Boston of Johns Hopkins Bayview Medical Center for their help with cadaveric experiments and CT scans. Special thanks to administrative staff: Mike Bernard and Kevin Adams of the Department of Mechanical Engineering, and Lorrie Dodd, Alison Morrow, Ashley Moriarty, and Jordan Card of Laboratory for Computational Sensing and Robotics (LCSR).

I am also grateful to the many wonderful friends I met during my journey at Johns Hopkins. I truly enjoyed their company and support. Special thanks to Dr. Sina Youssefian and Ali Ebrahimi for all of our fruitful discussions during coffee breaks. I would also like to extend my thanks to all my non-JHU friends whose names would span pages.

Last but absolutely not least, I thank my wonderful parents for their unconditional love, support, and sacrifice. Thanks to my sister, Nahal for being my best friend since day one, and to my cousin Ghazal who made my stay in Baltimore feel like home.

Amirhossein Farvardin

October 2020

Dedication

To Dr. Fereidoon Farvardin

Contents

Abstract **ii**

Acknowledgments **v**

List of Tables **xiii**

List of Figures **xiv**

1 Introduction **1**

1.1 Motivation 1

1.2 Objectives and Scope 2

1.3 Thesis Overview 3

1.4 Contributions 4

2 Background **6**

2.1 Osteoporosis and Hip Fractures 6

2.1.1 The Burden of Disease 6

2.2 Assessments and Treatments 8
2.2.1 Fracture Mechanism 9
2.3 Femoroplasty 11
2.3.1 First-generation Studies 11
2.3.2 Second-generation Studies 12
2.4 Computer-assisted
Orthopaedic Surgery 18
2.5 Robot-Assisted System Overview 20

3 Significance of Preoperative Planning for Femoroplasty 23

3.1 Introduction 23
3.2 Methods 25
3.2.1 Plan-based injection 25
3.2.2 Generalized Injection Strategies 30
3.2.3 Biomechanical Evaluation
and Data Analysis 31
3.3 Results 33
3.4 Discussion 37
3.5 Recapitulation of Contributions 40

4 Experimental Evaluation of the Planned Injections 42

4.1 Introduction 42

4.2 Methods 43
4.2.1 pre-operative Planning Paradigm 43
4.2.2 Navigation System 47
4.2.3 Cement Injection
and Temperature Measurement 48
4.2.4 Post-operative Mechanical Testing
and Data Analysis 51
4.3 Results 53
4.4 Discussion 60
4.5 Conclusion 63
4.6 Recapitulation of Contributions 64

5 Heat Transfer Analysis for Femoroplasty 65

5.1 Introduction 65
5.2 COMSOL Simulations 67
5.2.1 Model Validation 69
5.2.2 Discussion 72
5.3 Conductive Cooling Scheme 73
5.3.1 Geometrical Modeling
and FE Simulations 75
5.3.2 Sawbone Experiment 77
5.3.3 Results and Discussion 79

5.4 Conclusion 84

5.5 Recapitulation of Contributions 85

6 Curved Injection Paths **87**

6.1 Motivation 87

6.2 Methods 88

6.2.1 Optimization of the Injection Trajectory and Rate 88

6.2.2 Data Analysis and Validation 91

6.3 Results and Discussion 92

6.4 Conclusion 95

6.5 Recapitulation of Contributions 96

7 Large Deflection Shape Sensing **97**

7.1 Introduction 97

7.2 Shape Sensing Approach 101

7.2.1 Design Concept 101

7.2.2 Shape Sensing Scheme 103

7.2.3 Modeling 107

7.2.4 Shape Sensor Assembly 108

7.2.5 Sensor Calibration 109

7.2.6 2D Shape Reconstruction 110

7.2.7 Shape Sensing Scheme of CDM 111
7.2.8 Sensor Calibration inside the CDM 112
7.2.9 Results and Error Analysis 113
7.3 Dynamic Shape Tracking 115
7.3.1 Experimental Platform 115
7.3.2 Case I: Free Bending 116
7.3.3 Case II: Bending with an Obstacle 117
7.3.4 Case III: Bending with a Tool 118
7.3.5 Data Analysis 119
7.4 Results 119
7.5 Discussion 122
7.6 Conclusion 125
7.7 Recapitulation of Contributions 126

8 Conclusion **127**
8.1 Summary 127
8.2 Limitations and Future Work 128

Bibliography **131**

Vita **152**

List of Tables

2.1 Summary of the published second generation experimental studies on femoroplasty 17

4.1 Sample demographics– Neck T-scores and BMD were obtained from DEXA Scanning. The Neck T-scores and BMDs are reported for both the limb to be augmented and the control side. 46
4.2 Results of femoroplasty: YL and ML represent the yield load and maximum load in N, respectively, and YE and ME represent the yield energy and maximum energy in Joules, respectively. Moreover, “Pre”, “Plan”, and “Post” represent the FE analysis based on the pre-operative CT, virtual CT created from the plan, and post-operative CT, respectively. 55
4.3 Recorded temperature of the bone at the depth of 2mm from the surface at three anatomical regions. For the regions with potential risk of necrosis, exposure time of the temperature-rise was reported as well. 59

5.1 Material properties of the bone used in FE simulations 68
5.2 Maximum temperature-rise of the bone at discrete time-intervals following PMMA injection 71
5.3 Summary of the material properties involved in cooling simulations 77

6.1 Sample demographics and predicted yield load of the selected femora for augmentation. 88

7.1 Summary of tip tracking results for all experimental groups. . . . 120

List of Figures

2.1 Healthy (left) vs osteoporotic (right) femur. Deterioration of bone micro-structure is evident in neck and trochanter region of the osteoporotic bone. 8
2.2 Representative anteroposterior (AP) radiograph of a proximal femur showing second-generation injection strategies 15
2.3 Overview of the main system components for femoroplasty 19
2.4 Overview of the Robot-assisted system components for femoroplasty 21
2.5 An integrated Drilling and Injection Component (DIC) designed for Robot-assisted Femoroplasty 22

3.1 Distribution of the Young's elastic modulus in the critical region of the femur. 28
3.2 Schematic of the optimized injection pattern by BESO (green), practical injection volume (blue) and line of injection (red). 29
3.3 (A) Schematic of the optimized injection pattern by BESO, (B) the matching spheroids (blue rings) and (C) line of injection with corresponding results of the SPH simulation (blue). 30
3.4 Generalized injection strategies: a) Single central (V1; Red), b) main compression bridge (V2; Blue) and c) compression bridge to the lower part of the femoral head (V3; yellow). 31
3.5 Boundary conditions simulating a side-way fall on greater trochanter. 33
3.6 SPH results of generalized injection strategies (a) the single central mesh of the specimen 1 with diffused volume of cement in different variations of the generalized injection strategies: The single central (V1; Blue), main compression bridge (V2; Blue) and compression bridge to the lower part of the femoral head (V3; yellow). 34

3.7 FE mesh of the femur specimens with the optimized injection patterns after hydrodynamic simulation. Cement volumes were constrained and initially located based on the modified method of BESO 35
3.8 Percentage of the yield load increase normalized to the non-augmented state of the same specimen. 36
3.9 Percentage of the yield energy increase normalized to the non-augmented state of the same specimen. 36

4.1 Schematic of the optimized injection pattern by FE using BESO method (green) and the injection blobs defined by the planning paradigm (Blue) 47
4.2 (A) Intra-operative system for drilling navigation, (B) An automatic injection device for bone cement delivery into the planned region, (C) Predetermined points for initial registration (top) and surface points used for ICP registration (bottom). 49
4.3 Thermocouple placement for temperature measurements. Note that k-type thermocouples recorded the temperature at one second interval and depth of 2mm from the surface on trochanteric crest (TC1; red), the greater trochanter (TC2; blue), and femoral neck (TC3; black) 51
4.4 Experimental set-up simulating a fall on the greater trochanter using MTS machine (Bionix 858 Test System, Eden Prairie, Minnesota) 52
4.5 Representative force-displacement curve used to determine the yield and maximum energy and their corresponding energies . . 53
4.6 Measured vs. Predicted yield loads. The overall correlation coefficient is 0.77. 56
4.7 Effects of augmentation on yield and maximum load (left), yield and maximum energy (right) of the osteoporotic specimens measured in fracture tests. Error bars represent standard deviation. 57
4.8 Patterns of fracture in side-way fall loading condition for A) Sample 1 from the control group, B) Sample 6 from the control group, C) Sample 6 of the augmented group; D) Sample 3 (osteopenic specimen). Note that the control samples experience an intertrochanteric fracture while the fracture pattern varies in the augmented group. 58

5.1 Segmented geometries of the bone and PMMA (left) FE mesh of the bone geometry (right). Note that the FE mesh was created using the largest mesh size that would produce the converging results. 68

5.2 Surface temperature-rise of the femur during PMMA Polymerization. 70
5.3 Surface Temperature-rise of the Second femur specimen for the first 1000 seconds after the injection- Experimental results vs. predicted values. 71
5.4 Schematic Illustration of the proposed cooling system. In the first step (left), bone cement is injected through the planned path and then K-wire attached to the ice-water bath is inserted in the drilled tunnel right after the injection (right). 75
5.5 3D Geometrical and FE mesh of the femur with segmented PMMA and k-wire 77
5.6 Cooling Experimental Setup 78
5.7 Predicted temperature of the specimen 1 for the first 3000 seconds after injection with and without the cooling 79
5.8 Simulated maximum temperature with cooling vs. without cooling 80
5.9 Temperature distribution of the femoral bone during PMMA polymerization with (top) and without (bottom) the cooling. 81
5.10 X-ray images of PMMA profile inside the open cell foam block (Sawbone) without cooling(top) vs. with cooling (bottom) 82
5.11 Temperature-rise measurement of the 3 thermocouples at sawbone cement interface with cooling vs. without cooling 83

6.1 Sagittal (left) and axial (right) view of FE mesh with desired cement elements (green) selected based on the method of BESO. . . 89
6.2 Overview of the optimization algorithm: Creating an isosurface of the cement elements from BESO (a), Dividing the cement volume into regions (b), finding the center points (c), initiating the optimization algorithm to find injection rates (d), and final drill trajectory and injection volume (e). 90
6.3 Bone yield load before and after injection. 93
6.4 Results of the optimization convergence for sample 1 (left) and 2 (right). 93
6.5 Sagittal (a) and axial (b) of SPH Results after cement injection for sample 3. 94
6.6 Curved-drilling of the proximal femur using a cable-driven CDM 95

7.1 The (a) osteolysis and (b) CDM with a tool through screw hole on acetabular cup. 98
7.2 Sensor configuration for larger curvature detection. 102
7.3 Strategy to reduce the range of wavelength shift by increasing the center distance between nitinol wires (L1 $>$ L2) a) reduced wavelength shift and b) larger wavelength shift. 104

7.4 Shape sensing for osteolysis dexterous manipulator. 105
7.5 The (a) Parallel nitinol wires and (b) whole assembly under microscope. 108
7.6 Calibration board for 2D Shape Sensor Array. 109
7.7 Calibration board for 2D Shape Sensor Array. 110
7.8 Arrangement of the FBG sensors for Shape reconstruction. 112
7.9 Shape sensing with constant curvature bending. 113
7.10 Wavelength shift for different curvatures, calibration (blue) and verification (red). 114
7.11 Overall view of the experimental setup. 116
7.12 Free bending configuration of the CDM at 2 mm cable displacement. 117
7.13 CDM bending configurations at 2.0 mm cable displacement in free bending (left), and bending in the presence of an obstacle. . . 118
7.14 CDM bending configuration in a presence or a torque coil inside its lumen. 118
7.15 This figure shows (a) Comparison of shape sensing trajectory with the trajectory extracted from images in free bending, (b) bending with an obstacle (Figure 7.13), and (c) bending with a tool. 121
7.16 Tip position on the x-axis (a) and y-axis (b)-free bending case at 0.75 mm/s cable displacement rate. 122

Chapter 1

Introduction

1.1 Motivation

Osteoporosis is a widespread disease, affecting over 75 million people and is associated with the risk of fracture [1]. In the case of vertebral and hip fractures, incidence increases exponentially with advancing age [2]. The worldwide occurrence of osteoporotic hip fractures is estimated to increase from 1.7 million in 1990 to 6.3 million in 2050 [3]. The mortality rate within one year of these fractures is between 14% to 58%, depending on the report [4–7]. Moreover, only 60% of the patients who have suffered from an osteoporotic hip fracture recover to their previous level of walking [8]. These patients are 6-10 times more likely to sustain a second fracture [9] and can benefit greatly from a preventive treatment. Current treatments (i.e. antiresorptive drug usage),

however, are only effective in the long term. Femoroplasty or augmentation of bone strength by injecting Polymethylmethacrylate (PMMA) is a potential treatment option to reduce the risk of such injuries. Several previous studies have investigated the biomechanical benefits of femoroplasty in an established biomechanical model mimicking a fall on the greater trochanter [10–16]. Most of these studies showed an increase of the fracture-related biomechanical properties as the result of augmentation. However, femoroplasty is associated with complications such as bone surface temperature-rise that needs to be addressed before it becomes a clinical procedure. An efficient biomechanically-guided planning paradigm, along with a robot-assisted execution system can benefit patients at the highest risk of hip fractures.

1.2 Objectives and Scope

The research presented in this document aims to develop new methodologies and tools that improve the outcome of femoroplasty. In particular, we aim to investigate whether the additional computational overhead of the patient-specific planning can significantly improve the bone strength as compared to the generalized injection strategies attempted in the literature. Next, we aim to validate the outcome of the new planning paradigm via direct experiments that evaluates the biomechanical benefits of the plan as well as bone surface

temperatures. The next aim was to introduce heat-transfer modeling and cooling solutions to address the risk of thermal damage associated with femoroplasty. The final objective is to develop robotic technologies for a more accurate execution of the planned injection. In addition, we propose other novel approaches that have the potential to promote efficiency and safety of femoroplasty and other orthopaedic surgeries.

1.3 Thesis Overview

Chapter 2 provides a brief background about osteoporosis, hip fractures, current treatment options and efforts to prevent those fractures including patient-specific and generalized injection strategies. It then provides an overview of the current system developed for intra-operative navigation and assessment of femoroplasty.

Chapter 3 describes development of a novel pre-operative planning paradigm for bone augmentation using Finite Element (FE) modeling and structural optimization algorithms. Computer simulations were used to evaluate the biomechanical efficiency of this plan against generic approaches previously proposed in the literature.

In Chapter 4, we investigate the efficacy of the proposed planning paradigm through direct cadaveric experiments in which both the biomechanical testing

and temperature measurements evaluate the safety and efficacy of augmentation.

Chapter 5 is dedicated to describing the heat transfer model developed to estimate bone temperature-rise after femoroplasty. Previously measured bone temperatures are used for model validation. Furthermore, a conductive cooling scheme is introduced to lower the risk of thermal damage.

Chapter 6 presents a new planning paradigm for femoroplasty based on injection patterns that are achieved with curved-drilling.

Chapter 7 focuses on development of a novel large curvature detecting Shape Sensor Array (SSA) of a continuum manipulator for Orthopaedic surgery. It presents the conceptual design, SSA modeling, assembly, calibration and real-time shape sensing results.

Chapter 8 offers a summary and conclusion of this work as well as some limitations. It also provides brief recommendations for future research in this area.

1.4 Contributions

The author's contributions in the presented work include:

- Development of a planning paradigm for patient-specific femoroplasty. The planing paradigm combines the structural optimization with a gra-

dient descent optimization that matches the FE pattern with realistic injection blobs. Simulation results showed the superiority of the plan over generic injection strategies and previously customized plans.

- Performing augmentation experiments, based on pre-operative plans, on cadaveric femur specimens with osteoporosis and osteopenia and analysis of the results including bone surface temperatures and fracture tests. Mechanical testing results showed close agreements with those of simulations.

- Development of a heat transfer FE model to estimate bone surface temperatures. Preliminary experimental results showed agreement between measurements and simulation predictions.

- Development of a novel shape sensor for large deflection shape sensing of a dexterous continuum manipulator used in orthopaedic surgery. Tip tracking accuracy of the manipulator was evaluated in different environments which showed sufficient accuracy for its immediate application.

Chapter 2

Background

2.1 Osteoporosis and Hip Fractures

2.1.1 The Burden of Disease

Osteoporosis is a major health concern, affecting over 75 million people and is associated with the risk of fracture [1]. In the case of vertebral and hip fractures, the incidence rate increases exponentially with advancing age, while that of wrist fractures levels off after the age of 60 years [17]. An estimated 1.3-1.7 million hip fractures occurred worldwide in 1990 [3, 18]. As the life expectancy of the world population increases, the World Health Organization (WHO) predicts that this number will rise to 3 million by 2025 [19]. The 1-year mortality rate for those sustaining a hip fracture is between 14%-58%,

depending on the report [4–7]. Moreover, only 60% of the patients who have suffered from an osteoporotic hip fracture recover to their previous level of walking [8].

While most hip fractures occur as the result of a fall, some may occur spontaneously when the bone density is significantly lower than the healthy levels. The lifetime risk of hip fractures is estimated to be 8.1% and 19.5% in men and women respectively, assuming that all survive to the current average life expectancy [20]. Estimates increase to 11.1% and 22.7% if calculated based on predicated mortality rates (increase in life expectancy in the future) [20]. It is important to note that a previous hip fracture increases the risk of fracture for the second hip (contralateral hip) are 6-10 times more likely to occur in patients who have already suffered from a hip fracture [9, 21].

Nearly all hip fractures result in hospitalization with a mean hospital stay of 30 days. In the United Kingdom, the number of hospital bed-days for hip fracture is similar to those of breast cancer and cardiovascular disease [22, 23]. In the United States, approximately 20% of hip fracture patients require long-term care in a nursing home [24].

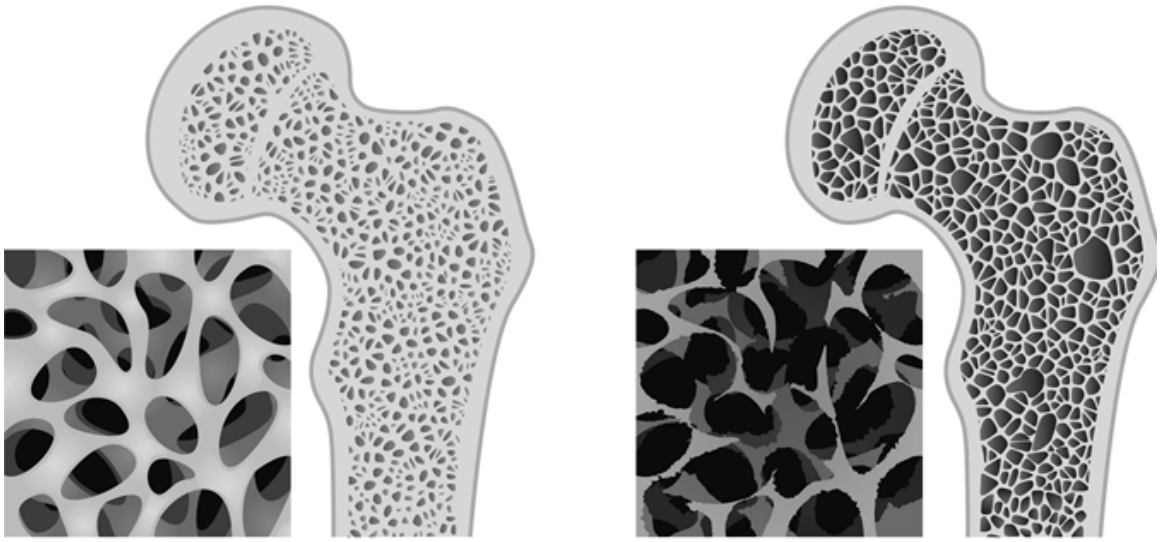

Figure 2.1: Healthy (left) vs osteoporotic (right) femur. Deterioration of bone micro-structure is evident in neck and trochanter region of the osteoporotic bone. Image from http://orthopedicsurgerysandiego.com/cardiovascular-disease-increases-the-risk-of-hip-fractures.

2.2 Assessments and Treatments

By definition, osteoporosis is having a bone mineral density (BMD) of 2.5 standard deviations or more below that of average for healthy, young adults (T-score of -2.5 or less). This can be determined by Dual-Energy X-ray Absorptiometry (DEXA) scanning of the bone. Patients with osteopenia, or low BMD, have a BMD between 1 and 2.5 standard deviations below average. Numerous factors affect our ability to build and retain BMD. These factors include but not limited to gender, race, hormonal factors, nutrition, physical activity, and lifestyle behaviors [25]. In recent decades, several studies have focused on osteoporosis treatment and some studies have resulted in the development of an-

tiresorptive drugs such as estrogens, calcitonin, and bisphosphonates [26–30]. These drugs, however, can have long-term effects and are not effective in the short-term. While the combination of early diagnosis and prescription of these drugs could lead to a lower risk of future fractures, such treatments are not sufficient for elderly at the highest risk. In one study Courtney et al. has shown that an increase in femoral neck BMD of more than 20% would be required to prevent fracture [31]. This increase requires years if not decades of antiresorptive drug usage.

Another preventive measure proposed for the patients at the highest risk is the use of mechanical devices such as hip protectors. In studies of nursing home patients, the use of hip protectors has reduced the incidence of hip fractures [32–34]. Meanwhile, due to their high cost and difficult to apply mechanical designs, hip protectors are not widely used outside of the nursing home settings [35]. Therefore, an effective therapeutic approach to prevent osteoporotic hip fractures immediately can be significantly advantageous, especially for patients who have already sustained a fracture.

2.2.1 Fracture Mechanism

The femur fracture is a complex phenomenon and depends on several factors including bone geometry, degree of bone loss as a result of osteoporosis or osteopenia, and loading conditions. Reportedly, more than 90% of hip fractures

were caused by falls from standing heights [36, 37]. Pinilla et al. [38] investigated the influence of loading direction on bone strength through compression testing of the cadaveric femora and showed that impact direction is a critical determinant of hip fracture risk. Similar studies have aimed to study the effects of bone loading conditions using both linear (e.g. [39, 40]) and nonlinear (e.g. [41]) FE analysis. Bessho et al. [41] showed that the loading condition simulating a fall in the posterolateral direction is smaller than that of a fall in the lateral direction. These results are valuable in developing effective treatments to prevent femur fractures.

In some cases, low BMD can cause a bone (e.g. proximal femur or vertebral segments) to fracture during normal daily activities without falling or even sustaining a significant load [35, 42]. These cases are often associated with severe osteoporosis when the bone has lost its ability to remodel. Remodeling is a phenomenon that helps the healthy bone adapt its structural density to best carry the loads while keeping its weight at a minimum [42, 43]. In a recently published study, Varga et al. [44] proposed treatment strategies based on this phenomenon which is further discussed in Chapter 3.

2.3 Femoroplasty

Augmentation of the proximal femur with Polymethylmethacrylate (PMMA) bone cement, also known as femoroplasty, has been identified as a potential preventive approach to reduce the risk of fracture. Over the past two decades, several research groups have presented various prophylactic augmentation strategies for the osteoporotic proximal femur. The overall procedure involves drilling a cannula path along the femoral neck region and injecting the liquid bone cement while retracting the cannula. The neck and greater trochanter regions of the proximal femur are injected with sufficient bone cement to strengthen the bone against falls.

2.3.1 First-generation Studies

In the first-ever femoroplasty study, Heini et al. showed that gross filling of the proximal femur with 28-40 ml of PMMA increases both fracture load (+82%) and fracture energy (+188%) of the bone [10]. Using 50 ml of PMMA, de Bakker showed an increase of 24% and 84% for the fracture load and fracture energy, respectively [45]. Beckmann et al. used a composite material (Cortoss Orthovita) that releases less heat and showed comparable strengthening results (43% and 187%, respectively) using 40 ml of cement and demonstrated, for the first time, the feasibly of revision surgery in case of fracture

after augmentation [46]. Sutter et al. achieved similar results using 40-50 ml of PMMA bone cement (Spineplx, Stryker, Kalamazoo, MI, USA) [47]. While the first generation of femoroplasty studies established the biomechanical benefits of femoroplasty, various issues regarding the clinical use of femoroplasty were not addressed in these studies [47]. Of note, all first-generation studies involved high volume injection of bone cement in the neck and intertrochanter regions of the proximal femur.

2.3.2 Second-generation Studies

Following the first-generation studies, the biological risks related to the large cement volumes were realized [44]. In particular, it was realized that the gross filling of the proximal femur with PMMA may introduce the risk of thermal necrosis and other complications such as leakage or blockage of the blood support [48, 49]. Therefore, in the second generation femoroplasty studies, researchers focused on reducing the overall volume of the injection. In the study of Sutter et al. [11], 15 ml injection of PMMA into the trochanteric or femoral neck region resulted in no biomechanical advantages. Moreover, no significant difference was found between the fracture patterns of the two injection scenarios. Van der Steenhoven [50] studied the effects of two minimally invasive Elastomer Femoroplasty (EF) techniques on femur strength and their ability to prevent fracture displacements. Fracture results showed

no significant increase in femur strength. However, measured displacements suggested that EFs can stabilize the proximal femur by restoring hip geometry. Beckmann et al. [12] achieved improvements in biomechanical properties of the femora when they used a single drilling approach, but injection strategies with double drilling paths resulted in a non-significant difference, or lower fracture load and energy. Fliri et al. [51] investigated the biomechanical potential of V-shaped injection configurations targeting the superior and inferior aspects of the femoral neck in an in-vitro study and showed that such patterns that result in 124% more energy absorption before fracture.

In contrast to generic injection approaches, our lab has developed a patient-specific planning strategy for femoroplasty. Basafa et al. [15] reported the results of computational planning and optimization of the procedure for biomechanical evaluation. In simulations, it was shown that by introducing less than 10 ml of bone cement into the femur (substantially less than the 40–50 ml volumes used in previous experimental studies [10–12]), it is possible to increase the yield load of the femur specimens by over 30% [15]. This planning paradigm which is based on a modified method of Bi-directional Evolutionary Structural Optimization (BESO) was evaluated on eight pairs of osteoporotic femur specimens and achieved significant biomechanical benefit with an average injection volume of 9.5($\pm$1.7) ml of PMMA [16].

One of the main elements of an effective plan relies on, among others, is an

accurate prediction of how bone cement diffuses through the porous medium of osteoporotic bone. Therefore, as a part of the planning paradigm, Basafa et al. [52] developed a cement diffusion model and validated its efficacy through simulations and experiments. Because of the extreme viscosities involved in the injection of bone cement, a modified method of Smoothed Particle Hydrodynamics (SPH) was selected for this purpose [52]. Research work presented in the upcoming chapters has greatly benefited from this development.

Figure 2.2: Representative anteroposterior (AP) radiograph of a proximal femur showing second-generation injection strategies: A) Single central augmentation following 8 mm drilling proposed by Beckmann et al. [12]. B) Balloon compression technique of Van der Steenhoven et al. [50]. C) V-shaped augmentation pattern proposed by [51].

In a more recent study, Kok et al. [53] investigated the clinical feasibility of femoroplasty injections using a calcium sulfate/hydroxyapatite based cement. However, the results of computational models suggest that without proper planning of the injection location, the increase in fracture strength will be limited [53]. Table 2.1 summarizes the results of second-generation studies on prophylactic femoroplasty.

All of the studies mentioned above suggest than femoroplasty is a promising approach to lower the risk of osteoporotic hip fractures. However, in order for this surgery to become a routine clinical procedure, further studies are required to ensure its efficacy and safety. Therefore, this procedure could benefit from a multi-physics planning paradigm that consists of computational models of the femur for both the biomechanical and heat-transfer simulations, as well as cement infiltration of the cancellous bone.

Table 2.1: Summary of the published second generation experimental studies on femoroplasty, data were compiled from the studies of Sutter et al. [11], Van der Steenhoven et al. [50], Beckmann et al. [12], Fliri et al. [51], Basafa et al. [16], and Kok et al. [53]

Study	Samples	Cement	Volume (ml)	Location	Change in yield load (%)	Change in fracture load (%)	Change in yield energy (%)	Change in fracture energy (%)
Sutter et al. (1)	10	PMMA	15.2 ± 1.5	Neck	+22	+37	+80	+154
Sutter et al. (2)	18	PMMA	15.1 ± 1.6	Trochanter	+9	+8	+7	+53
Van der Steenhoven et al.	16	Polymethyl siloxane	35	Head and neck	...	-5	...	...
Beckmann et al. (1)	7	PMMA	12	*	...	+23	...	+160
Beckmann et al. (2)	7	PMMA	12	**	...	+35	...	+164
Beckmann et al. (3)	7	PMMA	12	***	...	+12	...	+12
Beckmann et al. (4)	7	PMMA	12	****	...	-26	...	-19
Fliri et al.	5	PMMA	11	Neck cortices	...	-9	...	+124
Basafa et al.	8	PMMA	9.5 ± 1.7	Customized	+33	...	+118	...
Kok et al.	5	CaS/HA	10	Neck	...	...	+42	...

* Single central
** Single centrodorsal
*** Double ventrodorsal
**** Double craniocaudal

2.4 Computer-assisted Orthopaedic Surgery

One of the long-term goal of the research presented in this thesis is to develop an integrated surgical system for femoroplasty. The overall system intends to augment the femur using a patient-specific and biomechanically-guided planning paradigm and consists of three main components:

1. A pre-operative plan to optimize cement location based on biomechanics
2. A navigation system to estimate the 3D pose of the femur anatomy and the injection device
3. An intraoperative assessment of the injection pattern

Figure 2.3 illustrates these components and information flow among them. Once a patient is selected for the procedure, the planning module provides the surgeon with an optimal pattern and volume for the injection using Computed Tomography (CT) images. During the surgery, navigation system guides the surgeon to drill the bone based on the desired path. Next, injection is performed using an automated injection device that can estimate bone cement's viscosity and control the injection accordingly. Finally, intraoperative X-ray images are taken to assess the pattern of injection, analyze the results, and if needed, update the plan.

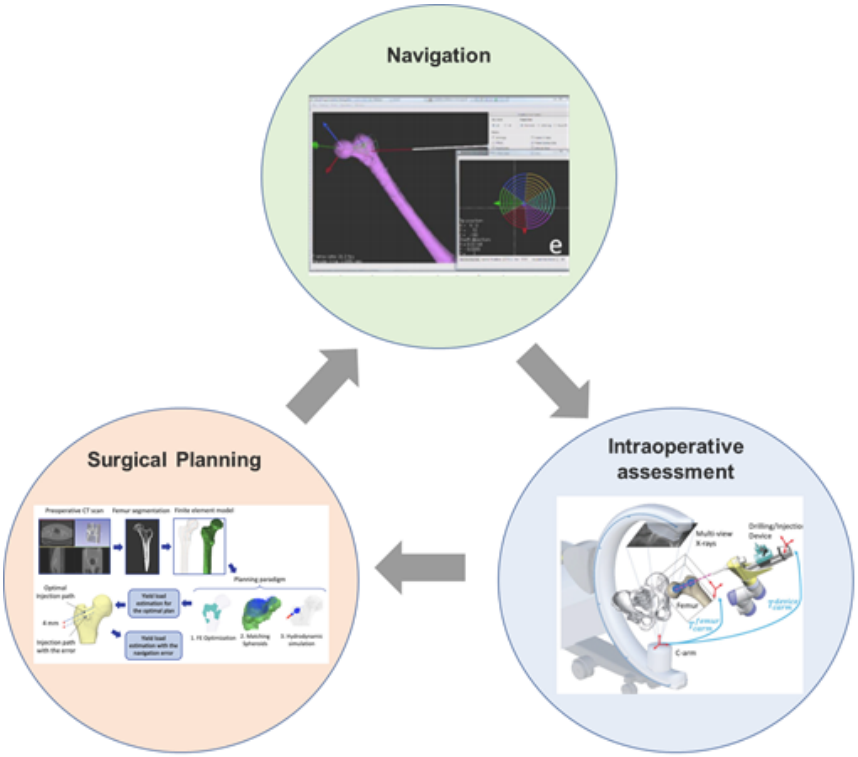

Figure 2.3: Overview of the main system components for femoroplasty

Most of the work presented in this thesis is dedicated to developing a new pre-operative plan for femoroplasty (Chapters 3,4, and 5). However, next section describes some research efforts towards developing a robot-assisted framework for intraoperative execution of femoroplasty and other orthopaedic surgeries (e.g. hip revision surgery). Prior to the work presented here, Kutzer et al. [54] has designed and built an injection device for precise delivery of PMMA inside porous media. The device allows high pressure injections to avoid leakage of bone cement into unwanted regions of the bone. Furthermore, Otake et al. [55] developed an intraoperative navigation system using an image-based 2D/3D registration framework with X-ray images and fiducial-based C-arm

tracking. This system, however, involves attachment of external pins to the bone and is not ideal for patients with osteoporosis. In addition, manual handling of the injection device may introduce an error in the overall injection pattern.

2.5 Robot-Assisted System Overview

The Robotic system consists of a 6-DOF robot (UR 10, Universal Robot, Odense, Denmark), an optical tracking system (Polaris optical system, Northern digital INC, Canada), a custom drilling/injection component, and a computer. An overview of this system is shown in Figure 2.4. The robot is used to guide the drill or the injection needle based on the planned configuration that is determined in pre-operative planning and evaluated in the simulation prior to surgery. To this end, two approaches for drilling and injection are designed. One is an interchangeable system with separated drilling and injection tools; the other is an integrated system for both drilling and injection.

Figure 2.5 shows the integrated Drilling and Injection Component (DIC) in which a 3D printed shell attached to the robot is used as a supporter for other parts. A linear stage provides the push force on the plunger of the syringe and serves as a hard stop for drilling. The push force is measured by a force sensor on the linear stage. The injection volume and velocity can be adjusted based on

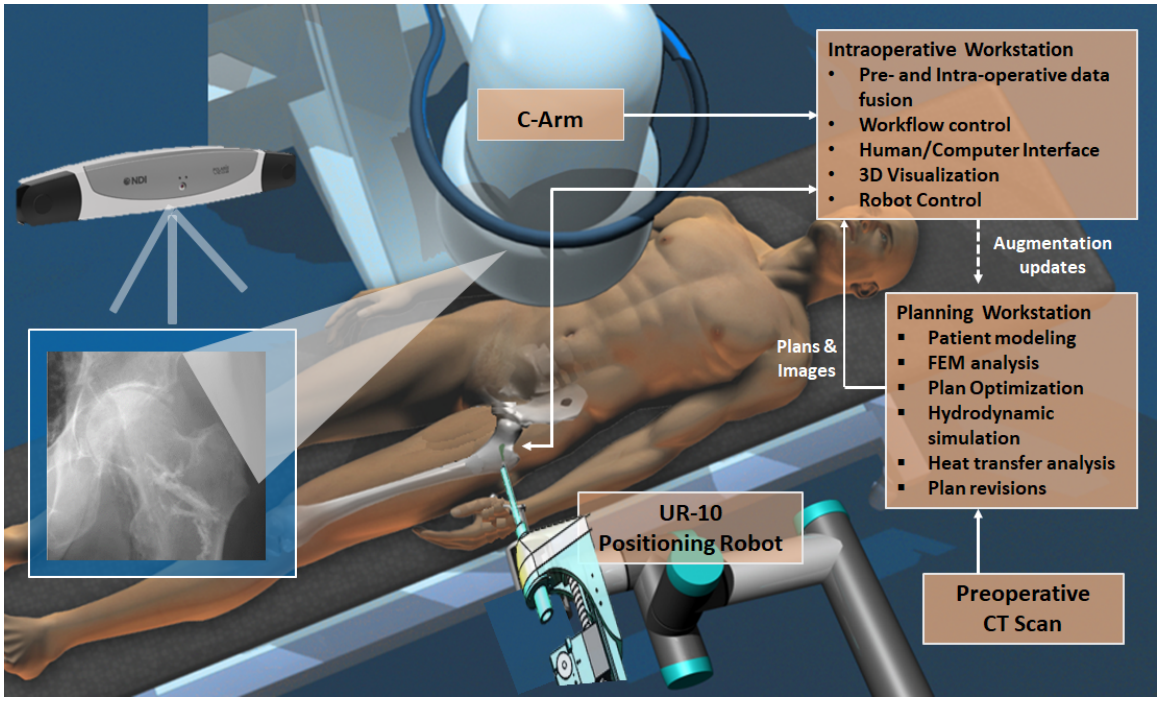

Figure 2.4: Overview of the Robot-assisted system components for femoroplasty

the feedback force data. A gauge made of stainless steel is the supporter of the syringe, meanwhile, the slender part of the gauge is used as a guide for both drill bit and cannula (both are 4mm in diameter). The length of the guide is 75mm and will be inserted into hip tissue during the procedure. Guide's length keeps a safe distance from the 3D printed shell to human tissue that helps with reducing the risk of infection.

To fit the different requirements of drilling and injection, a switch block is attached to the linear stage. The force sensor is fixed on one side of the switch to measure cement's viscosity while there is a limit hole for the drill bit on the other side. The limit hole would only allow the drill bit to pass through, and

the other parts of the hand drill will be held to control the injection's viscosity. There are 3 different positions the switch can be fixed, as is shown in Figure 2.5. One or two quick-release pins are used to fix the switch.

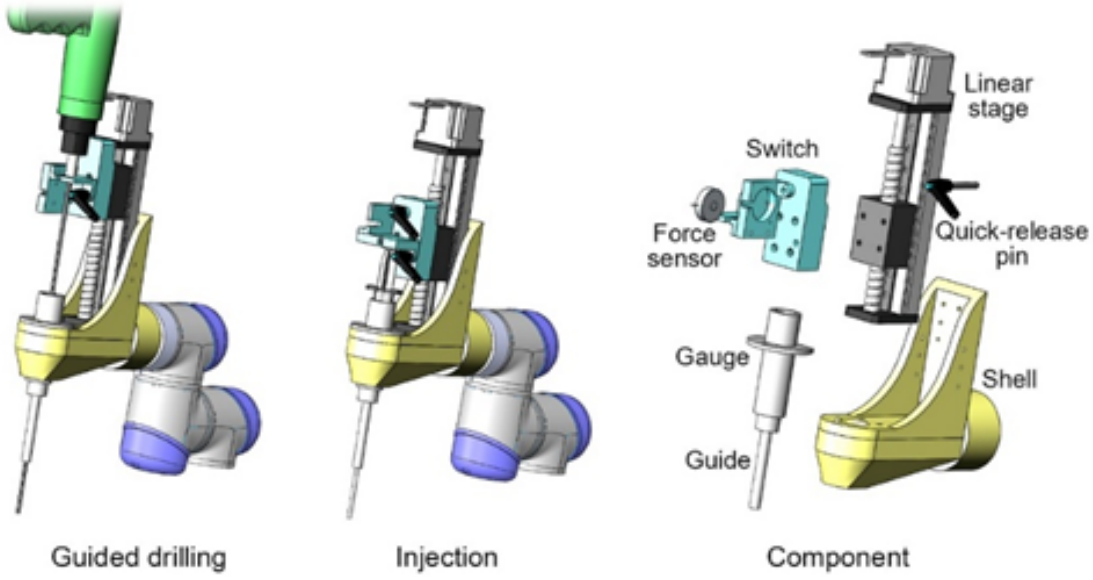

Figure 2.5: An integrated Drilling and Injection Component (DIC) designed for Robot-assisted Femoroplasty

Chapter 3

Significance of Preoperative Planning for Femoroplasty

3.1 Introduction

As discussed in the previous chapter, different injection strategies are proposed for Osteoporotic Hip Augmentation (OHA) to increase the efficiency and safety of the procedure [12, 13, 15, 56]. Most of these studies rely on a generic path for the injection, while others have aimed at customizing the injection pattern. Beckman et al. [12] concluded that a single central augmentation aligned with the femoral neck axis results in significant improvements in mechanical properties of the femur. However, recent patient-specific planning and computer-assisted augmentation resulted in significant biomechanical im-

provements using reduced amounts of bone cement [15, 56] as compared to studies where gross filling of the neck and trochanter was employed instead (more than 40–50ml) [11]. In the customized injection scenarios, cement location was determined using a modified method of Bi-directional Evolutionary Structural Optimization (BESO) [57]. In a recent study, however, Varga et al. [13] recommends generalized injection strategies for OHA arguing that detailed preoperative planning and controlled injection techniques are not realistic for the current clinical practice. In their study injection patterns were developed based on the principles of Wolff's law which state [43]:

1. Bone is an optimal structure relative to its mechanical requirements.

2. Bone can maintain an optimal configuration relative to alternative mechanical changes to its structure.

Through simulations, the study of Varga et al. [13] considers how bone would adapt its internal structure to withstand loading of a sideways fall. Numerical results suggested that cementation of the "main compression bridge" connecting the medial head region of the femur with the greater trochanter provides a larger increase in the yield load and yield energy of the proximal femur in side-way falls as compared to the "single central" configuration [13,46]. However, the assumption that a proposed injection strategy can be executed perfectly is not realistic. Therefore, it is also important to consider how the cement

diffuses inside the osteoporotic bone structure given any preoperative plan or injection strategy. Our group has previously developed a particle-based hydrodynamics model to predict the infiltration of cement into the porous medium of cancellous bone [52]. This model can be used to validate the effectiveness of different augmentation strategies prior to the execution.

In this chapter, we investigate if the additional computational overhead of the patient-specific planning can significantly improve the bone strength as compared to the novel generic planning attempted in the literature. Other contributions of this work include: (1) Modifying the computational paradigm introduced by Basafa et al. [15] to enhance the hydrodynamic simulations; (2) Demonstrating the significance of the hydrodynamic simulation within the context of overall planning paradigm; and (3) Comparing the effect of homogeneous versus inhomogeneous FE models within the proposed overall planning paradigm. [1]

3.2 Methods

3.2.1 Plan-based injection

High resolution Computed Tomography (CT) scans from four osteoporotic femur specimens (one male and three females) with average neck t-score of 3.2

[1] This chapter is published as [58]

(confirming osteoporosis) were obtained. From each pair, one specimen was randomly chosen for augmentation. The new planning paradigm consisted of three phases:

1. Finite Element (FE) optimization of the injection pattern based on the method of BESO;
2. Matching BESO results with realistic injection volumes;
3. Cement diffusion modeling based on the method of Smoothed Particle Hydrodynamics (SPH) [52]

To optimize cement pattern, a FE mesh of the femur was first created using concentric rings of quadratic 20-node brick elements, supplemented with 15-node wedge elements at the center [59]. Next, inhomogeneous material properties were assigned to these elements based on the bone density observed from the pre-operative CT scan. Using linear interpolation of known values for plastic phantom, Hounsfield Unit (HU) intensity values were converted to ash densities. Apparent density was calculated using 3.1 where $\rho_{aparent}$ and ρ_{ash} are ash and apparent densities in gr/ml, respectively [60].

$$\rho_{aparent} = \rho_{ash} \times 1.79 + 0.119 \tag{3.1}$$

Finally, the density values were converted to elastic modulus using 3.2 [61, 62]. In these models, the region above the lesser trochanter was assumed to be

mostly trabecular bone and the lower region was assumed to be mostly cortical bone. Figure 3.1 shows the distribution of elastic modulus of the femora.

$$\begin{aligned} E &= 10,500 \times {\rho_{ash}}^{2.29} \;\; Cortical\,Bone \\ E &= 6850 \times {\rho_{app}}^{1.49} \;\; Trabecular\,Bone \end{aligned} \tag{3.2}$$

where E is the elastic modulus in MPa. The Poisson's ratio of 0.4 is assumed for the femoral bone elements. In the first iteration of the BESO, we populate the proximal part of the femur with PMMA elements with elastic modulus of 1.2 GPa and Poisson's ration of 0.4. The inefficient PMMA elements were gradually removed from the FE model while added to the high load-bearing regions using strain energy as the criterion. Details of the optimization is described elsewhere [15] and was previously validated on seven cadaveric experiments [16].

In the second step of planning, we used gradient-descent optimization algorithm to find the closest match to the BESO results through simulation of realistic injection volumes (spheroids) of no more than 10ml combined. The optimization identifies the lengths (L_i) and radii (R_i) of injection blobs in addition to the target point and orientation of the injection path (angles θ and ϕ). A planar schematic of this algorithm is shown in 3.2.

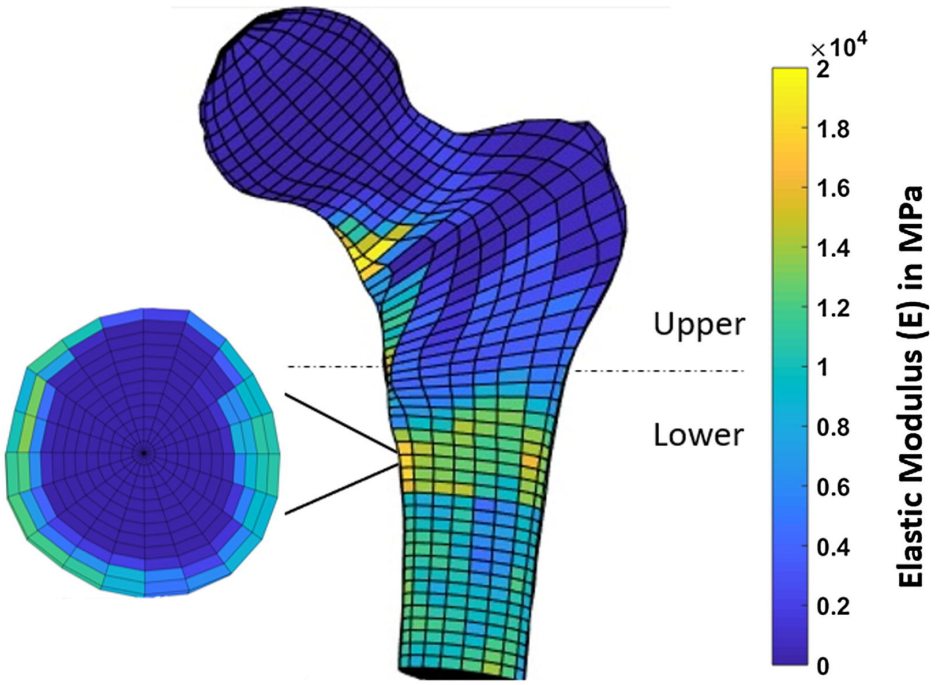

Figure 3.1: Distribution of the Young's elastic modulus in the critical region of the femur. Note that the upper region is assumed to be mostly cancellous.

$$Max \quad \frac{V_{BESO} \bigcap V_{Spheroid}}{V_{BESO} \bigcup V_{Spheroid}} \quad Subject\ to: \quad V_{Spheroid} < 10ml \tag{3.3}$$

where

$$V_{Spheroid} = \sum_{i=1}^{N} (\pi {R_i}^2 L_i + \frac{4}{3} \pi {R_i}^3) \tag{3.4}$$

and N is the number of spheroids.

In the final step of the planning, we ran the SPH simulation to estimate the final distribution of the cement within the bone structure. SPH incorpo-

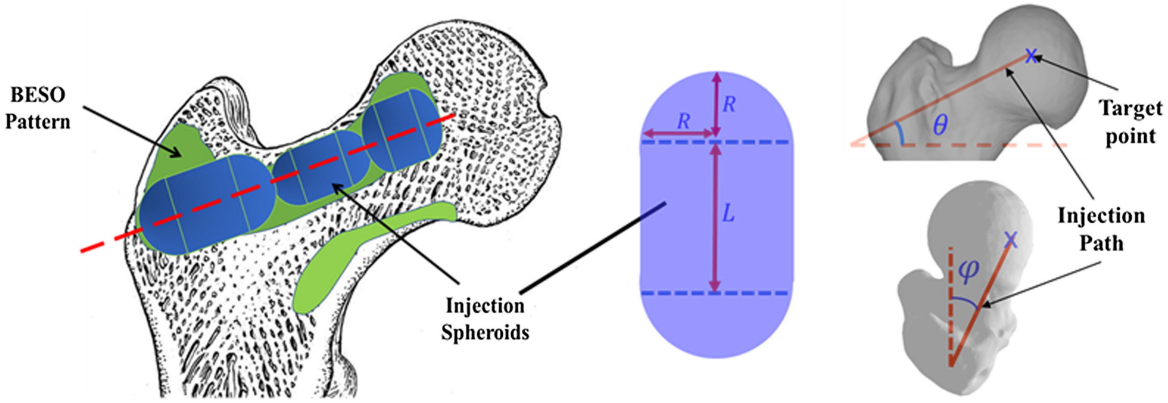

Figure 3.2: Schematic of the optimized injection pattern by BESO (green), practical injection volume (blue) and line of injection (red). Note that the target point (starting point of injection), length (L) and radius (R) of each injection blob, and orientation of the injection path are optimally selected to find the closest match between the BESO pattern and injection spheroids. (For interpretation of the references to colour in this figure legend, the reader is referred to the web version of this article.)

rates the extreme viscosities associated with the bone cement. This is done by creating a porous model of the proximal femur from CT volume. Assuming an injection rate of 0.1 ml / s and viscosity of 200 Pa·s for the bone cement at the time of injection, SPH simulates the hydrodynamics by removing the tissue particles on the path of a virtual drill (injection line) and gradually introducing cement fluids on the same path [52]. Three major steps of planning paradigm are shown in Figure 3.3.

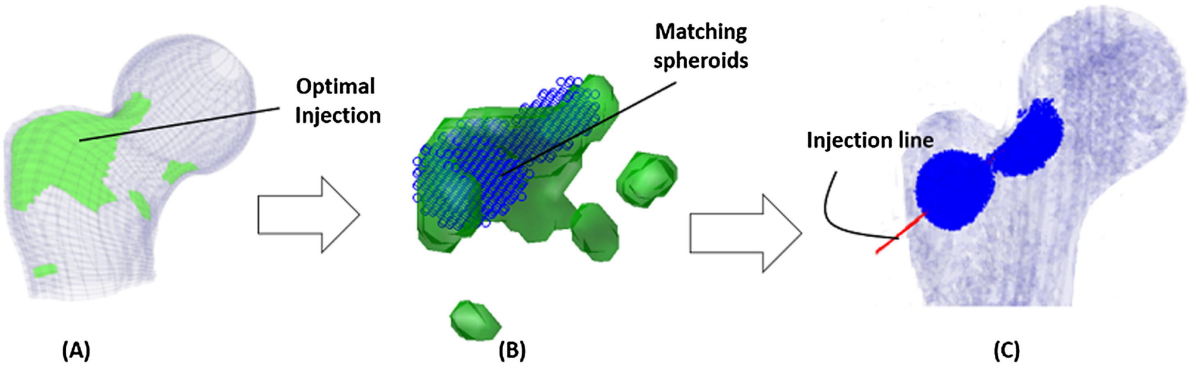

Figure 3.3: (A) Schematic of the optimized injection pattern by BESO, (B) the matching spheroids (blue rings) and (C) line of injection with corresponding results of the SPH simulation (blue).

3.2.2 Generalized Injection Strategies

In addition to the customized injection strategy, three generalized injection patterns were selected based on the previous studies including the single central [46] (V1; Red), main compression bridge (V2; Blue) and compression bridge to the lower part of the femoral head (V3; yellow) [13]. For each of these injections, we assumed a single injection blob (spheroid) with volume of 10ml connecting the desired anatomical landmarks (3.4). This was followed by a diffusion simulation to estimate the final cement blob using the SPH method described earlier.

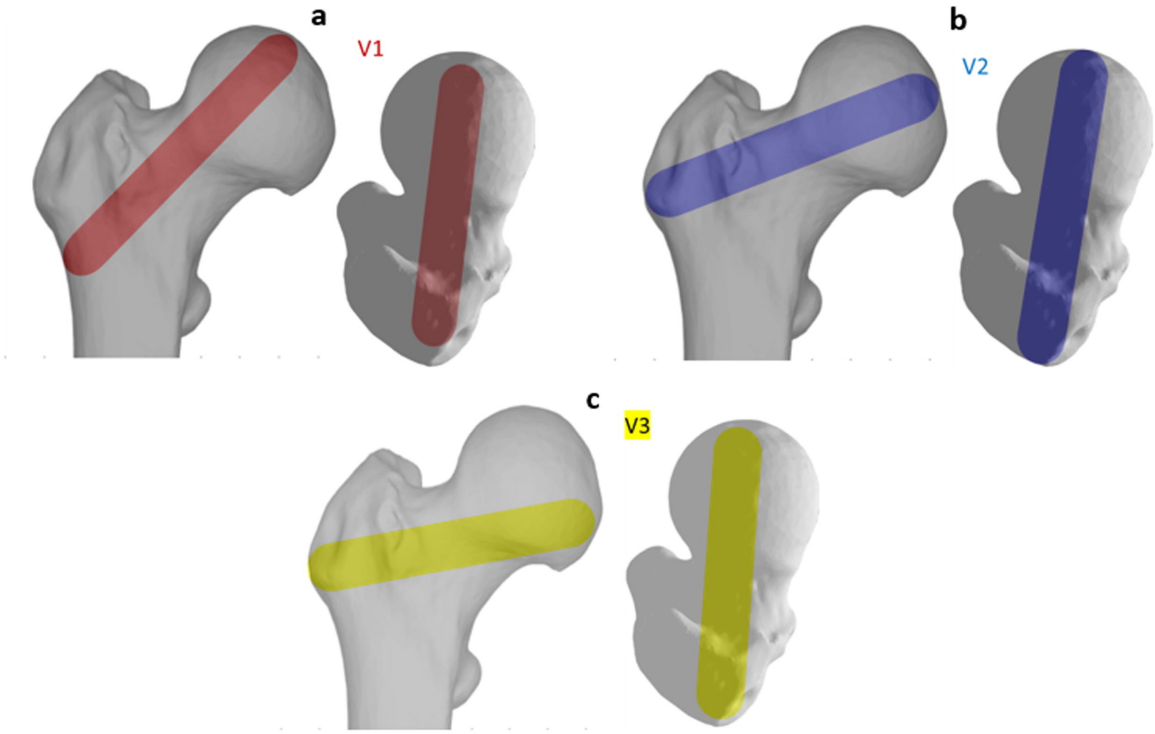

Figure 3.4: Generalized injection strategies: a) Single central (V1; Red), b) Main compression bridge (V2; Blue) and c) Compression bridge to the lower part of the femoral head (V3; yellow).

3.2.3 Biomechanical Evaluation and Data Analysis

To evaluate the biomechanical effect of each injection strategy, a static FE analysis was performed on each model using ABAQUS (ABAQUS/Standard V6.8, SIMULIA, Providence, RI). Each model was evaluated with both homogeneous and inhomogeneous material properties to investigate the potential differences of biomechanics when boundary conditions simulating a side-way fall on the greater trochanter are applied [47] (Figure 3.5). For the homoge-

neous models, we have assumed an average ash density (ρ_{ash}) of 0.206 g / ml for all the bone elements and have calculated the apparent density as 0.488 g / ml from Figure 3.1 [60]. The output parameters from the FE solver included the displacement component of the loaded nodes in the direction of the load and maximum and minimum principal strain values, reported at the centroid of each element. Using the parameters at the load of 500N and assuming linearity, outputs could be scaled for any desired load. Following the procedure in [57], we define yield load as the load at which combined volume of the failed elements reach 1% of the total volume of the specimen. To compare the effectiveness of different injection strategies, the values of yield load and yield energy were normalized to the non-augmented state of the same specimen for both homogeneous and inhomogeneous models. All generalized injections were considered based on a 10ml volume of PMMA since the customized injections were constrained by this value in the gradient-descent optimization described before. For each group, mean and standard deviation of the data were given as descriptive statistics. Results of different strategies were compared through a two-way ANOVA test with state significant level of 0.05.

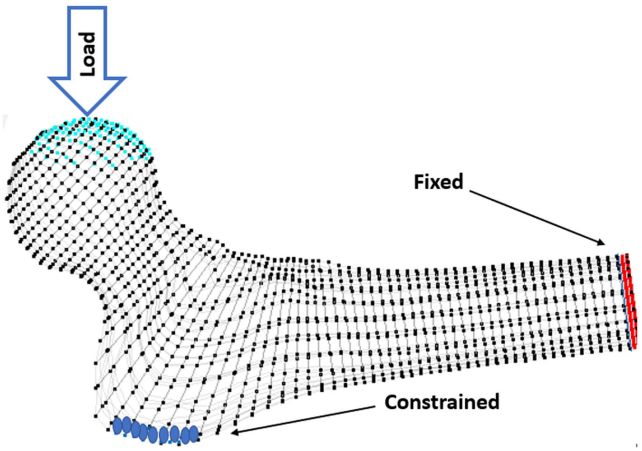

Figure 3.5: Boundary conditions simulating a side-way fall on greater trochanter. The distal vertices were fixed in all three directions and the surface vertices on the 10mm lateral side of the greater trochanter were restricted to move only in the y–z plane.

3.3 Results

To investigate the possibility of realistically reproducing the generalized patterns of injection, we ran SPH for the cement blob of each generalized injection strategy. Figure 3.6 shows SPH results of the generalized injections for specimen 1 and the final distribution of cement elements in the FE model. It can be observed from the pattern of the FE mesh that the thickness of PMMA is unlikely to match those of the desired pattern (cylindrical volumes shown in Figure 3.4).

All injection methods were found to improve the biomechanical properties of the femur simulating sideway falls. The average injection volume of the optimized pattern was 9.2 ml (SD=1.0 ml). Most of the optimal injection lines were directed from the supero-anterior aspect of the neck to the posterior of

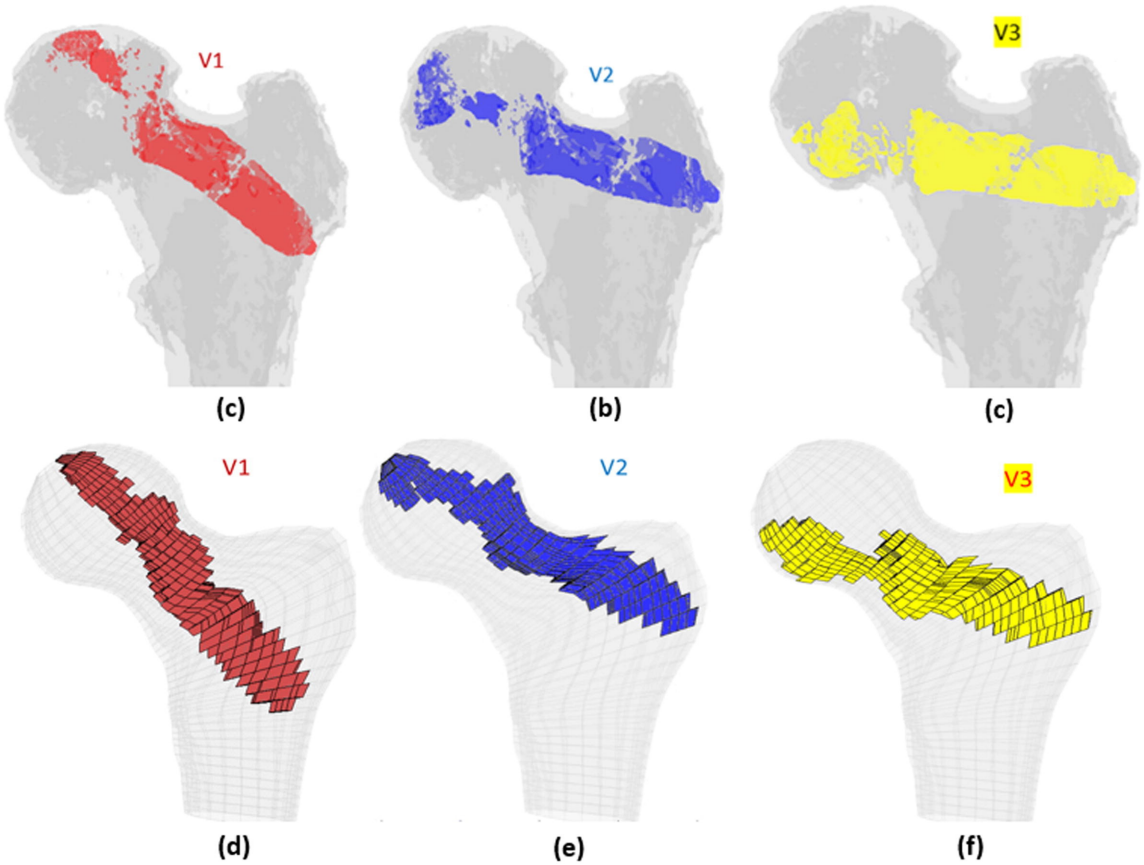

Figure 3.6: SPH results of generalized injection strategies (a) the single central mesh of the specimen 1 with diffused volume of cement in different variations of the generalized injection strategies: The single central (V1; Blue), main compression bridge (V2; Blue) and compression bridge to the lower part of the femoral head (V3; yellow).

the greater trochanter. Figure 3.7 shows the conversion of SPH results for customized injections patterns into FE mesh.

The normalized Results of the FE analysis suggest that the customized injection patterns are significantly more effective in increasing the yield load of the proximal femur than those of the generalized path in the inhomogeneous models ($P < 0.01$). This difference however is not significant in the homoge-

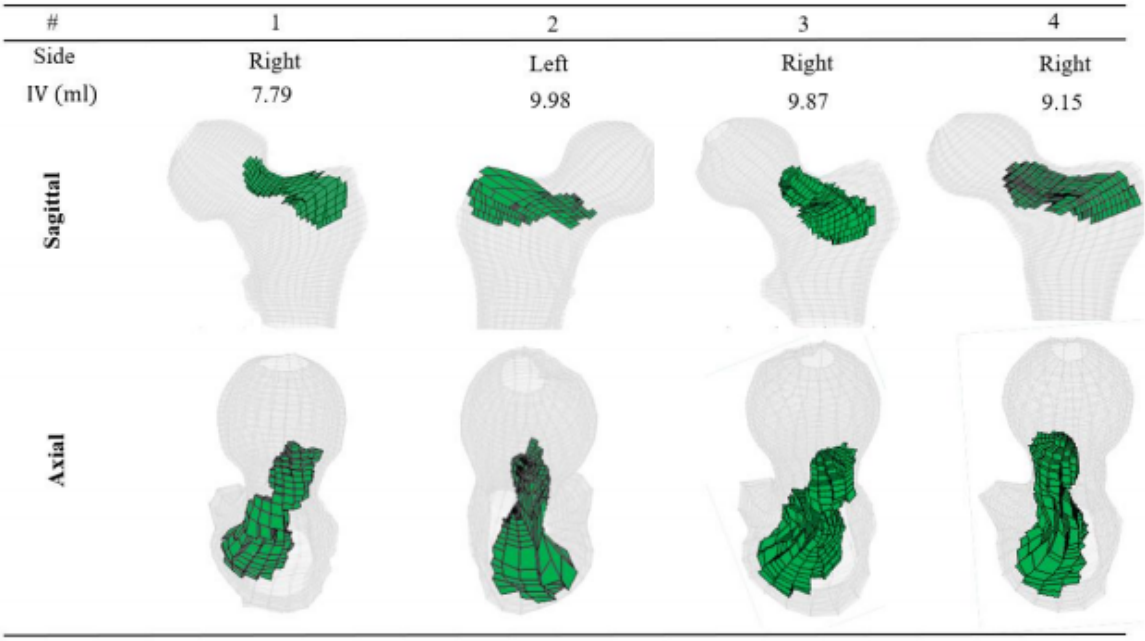

Figure 3.7: FE mesh of the femur specimens with the optimized injection patterns after hydrodynamic simulation. Cement volumes were constrained and initially located based on the modified method of BESO

neous models (P=0.234). In addition, customized injections can increase the yield energy by 199% (Standard Deviation (SD)=78.4%) which is significantly higher than those of generalized injections (117% (SD=38.4), 140% (SD= 52.6) and 136% (SD=52.3%) for V1, V2 and V3, respectively). Relative improvements on yield load and yield energy were calculated for all injection variations and are summarized in Figures 3.8 and 3.9. Note that injection in the main compression bridge (V2) is more effective than other variations of the generalized injection.

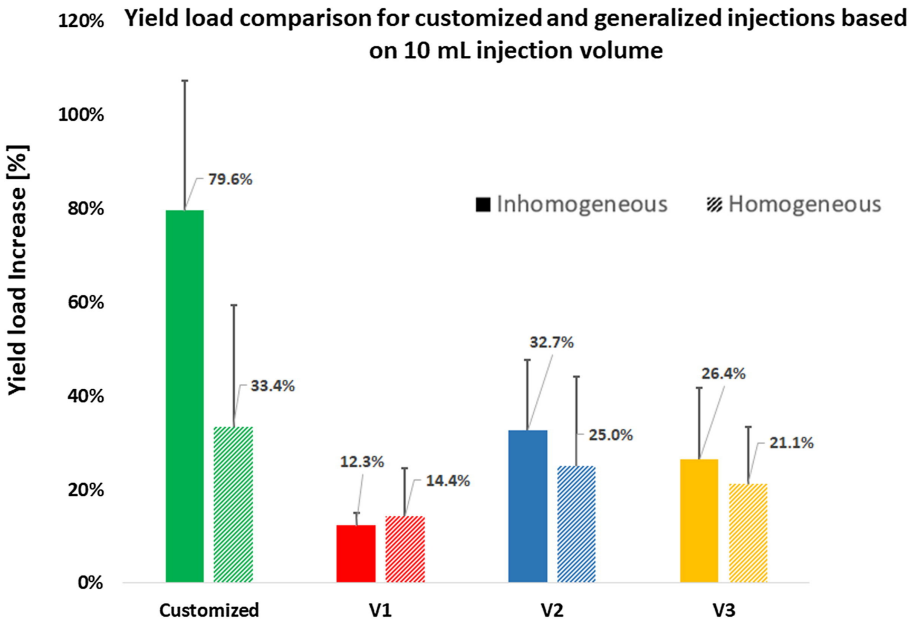

Figure 3.8: Percentage of the yield load increase normalized to the non-augmented state of the same specimen.

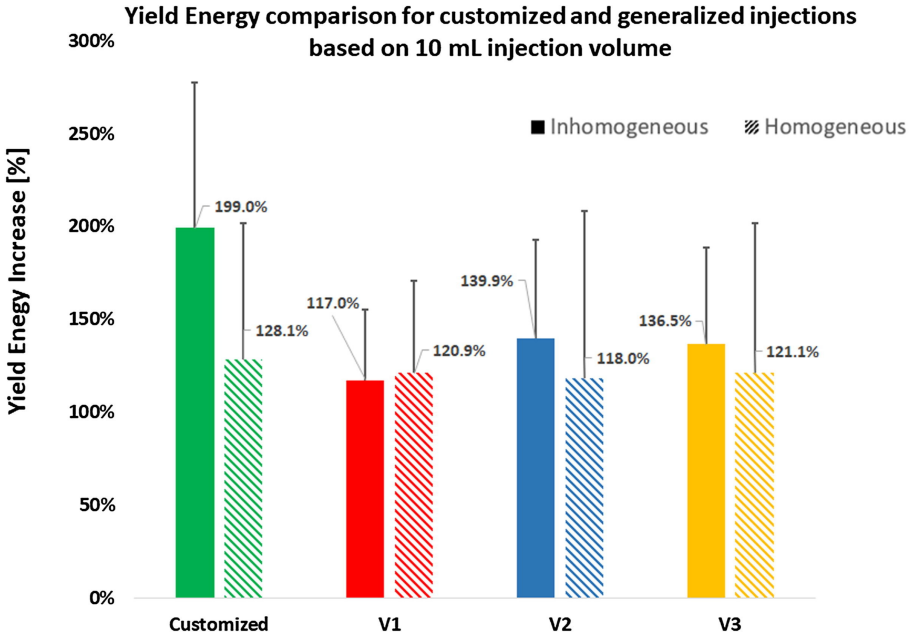

Figure 3.9: Percentage of the yield energy increase normalized to the non-augmented state of the same specimen. Among different injection strategies, only the customized injection in the Inhomogeneous group was significantly higher than the others.

3.4 Discussion

Results of the hydrodynamic simulations combined with the FE analyses suggests that OHA can significantly benefit from a pre-operative plan that defines the 3D path of the drill hole and pattern of injection as compared to a generalized injection recommendation made in recent literature. Several cadaveric and simulation-based studies were conducted in the past to evaluate different injection strategies for OHA [10, 14, 63]. In this study, we have investigated four of these strategies: V1; the single central augmentation [46], V2 and V3 that were previously developed based on the principles of bone remodeling (Wolff's law) and resemble the main compression bridge [13], and a modified method of patient-specific OHA based on a previously validated planning paradigm [15]. Simulation results demonstrated that all injection variations improve the fracture-related biomechanical parameters; however, the customized injection strategy is significantly more effective in improving the fracture-related biomechanical properties of femur compared to all general patterns ($P < 0.01$).

In this study, we used both homogeneous and inhomogeneous material properties in FE models to compare different injection strategies. Inhomogeneous model of the bone, which was previously validated in cadaveric studies [16] leads to significantly different results from the homogeneous model ($P < 0.01$)

suggesting that customized models can greatly benefit OHA, as the mechanical properties of the bone are calculated based on radiodensities of pre-operative CT images.

Computational modeling of novel generalized injection strategies was recently presented by Varga et al. [13] using nonlinear FE simulations. Results of this study are similar in concluding that V2 is a more effective than the other two injection strategies. However, this study suggests a lower yield load (32.7% (SD=15%) compared to about 45%, as reported in the literature) for V2. This difference can be explained by the results of SPH demonstrated in Figure 3.6. The desired pattern of PMMA distribution (shown in Figure 3.4) is considerably different from post-operative results of the injection. Most of such variations occur in the femoral head and are observed for all generalized injections. In addition, unexpected leakage of bone cement combined with exothermic nature of PMMA curing may result in complications such as osteonecrosis or blockage of the blood supply. Thus, once a pattern of injection is chosen for OHA, it is important to consider how PMMA distributes in the proximal femur altering the biomechanical outcomes.

In a more recent study on patient-specific femoroplasty, it was observed that 11.7 ml of cement can lead to 100% increase of yield load in simulation [56]. Assuming linearity, algorithm presented in this chapter increase the yield load by 93.1% for the same volume. However, the injection patterns in the study of

Santana et al. [56], are idealized and do not lie on a single line of injection. The proposed modifications to the planning paradigm presented in this chapter may reduce this difference since the algorithm decides on a single line of injection for all cases.

Apart from the improved outcome of customized planning for OHA, surgical implementation of this strategy requires an image-guided system for intra-operative feedback that are discussed in the upcoming chapters. This system consists of surgical navigation involving 2D/3D registration of pre-operative CT scans to the femur radiographic images [55], real-time tracking, and a hand-held motorized bone cement delivery device [54].

The biomechanical evaluation analysis used in this study closely follows the approach that was previously verified against cadaveric experiments where invasive testing was performed to estimate the yield load ($R^2 = 0.74$) [16]. However, the future work needs to directly evaluate the modified version of the Basafa's paradigm against cadaveric experiments. Furthermore, this study did not attempt to create a generic approach based on averaging patient-specific approaches. This may or (may not) provide a better generic approach as compared to the present literature. However, applying such generic approaches will still require real-time navigation for trajectory planning, 2D-3D registration, and a motorized device to control the surgical execution. We submit that the main overhead of both generic and patient-specific femoroplasty come from

the surgical execution. Thus, the use of a better generic approach may not turn out to offer much advantage compared to the patient-specific paradigm. In addition, since the injections of more than one blob requires controlled injection techniques, all generalized injection were based on a single blob injection (constant rate).

OHA is shown to improve the fracture related biomechanical properties of the femur. However, the exothermic reaction of PMMA polymerization may introduce the risk of thermal necrosis. This point was not addressed in the current study. In a separate study discussed in Chapter 5, we have shown that the maximum temperature-rise of the bone surface is 10°C which occurs about 12 minutes after cement injection [64]. Other studies have pointed out that the temperature increase in the range of 45–60°C (temperature-rise of 8–23°C) may cause thermal tissue damage, depending on the exposure time [65, 66]. Therefore, in the future, in addition to the mechanical strength of the femur, maximum temperature-rise and duration of thermal exposure are important factors that need to be considered while planning the injection parameters for OHA.

3.5 Recapitulation of Contributions

The author's contributions in this chapter are as follows:

- Proposing a new patient-specific plan for femoroplasty to reduce the volume of PMMA injection. A gradient-descent optimization algorithm was implemented in MATLAB to find the closest match between the BESO results and realistic injection volumes (spheroids).

- Developing FE models to evaluate the effects of three generalized injection strategies on biomechanical properties of the bone.

- Demonstrating the significance of the hydrodynamic simulation within the context of overall planning paradigm.

- Comparing the effect of homogeneous versus inhomogeneous FE models within the proposed overall planning paradigm.

The preoperative plan was facilitated through the structural optimization algorithm previously developed by Dr. Ehsan Basafa. This chapter provides a baseline for experimental validation, which is discussed in the forthcoming chapters.

Chapter 4

Experimental Evaluation of the Planned Injections

4.1 Introduction

In the previous chapter, we introduced a new patient-specific planning paradigm to reduce the volume of injected cement [58]. Through FE simulations, biomechanical outcomes of injections were compared with those of the generic injections and results showed that injection recommendations of the new planning paradigm can significantly increase the yield load (79.6%, $P < 0.01$) and yield energy (199%, $P < 0.01$) of an osteoporotic femur. The increase was significantly higher than those of generalized injections proposed previously [12, 13, 51]. However, the new approach was not validated via direct experi-

ments. Contributions of this chapter include:[1]

1. Investigating the biomechanical effectiveness of the newly proposed planning paradigm.

2. Evaluating the bone surface temperature rise during cement polymerization through cadaveric experiments.

4.2 Methods

4.2.1 pre-operative Planning Paradigm

Details of the biomechanically-guided planning paradigm was fully described in Chapter 1 and also in [58]. There are two major differences between this planning paradigm and previously developed augmentation plan described in [15]:

1. In the previous generation of the subject-specific plan for femoroplasty, injections were simulated for three different regions of the proximal femur with each region containing several 'test' points and the injection that overlapped most with the BESO pattern was selected to determine the drill path [15]. In this study, parameters that determine the injection profile are selected through an optimization algorithm.

[1]The majority of the work presented in this chapter is submitted for publication to the Journal of Clinical Biomechanics and is currently under review.

2. Cement injections in the new plan were performed dynamically (i.e. the injection needle was retracted during cementation), while the injection needle was fixed during cementation previously. This improves the overall coverage of the optimal pattern.

For the experiments, six pairs of fresh cadaveric femur specimens (one male and five females) were obtained from the Maryland State Anatomy Board, Dual Energy X-ray Absorptiometry (DEXA) scanned (Lunar Prodigy Advance, GE Healthcare Lunar, Madison, WI), and cleaned of soft tissue. The specimens were then stored in a freezer (-18°C) until one day before the augmentation procedure when they were left at room temperature to thaw. A relevant summary of cadavers' demographics and DEXA scanning results are presented in table 4.1. Next, a high-resolution CT scan (Toshiba Aquilion One, Canon Inc., Tochigi, Japan) was obtained for each of the specimens. Following the procedure in [57], a FE model was created for each bone and initial yield load was estimated. From each pair, one femur with the lower initial yield load was selected for augmentation. The new planning paradigm consists of three steps: first, the optimal pattern of bone cement was determined through an FE analysis in which inhomogeneous material properties were assigned to the bone elements based on density values calculated from CT. This was achieved using a modified method of Bi-directional Evolutionary Structural Optimization (BESO) [15]. In the second phase of planning, a gradient-descent optimization

algorithm was used to find the closest match between BESO results and realistic injection blobs of bone cement. The optimization constrains the injection volume such that only one drill hole is required. In addition, total volume of injection does not exceed 12 ml, so that we have:

$$Minimize \ \frac{V_{injection}}{V_{injection} \bigcap V_{BESO}} \ Subject \ to \ V_{injection} < 12ml \tag{4.1}$$

where V_{BESO} is the optimal pattern of PMMA defined by the FE and $V_{injection}$ consists of 2 or 3 injection blobs in cylindrical shapes with end caps that lie on a single injection path 4.1. In the third step of planning, cement dispersion inside the bone was predicted using a modified method of Smoothed Particle Hydrodynamics (SPH), which uses discrete particles to approximate continuum field quantities. In our planning paradigm, we run SPH to predict the actual yield load of the specimen after augmentation with realistic injection blobs. For this purpose, we first create a porous model of the proximal femur from the CT volume (considering the inhomogeneous permeability of the bone) and remove the tissue particles on the path of a virtual drill (or injection needle). Next, we simulate the injection of bone cement at the rate of 0.1 ml/s and viscosity of 200 Pa.s. on the same path [52].

Table 4.1: Sample demographics– Neck T-scores and BMD were obtained from DEXA Scanning. The Neck T-scores and BMDs are reported for both the limb to be augmented and the control side.

Sample	Age	Gender	Neck T-score		Neck BMD g/cm^3		Condition
			Augmented	Control	Augmented	Control	
1	89.3	Female	-3.8	2.0	0.525	0.735	osteoporotic
2	69.3	Female	-2.2	-2.8	0.716	0.641	osteoporotic
3	59.4	Female	-2.2	-2.0	0.714	0.738	osteopenic
4	91.8	Female	-4.0	-3.6	0.496	0.550	osteoporotic
5	72.8	Female	-4.3	-4.2	0.468	0.480	osteoporotic
6	68.4	Male	-2.8	-2.6	0.590	0.617	osteoporotic
Average($\pm SD$)	75.2($\pm$12.7)	-	-3.2($\pm$0.9)	-2.9($\pm$0.9)	.58($\pm$1.0)	.63($\pm$1.0)	-

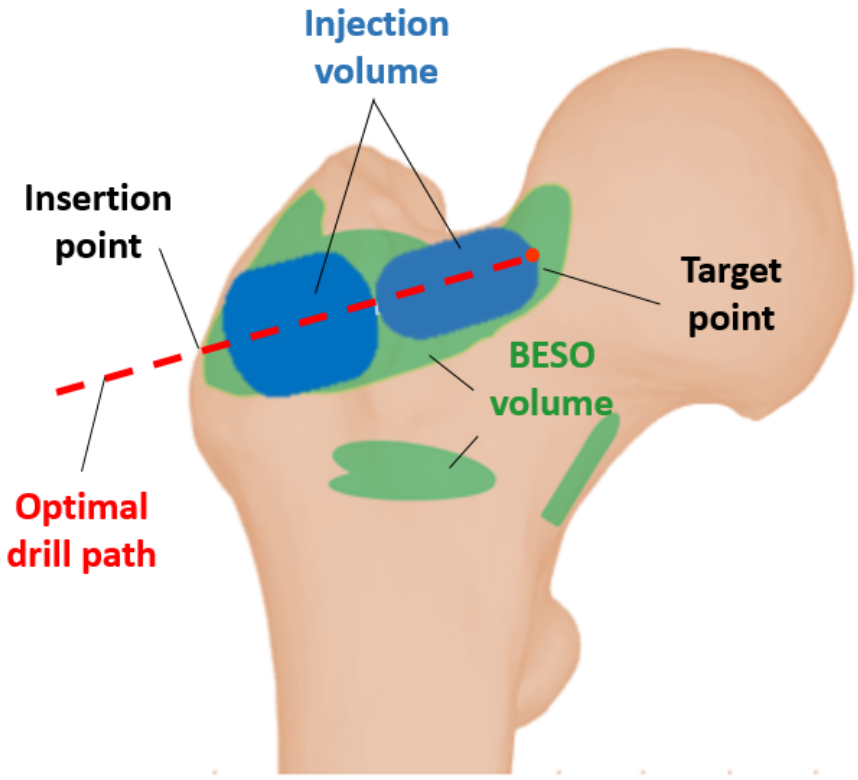

Figure 4.1: Schematic of the optimized injection pattern by FE using BESO method (green) and the injection blobs defined by the planning paradigm (Blue)

4.2.2 Navigation System

Prior to each experiment, femora were removed from the freezer and left at room temperature to thaw. This was followed by removing the remaining soft tissue from the femur. For navigation, we used an in-house system developed and validated previously by Otake et al. [55]. Briefly, three landmarks, i.e., center of the head, lateral most point on the greater trochanter, and the protrusion

point of the lesser trochanter, were selected on the model of the bone segmented in the Medical Imaging Interaction Toolkit (MITK) (German Cancer Research Center, Heidelberg, Germany). Using a tracked digitizer (Passive Probe, NDI, Waterloo. ON, Canada) and an optical tracker (Polaris, NDI, Waterloo, ON, Canada) these points were identified on the femur specimen. The transformation between these two sets, provided an initial guess for registration. Next, patches of surface points were digitized, and a point cloud-to-surface registration was performed using the Iterative Closest Point (ICP) algorithm [67] (Figure 4.2c). Bone registration was followed by navigation of a cordless hand drill (DCD760, DeWalt Industrial Tool Co., Baltimore, MD) tracked by a rigid body to drill the injection path defined by the pre-operative plan. The navigation guides the user to the drill path by providing the distance and angle errors of the drilling configuration in real-time.

4.2.3 Cement Injection and Temperature Measurement

After drilling, we used a custom designed injection device similar to that of previously developed by Kutzer et al. [54] for cement delivery. The modified device utilizes a 20 ml syringe. Consequently, 15 g of radiopaque dose Spineplex (Stryker, Kalamazoo, MI) was mixed with 13.5 ml of the monomer liquid

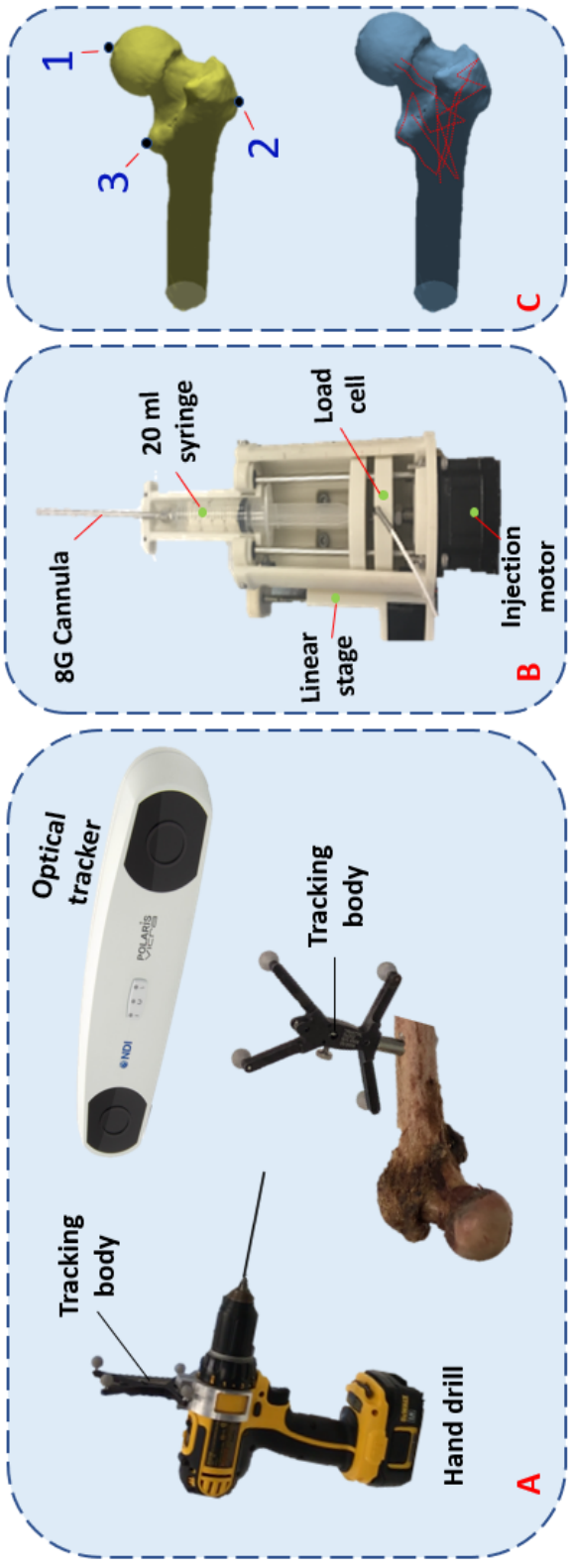

Figure 4.2: (A) Intra-operative system for drilling navigation, (B) An automatic injection device for bone cement delivery into the planned region, (C) Predetermined points for initial registration (top) and surface points used for ICP registration (bottom).

about 60 s. We then filled the syringe with this mixture, attached a 15.2 cm, 8G cannula (Scientific Commodities Inc., Lake Havasu, AZ) and placed it in the injection device. Approximately 12 minutes from the start of mixing the powder and liquid, we estimated the viscosity of bone cement by ejecting 0.5 ml of cement at the rate of 0.1 ml / s while measuring and averaging the pressure using a compression load cell (OMEGA Engineering Inc., Stamford, CT). This viscosity estimate, along with previously extracted viscosity-time calibration curves for this cement mix using the same setup, was used to calculate the remaining time before the cement reaches the desired viscosity of 200 Pa.s. At that time, cement was automatically ejected at the controlled rate of 0.1 ml / s while the injection device retracted the cannula from the start of the first injection blob (target point) towards the bone surface. Note that the retraction rate of the cannula varies for each blob depending on their size (length and radius). Meanwhile, from the start time of the injection, we measured the surface temperature of the bone at one second intervals in three regions, i.e., greater trochanter, trochanteric crest, and femoral neck using previously planted k-type thermocouples (Thermometrics Inc., Northbridge, CA) with probe diameter of 0.6mm. Thermocouples were placed inside 1mm drill holes made on the surface at the depth of 2mm to minimize the effect of room temperature on the measurements. Figure 4.3 shows the location of the thermocouples with respect to the femur anatomy. These regions were selected based on the location

of main arteries that supply blood to the femoral head [68, 69].

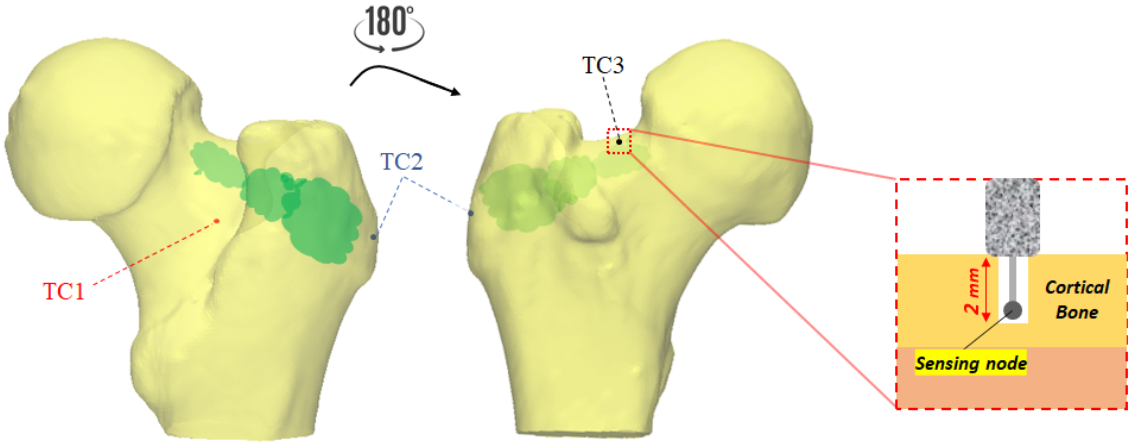

Figure 4.3: Thermocouple placement for temperature measurements. Note that k-type thermocouples recorded the temperature at one second interval and depth of 2mm from the surface on trochanteric crest (TC1; red), the greater trochanter (TC2; blue), and femoral neck (TC3; black)

4.2.4 Post-operative Mechanical Testing and Data Analysis

Following the plan-based injections, another set of CT scans were obtained. To discover how closely PMMA distributions matches those of pre-operative simulations, we used the technique previously described in [16] to estimate the translational error between their corresponding isosurface. This was followed by mechanical testing to failure in configuration of a fall to the side on the greater trochanter. As shown in Figure 4.4, we positioned the axis of femur shaft so that it was 10 degrees below a horizontal plan parallel to the

MTS table and rotated the femoral shaft 15 degrees internally [47]. While the greater trochanter was supported by a dollop of PMMA, the femoral head was pre-loaded to 50N by the MTS machine (Bionix 858 Test System, MTS, Eden Prairie, MN). Next, femoral head was displaced downward at the rate of 100 mm / s until failure [47]. For each specimen, the first inflection point of the load-displacement curve was recorded as yield load. In addition, we recorded the maximum load. Yield and maximum energy were defined as the area under force-displacement curve up to yield and maximum load respectively [16](see Fig. 4.5). A paired t-test was used to compare the biomechanical outcomes of the augmented and control femora ($P < 0.05$). In comparison of the biomechanical properties, we have only considered the osteoporotic specimens (Sample 1, 2, 4, 5 and 6).

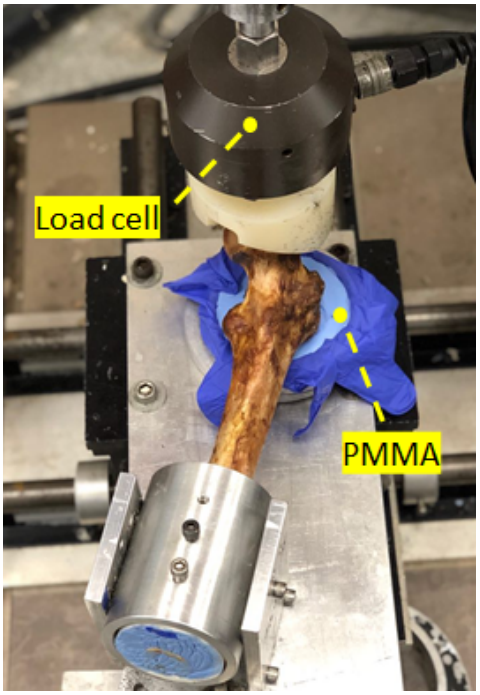

Figure 4.4: Experimental set-up simulating a fall on the greater trochanter using MTS machine (Bionix 858 Test System, Eden Prairie, Minnesota)

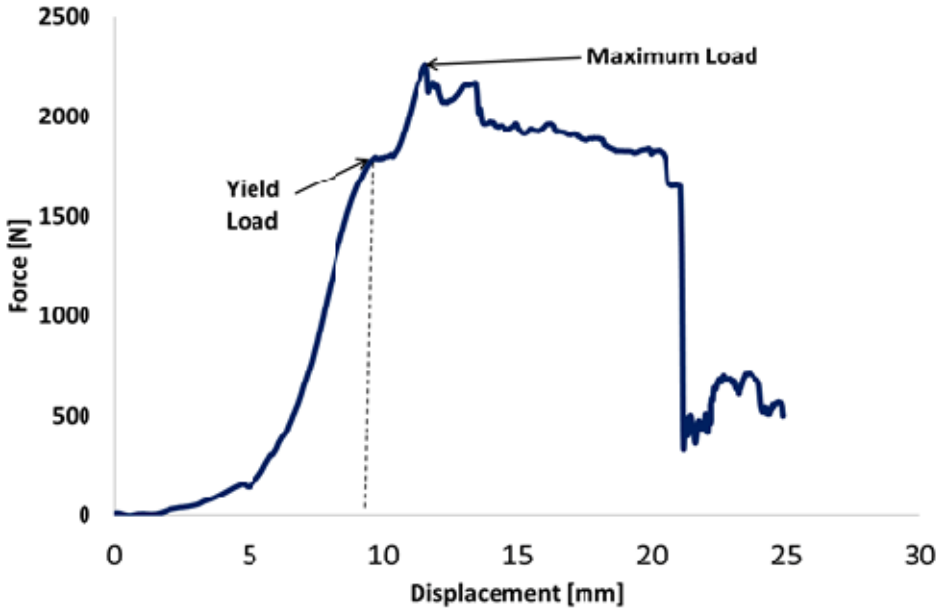

Figure 4.5: Representative force-displacement curve used to determine the yield and maximum energy and their corresponding energies

To evaluate the potential risk of thermal damage, we recorded the peak temperature of bone at each of the three regions of interest as well as the exposure time for temperature rise of 8°C, 10°C, and 12°C in these regions (Fig. 4.3).

4.3 Results

FE simulations predicted an average yield load of 1866(SD=359)N for the osteoporotic specimens of the control group (those left intact), while that of their augmented pairs prior to cementation was lower with an average of 1659(SD=453)N ($P = 0.039$). With some variations, the pre-operative plan recommended injection (drilling) paths that start from the vicinity of the supero-posterior aspect

of the greater trochanter and continue towards the superior part of the neck. The algorithm also suggested that a mean of 9.1(SD = 1.2)ml of PMMA injections adequate to increase the yield load of the osteoporotic specimens by an average of 73% (from 1659(SD=453)N to 2877(SD=345)N). Yield load values measured in mechanical testing were found to be linearly correlated with those of simulations ($R^2 = 0.77$) (Fig. 4.6). The fracture tests revealed that on average, augmented specimens have a 42% larger yield load (1951N vs. 2774N, $P < 0.001$) and 29% larger maximum load (2216N vs. 2853N, P=0.01) compared to those of the control group. Consequently, yield and maximum energy of the augmented pairs were larger by an average of 137% (4.4J vs. 10.5J, P =0.062) and 29% (24J vs. 30.9J, P= 0.23) respectively (Table 2.1). Figures 4.7 shows the results of fracture tests for the osteoporotic pairs. In most cases, femur fractures of the control group occurred in locations that are clinically defined as the intertrochanteric fractures [70]. The fracture locations were slightly different for the augmented pairs depending on the injection location. The osteopenic sample fractured from the inferior part of the femoral head (Figure 4.8). Femur specimens were registered to the segmented model of the bone with root mean squared errors of less than 1mm in all experiments. However, the error due to injector placement and pre-operative simulations yielded to an average distance error of 6.2 mm between the isosurface of planned and injected volume of PMMA.

Table 4.2: Results of femoroplasty: YL and ML represent the yield load and maximum load in N, respectively, and YE and ME represent the yield energy and maximum energy in Joules, respectively. Moreover, "Pre", "Plan", and "Post" represent the FE analysis based on the pre-operative CT, virtual CT created from the plan, and post-operative CT, respectively.

Sample	Control					Augmented					
	Simulation	Fracture test				Simulation			Fracture test		
	YL[N]	YL[N]	ML[N]	YE[J]	ME[J]	YL[N] (Pre)	YL[N] (Plan)	YL[N] (Post)	YL[N]	ML[N]	YE[J]	ME[J]
1	1500	1419	1706	2.90	20.07	1350	2785	1910	2282	2360	8.91	19.03
2	1825	2302	2497	3.77	26.97	1745	3330	2800	3003	3142	8.96	58.26
4	1815	1771	2253	4.22	28.72	1680	2830	2675	2685	2685	4.50	13.33
5	1725	2145	2145	4.90	19.08	1170	2395	2940	3087	3159	22.7	39.63
6	2465	2116	2481	6.37	25.17	2350	3045	3040	2812	2920	7.48	24.19
Mean	1866	1951	2216	4.43	24.00	1659	2877	2673	2774	2853	10.5	30.89
SD	359	355	322	1.3	4.2	453	345	448	317	336	7.0	18.2

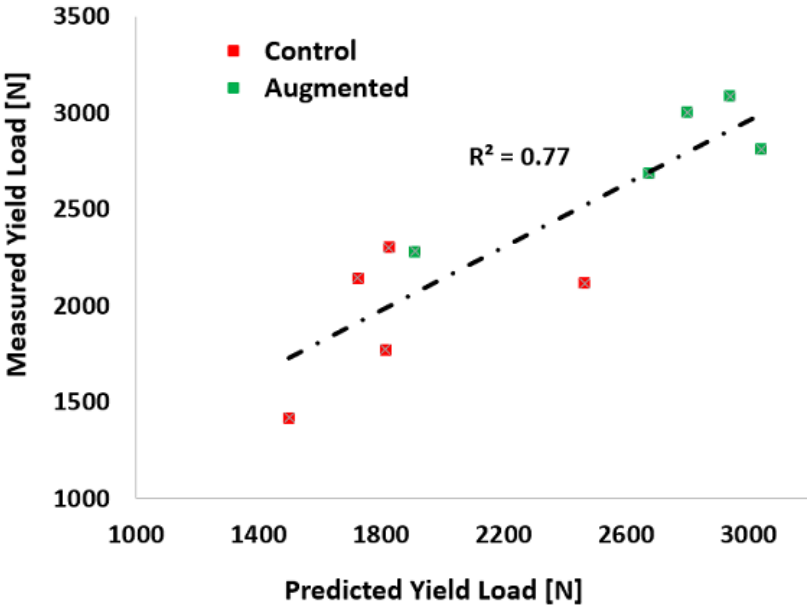

Figure 4.6: Measured vs. Predicted yield loads. The overall correlation coefficient is 0.77.

Temperature recordings of the bone surface shows that the areas close to the greater trochanter will experience the highest temperature rise with an average peak temperature rise of 12.1 °C. The trochanteric crest and femoral neck experience a lower temperature rise with an average peak rise of 6.17 °C and 5.26 °C respectively. In all experiments, greater trochanter area of the bone experienced a temperature rise of over 8 °C for an average period of about 9.2 minutes. In four specimens, this area experienced a temperature rise of over 10 °C. Meanwhile, these critical exposures were only observed in one specimen for the trochanteric crest. Table 4.3 details the summary of the peak temperature rises and duration of the critical exposures for all specimens.

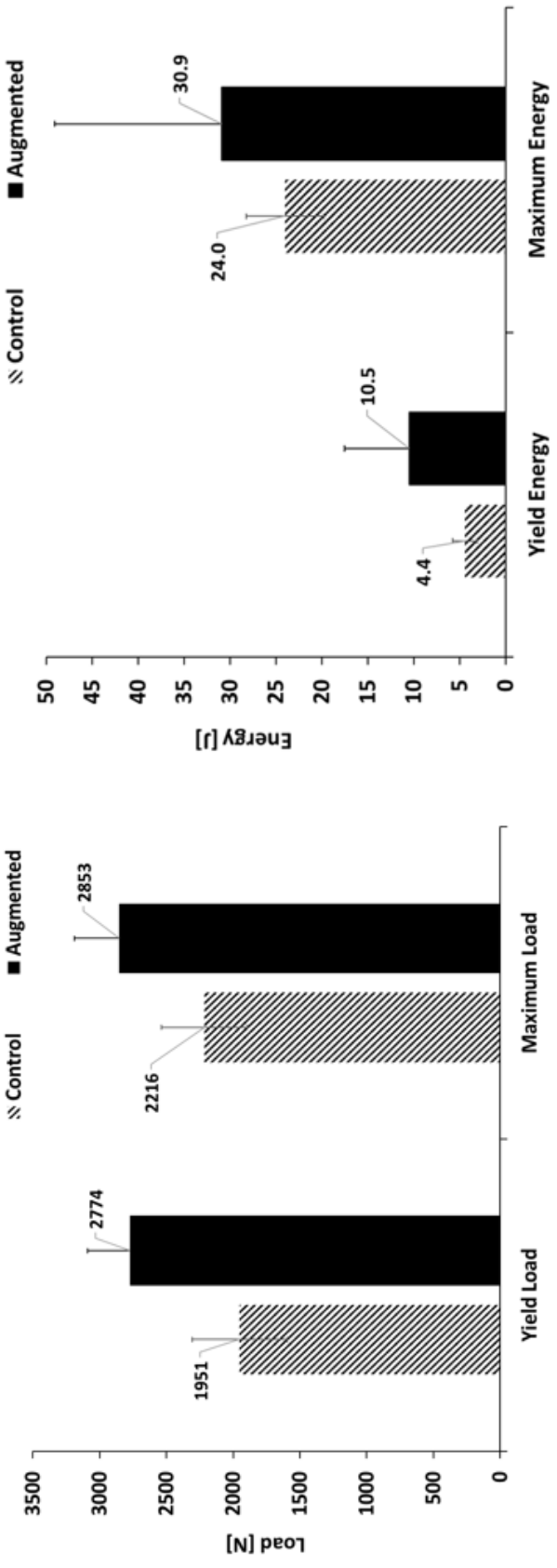

Figure 4.7: Effects of augmentation on yield and maximum load (left), yield and maximum energy (right) of the osteoporotic specimens measured in fracture tests. Error bars represent standard deviation.

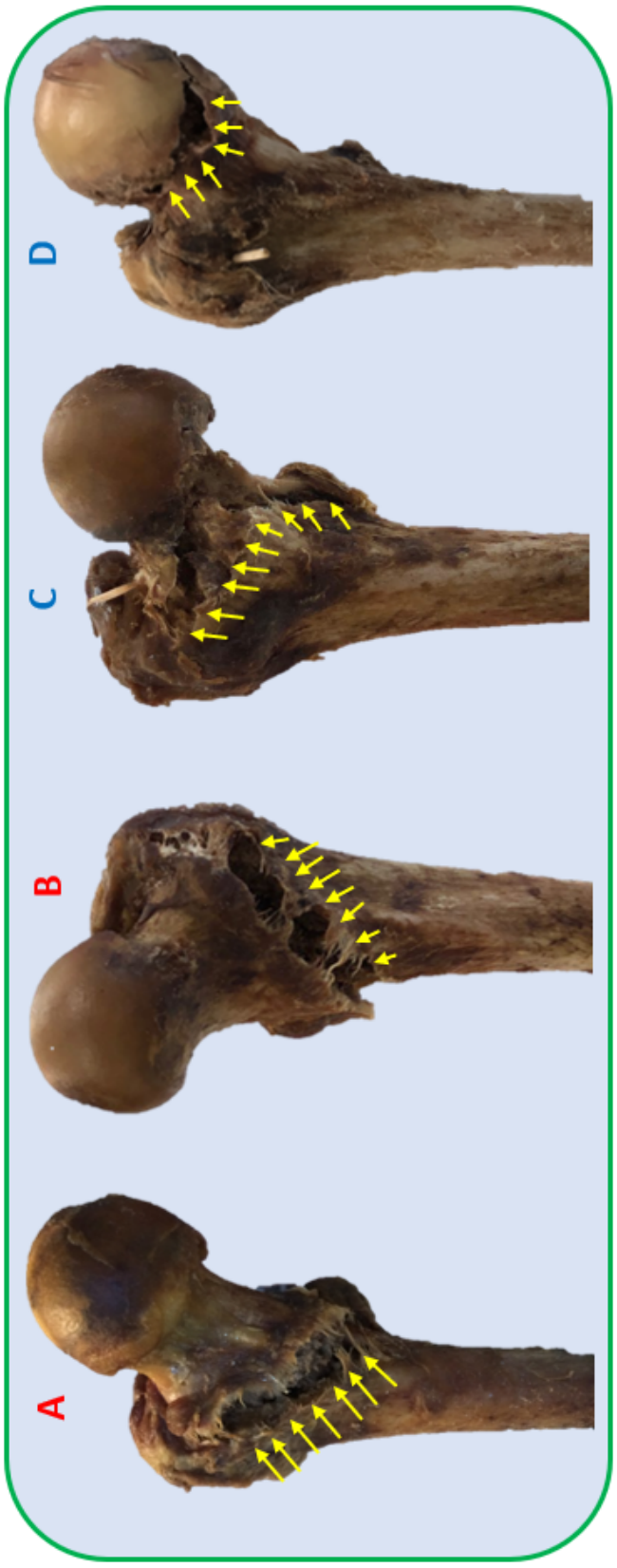

Figure 4.8: Patterns of fracture in side-way fall loading condition for A) Sample 1 from the control group, B) Sample 6 from the control group, C) Sample 6 of the augmented group; D) Sample 3 (osteopenic specimen). Note that the control samples experience an intertrochanteric fracture while the fracture pattern varies in the augmented group.

Table 4.3: Recorded temperature of the bone at the depth of 2mm from the surface at three anatomical regions. For the regions with potential risk of necrosis, exposure time of the temperature-rise was reported as well.

		Greater trochanter			Trochanteric crest			Neck
Sample	PMMA Volume [ml]	Peak Temperature rise[°C]	$> 8°C$ [Sec]	$> 10°C$ [Sec]	Peak Temperature rise[°C]	$> 8°C$ [Sec]	$> 10°C$ [Sec]	Peak Temperature rise[°C]
1	7.1	10.65	354	155	7.20	–	–	7.96
2	10.5	13.89	528	410	7.42	–	–	7.69
3	9.4	9.31	227	–	3.23	–	–	2.83
4	8.3	12.28	771	465	2.68	–	–	2.68
5	9.1	8.91	333	–	12.3	772	524	6.12
6	10.3	17.77	1121	831	4.16	–	–	4.26

4.4 Discussion

In this *in-vitro* study, we aimed to validate the fracture-related biomechanical outcomes of femoroplasty using a novel planning paradigm on human cadaveric femora with osteoporosis. The planning paradigm utilizes a gradient descent optimizer to determine a continuous pattern for PMMA injection. As expected, results demonstrated that osteoporotic specimens benefit greatly from injections that connect the supero-posterior aspect of the greater trochanter to the inferior aspect of femoral head. This distribution of bone cement is similar to the findings of other patient-specific plans [16, 56]. The biomechanical effectiveness of injections is comparable to those of Basafa et al. [16] where local optimization defined the location of three static injections and an average of 9.5 ml of cement increased the yield load by 33% and yield energy by 118%. The outcomes for these parameters have been improved by respectively 27% and 16% in the current study while the injection volume was reduced to 9.1 ml. Furthermore, the new plan did not require a second drill hole for any of the specimens. Findings also showed that bones with lower neck t-score benefit greater from the augmentation. Although the investigation was beyond the scope of this study, it was determined that the osteopenic sample does not benefit from the augmentation. This femur fractured from the inferior part of the head which was different from the osteoporotic femora of

both control and augmented groups (Fig. 4.8).

Previous studies have established that thermal necrosis may occur when tissue is exposed to temperatures higher than 60 °C. That is equivalent to temperature rise of approximately 23 °C. Lower temperatures can still cause necrosis depending on the exposure time [49]. Notably, temperatures of 45 °C (rise of 8 °C) for over 600 s, 47 °C (rise of 10 °C) for over 60 s, and 50 °C (rise of 13 °C) for over 30 s lead to necrosis [49]. Temperature recordings of bone surface in this study allowed for a quantitative assessment of this risk. Results presented in table 3 indicate that all injection scenarios except that of specimen 3 may risk thermal damage at the greater trochanter or trochanteric crest region of the bone. Future work will include addition of a FE model to predict the bone temperature (e.g. [64]) to the existing planning paradigm in order to remove the risk of thermal damage. In addition, integration of a cooling system with femoroplasty can extend the polymerization time of PMMA, thus reducing the risk of thermal necrosis due to the temperature rise. Approaches for integration of a cooling system have been previously used for vertebroplasty [71]. It is important to note that our temperature rise estimation may be over-estimations since 1) initial tissue temperatures in all *in-vitro* experiments of this study averaged 21 °C, well below the normal body temperature (37 °C); and 2) lack of blood flow results in higher temperatures in cadaveric experiments. A more realistic evaluation of necrosis risk may be achieved

through live tissue injections of PMMA.

The current study focused on PMMA based femoroplasty which is shown to be effective in several computational and experimental studies [12, 13, 16]. However, a recent study showed that injections of biphasic calcium sulfate /hydroxyapatite (CaS/HA) in the proximal femur is also feasible and may lead to reduction in fracture risk if cement is injected optimally [53]. Additionally, study of Stroneck et al. [72] proposed a triphasic calcium-based implant as an alternative approach material that is designed to replace the bone loss due to osteoporosis. Combination of such materials with the planning and injection techniques proposed here can lead to a faster clinical adoption for femoroplasty.

Among other limitations of this study is the accuracy of cement injection based on the plan. The average shape error between the injected and planned path of cementation remains relatively large in this study (6.2 mm average distance error). While the overall planning paradigm has been improved, intraoperative execution of the plan remains a challenge. Although specimens were injected with the same volume of cement as planned, direction and location of cementation is different from desired path, lowering the biomechanical benefits of augmentation. Since both bone and tool registrations have errors that average $<$1mm, it can be assumed that the error of the user drilling with provided visual feedback and injector placement are the major contributing factors for the injection accuracy. Therefore, use of a robotic system for drilling and injec-

tion of bone cement may increase the accuracy of cementation, thus improving the overall reliability of the procedure by improving the biomechanical benefit and reducing the risk of cement leakage. The simplifying assumptions made in the SPH and errors in cement segmentation are other sources of error.

4.5 Conclusion

To summarize, this study shows that a planned injection of PMMA into the proximal femur can significantly improve its fracture-related biomechanical properties (yield load and yield energy). The new planning paradigm offers a more efficient injection strategy with injection volume of 9.1 ml on average. Meanwhile, temperature recordings of bone surfaces suggest that risk of thermal necrosis remains as a concern with PMMA-based femoroplasty. This may require additional provisions (e.g., a cooling mechanism) to lower the curing temperature. Future work involves incorporating modes that predict bone temperatures and conducting surgical interventions that aim at lowering those temperatures during femoroplasty.

4.6 Recapitulation of Contributions

The author's contributions in this chapter are as follows:

- Biomechanical planning for six pairs of cadaveric femora based on the patient-specific strategy described in chapter 3.
- Performing augmentation experiments on weaker bone from each pair according to the plan.
- Evaluating and analyzing the bone surface temperature rise during cement polymerization in cadaver experiments.
- Conducting invasive biomechanical testing to evaluate the outcome of augmentation on fracture-related properties of the bone.

Dr. Ryan Murphy implemented the navigation software used in the cadaver experiments in 3D-Slicer. Dr. Ehsan Basafa and Ms. Mahsan Bakhtiarinejad helped the author in performing the injection experiments.

Chapter 5

Heat Transfer Analysis for Femoroplasty

5.1 Introduction

As discussed in the previous chapters, higher volumes of PMMA injection may introduce the risk of thermal necrosis. Prior studies have pointed out that the temperatures in the range of 45 °C to 60 °C may cause thermal tissue damage, depending on the exposure time [65, 66]. Therefore, in addition to the mechanical strength of the femur, maximum temperature-rise and duration of thermal exposure are important factors that needs to be considered while planning the injection for femoroplasty.

Previous studies have developed simulation models to study the temper-

ature distribution after cementation with PMMA both in 2D and 3D, most of which have considered cement and bone as homogeneous continuum materials and the bone-cement-interface is often characterized by its conductivity [73, 74]. Baliga et al. [73] presented a methodology for numerical simulation of unsteady heat conduction in PMMA during its polymerization and demonstrated an agreement between the numerical predictions and the corresponding experimental results. Hansen et al. [74] proposed a general model for acrylic cementation in hip-joint-replacement surgery based on the principles of polymerization kinetics and heat transfer. The validity and capabilities of such methods has inspired us to consider FE heat transfer modeling as a potential approach for predicting the temperature rise during cementation, thereby lowering the risks associated with femoroplasty.

This chapter first presents a 3D heat transfer simulation model for bone temperature evaluation during femoroplasty. The modeling approach is then evaluated through direct measurements of bone surface temperature in experiments where bone injection profiles are customized based on a novel planning paradigm for bone augmentation. [1]

[1] Majority of the work presented in this chapter is published as [64] and [75]

5.2 COMSOL Simulations

Following the injection experiments discussed in the previous chapter, another set of CT scans of the proximal femur were obtained. These scans were used to segment the injected PMMA along with the bone surface in an open-source software MITK (German Cancer Research Center, Heidelberg, Germany)(Fig. 5.1). Next, an FE heat transfer model was created to estimate the bone surface temperature at every one second interval following cement injection in COMSOL Multiphysics, Inc (Burlington, MA). For this purpose, we assumed a homogeneous material property inside the bone and a uniform heat flux from the bone-cement-interface towards the cortical shell. For the conductive heat transfer between the tissue and PMMA, COMSOL solves the following equations:

$$\rho C_p \frac{\partial T}{\partial t} + \rho C_p u \cdot \nabla T + \nabla \cdot q = Q + Q_{ted} \tag{5.1}$$

$$q = -k \cdot \nabla T \tag{5.2}$$

where ρ is the density in kg/m^3, C_p is the specific heat capacity of the material at constant pressure in $J/(kg.K)$, T is the absolute temperature, u is the velocity field vector in m/s, q is the conductive heat flux in W/m^2, Q is the heat source (PMMA exothermic reaction) in W/m^3, and Q_{ted} is the heat source as the result of thermoelastic effects in W/m^3. Table 5.1 shows the constant material properties used for this simulation.

Table 5.1: Material properties of the bone used in FE simulations

Property	Value	Unit
Thermal Conductivity (k)	0.6	$W/m.K$
Density (ρ)	1000	kg/m^3
Heat capacity at constant pressure	2200	$J/(kg.K)$

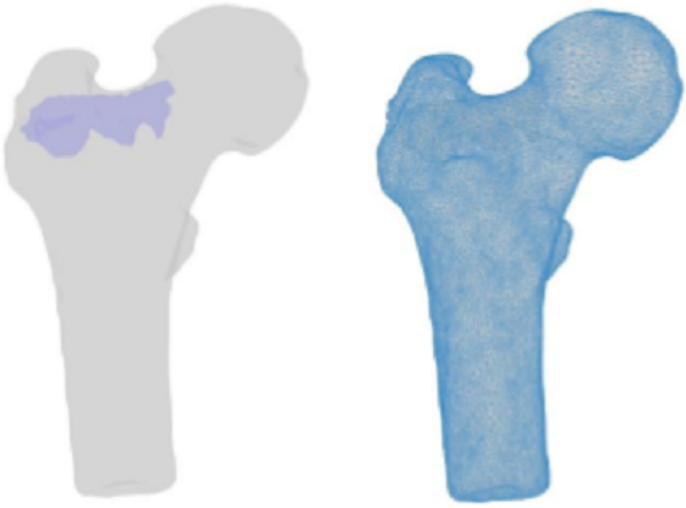

Figure 5.1: Segmented geometries of the bone and PMMA (left) FE mesh of the bone geometry (right). Note that the FE mesh was created using the largest mesh size that would produce the converging results.

PMMA curing temperature profile at the bone-cement-interface was directly measured in a 130 mm by 45 mm by 40 mm open cell block (7.5 PCF) (Sawbone Inc., Vashon Island, WA), resembling human cancellous bone where $30cm^3$ of canola oil was added to the block mimicking the bone marrow. This data was later used in simulations to estimate the bone surface temperature.

5.2.1 Model Validation

To validate the COMSOL model, we used direct temperature measurements from the first two cadaver experiments discussed in chapter 4. From planning, it was determined that 7.7cm^3 of PMMA is sufficient to increase the yield load of the first specimen by 67% (from 1350 N to 2256 N). For the second specimen, 9.1cm^3 of PMMA results in 105% of yield load increase (from 1170 N to 2395 N). Planning also suggested that the yield energy of these specimens increases by 161% and 116% respectively. Temperature measurements for the first specimen indicated that greater trochanter's temperature rises about 10°C about 12 minutes after the start of injection. Maximum temperature-rise at the femoral neck and trochanteric crest were 7.1 °C and 5.9°C respectively. Temperature profiles of this specimen were estimated in the FE simulation with an average error of 1.87°C at the Trochanteric crest, 1.23°C at the greater trochanter and 2.1°C at the femoral neck. Temperature distributions of the bone surface after injection are estimated at different time intervals (time after injection) and illustrated in Figure 5.2. Note that most of critical temperature-rises occurs at the superior and inferior aspects of the neck as well as supero-posterior aspect of the greater trochanter.

To further validate the model, we compared the temperature measurements of the second specimen with those of FE simulations. As shown in Figure 5.3, estimated temperatures of the second specimen at greater trochanter and

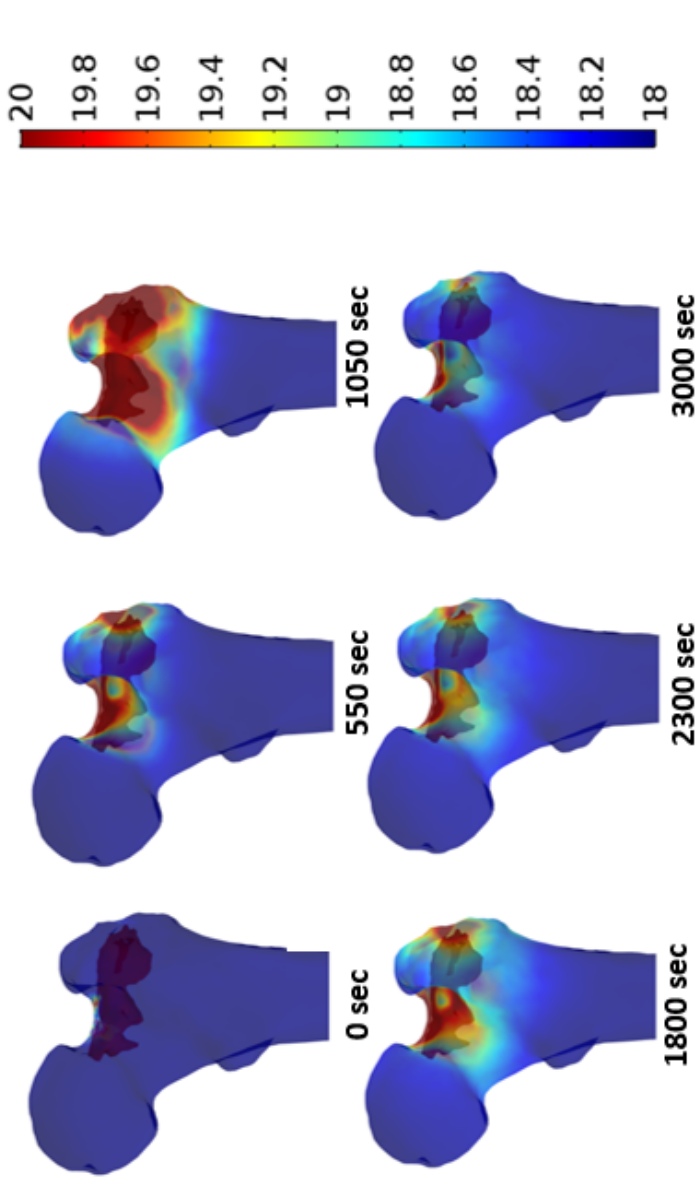

Figure 5.2: Surface temperature-rise of the femur during PMMA Polymerization.

trochanteric crest matches those of the measurements. Maximum temperatures of bone surface at different time intervals following the injection were extracted from simulations and are shown in Table 5.2.

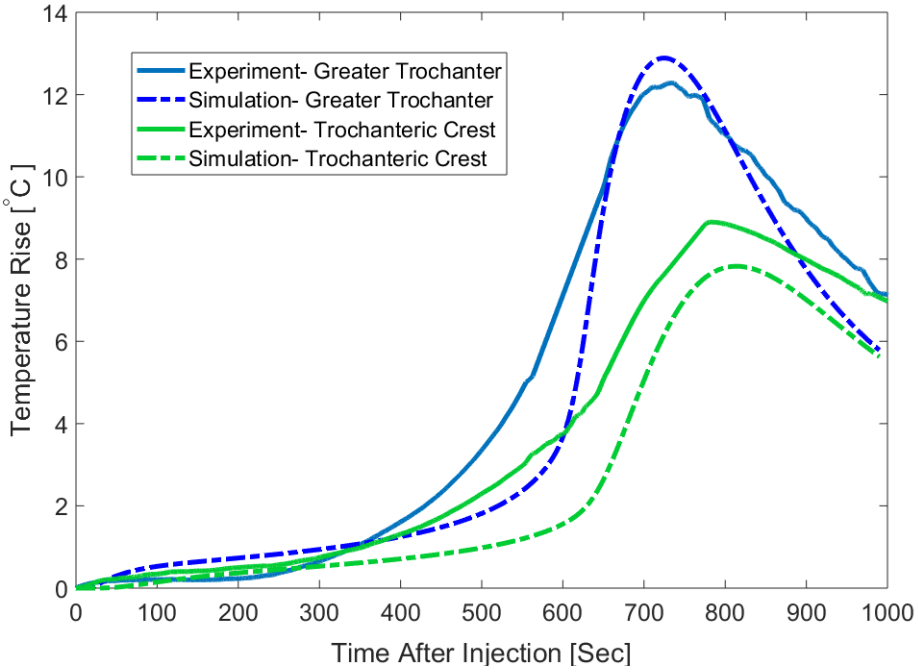

Figure 5.3: Surface Temperature-rise of the Second femur specimen for the first 1000 seconds after the injection- Experimental results vs. predicted values.

Table 5.2: Maximum temperature-rise of the bone at discrete time-intervals following PMMA injection

	Maximum temperature rise [°C]	
Time[s]	Specimen 1	Specimen 2
0	4.34	4.08
550	25.75	25.75
1050	26.67	29.15
1800	12.51	12.47
2300	9.09	9.07
3000	6.34	6.32

5.2.2 Discussion

The preliminary experiments on two femur specimens indicate that lowering volume of PMMA may reduce the risk of thermal necrosis. For the first specimen where 7.6 cm^3 of bone cement was injected, the maximum temperature-rise is 10°C which occurs at about 780 seconds after the injection. The exposure time for this rise is less than 30 seconds which is well below the levels causing thermal necrosis [49, 76]. In the second injection experiment, greater trochanter of the femur was exposed to temperatures above 10°C for over 200 seconds. Therefore, the thermal necrosis can be expected for these injection scenarios which confirm the potential need of cooling technique during cementation. For the heat transfer model, we have assumed a homogeneous material property for the bone tissue. The parameters shown in 5.1 were estimated and modified based on the direct temperature measurements of the bone surface. To validate the simulation results, we compared the temperature measurements on the surface of the second femur with corresponding temperatures from the FE simulation without further modification of the material properties (Fig. 5). One of the limitations of the in-vitro experiments presented in this study was the base-temperature of the bone tissue during the injection (about 22°C) that is well below the 37°C body temperature. In addition, lack of blood flow in cadaver specimens may result in an increased temperature-rise during PMMA curing. Previous studies pointed out that thermal necrosis is

expected when tissue is exposed to more than 60°C [49]. Therefore, with the temperature-rise values shown in 5.2, both injection scenarios may result in tissue damage. Among other limitations of this study was the technique used to fix the thermocouple on the bone surface prior to each injection experiments. Points of measurements were manually selected in the regions of interest and localized through X-ray images of the bone. Therefore, the verification of the location of the maximum temperature in the bone, as determined by simulation, was not possible.

5.3 Conductive Cooling Scheme

It is apparent that increasing the curing time of PMMA results in lower maximum temperatures for both the cement and surrounding bone tissue. In the study of Langdown et al., it was shown through in-vivo experiments that there is an inverse relationship between ambient temperature and the setting time for Simplex cement (Stryker Orthopaedics, Mahwah, NJ) [77]. Moreover, Chavali et al., proposed a technique in which loaded syringes of PMMA were placed in an iced sodium chloride bath, extending the PMMA curing time to over 2 hours in percutaneous vertebroplasty [71]. Although the main purpose of their technique was to increase the injectability time of the cement, it is expected that the temperature-rise of the tissue will also reduce. In a simi-

lar study, Lai et al., studied the effects of precooling (i.e. lowing the initial temperature of the liquid) and ice bath cooling (lowering the surrounding temperature) on the curing time of PMMA and found both techniques effective for percutaneous vertebroplasty [78]. These techniques, however, may not be suitable to be used for OHA because of two major limitations. First, the curing-time alterations of up to 2 hours can change the biomechanical properties (i.e. elastic modulus) of the bone cement which is important for OHA as a preventive approach. Second limitation is that surgeons have no control over the cement temperature after injection and, therefore, potential risk of osteonecrosis remains. To address the issue, we proposed a novel bone augmentation cooling scheme for OHA to lower the PMMA's curing temperature after cement injection and, therefore, reducing the risk of thermal necrosis. We aim to validate the proposed cooling system through in-vitro experiments and the simulation model discussed in the previous section. We performed FE heat transfer simulation of the proposed cooling mechanism in three-dimensional (3D) models of the femur with injected PMMA and compared the temperature-rise of the bone against models without using the cooling system. Moreover, we performed controlled sawbone experiments with a K-wire via a conductive heat transfer to examine the feasibility of the proposed cooling system. The metallic k-wire is attached to an ice-water bath and inserted through the injected PMMA in the drilled tunnel immediately after the injection. The schematic illustration of

the cooling system is shown in Figure 5.4.

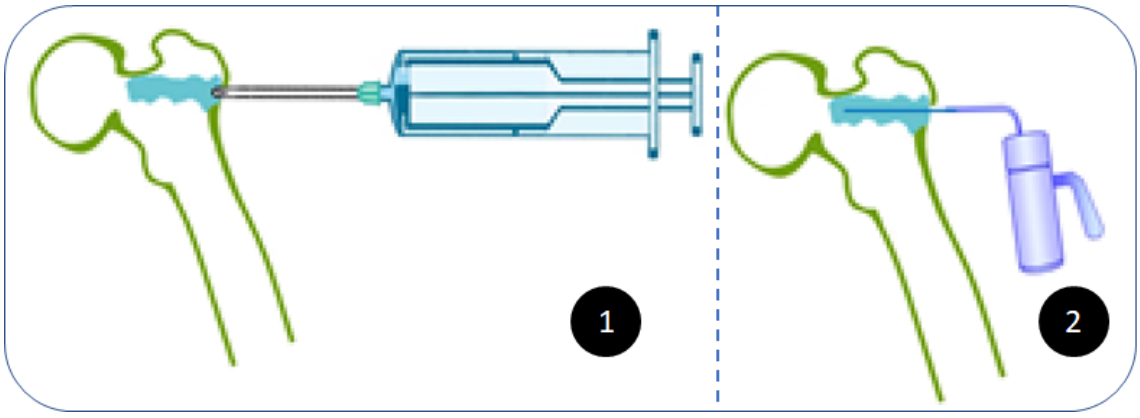

Figure 5.4: Schematic Illustration of the proposed cooling system. In the first step (left), bone cement is injected through the planned path and then K-wire attached to the ice-water bath is inserted in the drilled tunnel right after the injection (right).

5.3.1 Geometrical Modeling and FE Simulations

For the purpose of temperature estimation simulations, we used Post-op CT of two femur specimens to create FE heat transfer models as described in section 5.2. Through a threshold-based segmentation of the bony anatomy, the domains of the femur and injected PMMA were identified using image processing software; MITK (German Cancer Research Center, Heidelberg, Germany). We then improved the segmentation by manual refinement and created smoothed 3D models of each femur with associated PMMA. Next, we placed a stainless-steel k-wire with 3mm thickness diameter based on the location of the opti-

mized drilled path that is identified through the planning paradigm. Consequently, the K-wire is inserted through the injected PMMA. The FE model of the two specimens with the associated segmented PMMA are generated using linear tetrahedral elements in COMSOL Multiphysics (COMSOL AB, Stockholm, Sweden). Figure 5.5 demonstrates three-dimensional FE model of the femur together with the injected PMMA and metallic K-wire inside the cement. The femoral bone, PMMA and 301 Stainless steel K-wire elements are assumed linear and isotropic with the homogeneous material properties shown in Table 5.3.

The heat transfer simulation is performed in two steps.: In the first step, the temperature-rise estimation of the bone during cement augmentation is performed. We also calculated total heat flux generated using temperature profile of the bone-cement interface. We then simulated the bone augmentation cooling process via conductive heat transfer to investigate the effect of cooling on the bone temperature-rise. For this purpose, we imported and implemented the heat flux profile as a heat source to the bone-cement interface and assigned 0°C constant temperature to the metallic K-wire surface so that the cement augmentation and cooling procedure are performed simultaneously. Similar to the previous step, time-dependent simulation is carried out at one second interval during hip augmentation procedure.

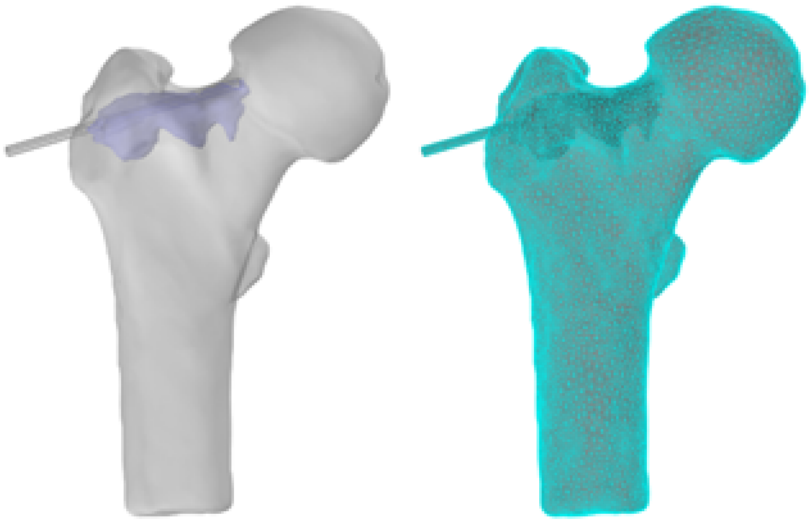

Figure 5.5: 3D Geometrical and FE mesh of the femur with segmented PMMA and k-wire

Table 5.3: Summary of the material properties involved in cooling simulations

Property	Unit	Bone	PMMA	301 Stainless Steel
Thermal Conductivity (k)	$W/m.K$	0.6	0.2	16.3
Density (ρ)	kg/m^3	1000	1190	8030
Heat capacity at constant pressure	$J/(kg.K)$	2200	1420	500

5.3.2 Sawbone Experiment

To better investigate the functionality and feasibility of the proposed cooling system, we conducted a controlled sawbone experiment using 3mm metallic K-wire attached to an ice-water bath. For this purpose, 15 cm^3 of PMMA was injected uniformly into a 130 mm x 45 mm x 40 mm of an open cell block (7.5 PCF) resembling the human cancellous bone. Before injection, 30 cm^3 of canola oil is added to the block mimicking the bone marrow.

In this setup, temperature profile of the bone-cement interface is measured using k-type thermocouples at 3 locations. Next, similar experiment was performed incorporating the aforementioned cooling system to the augmentation setup (Figure 5.6, right). Prior to the injection, the metallic K-wire is placed in a mixture of ice water bath for 5 minutes to ensure that the temperature of the K-wire prior to insertion is 0° C. We then insert the K-wire through the drilled tunnel keeping it in contact with the injected cement while the end of the K-wire is kept in the ice-water bath. In order to avoid K-wire to adhere to the PMMA during cement polymerization, we rotate the K-wire gently in a uniform motion while inserting it through the foam block.

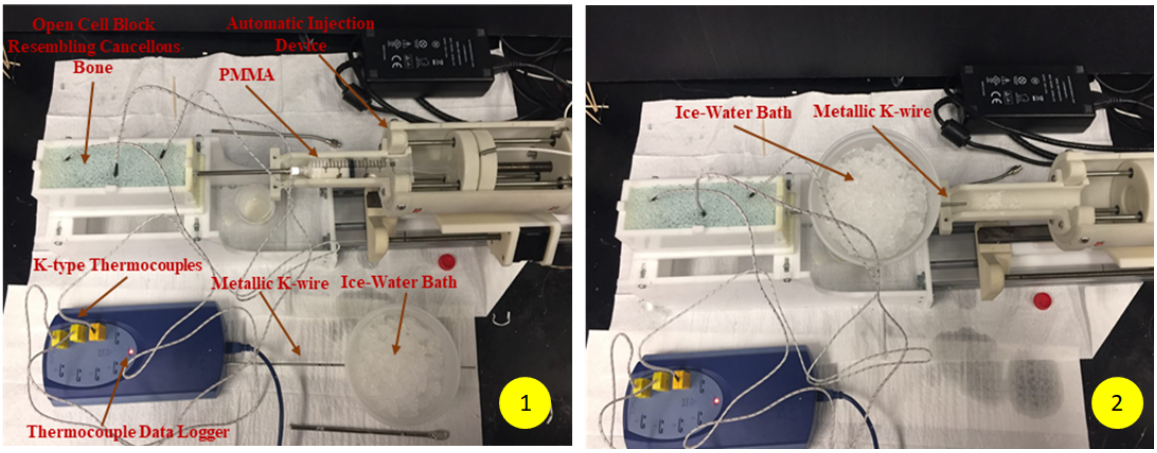

Figure 5.6: Cooling Experimental Setup: Cement Injection with (left) and without (right) the cooling system.

5.3.3 Results and Discussion

During both steps of the simulation, we measured temperature-rise of two specimens at three key locations. For specimen 1, maximum temperature-rise were reported as 4.3°C, 5.8°C and 9.7°C at the femoral neck, introchanteric crest, and greater trochanter respectively. These temperatures were lowered to 0.9°C, 1.2°C and 2.1°C respectively when the augmentation setup is incorporated with the cooling system. Figure 5.8 demonstrates the comparison between the temperature-rise of the augmentation model with cooling system and the control augmentation without cooling at three key locations.

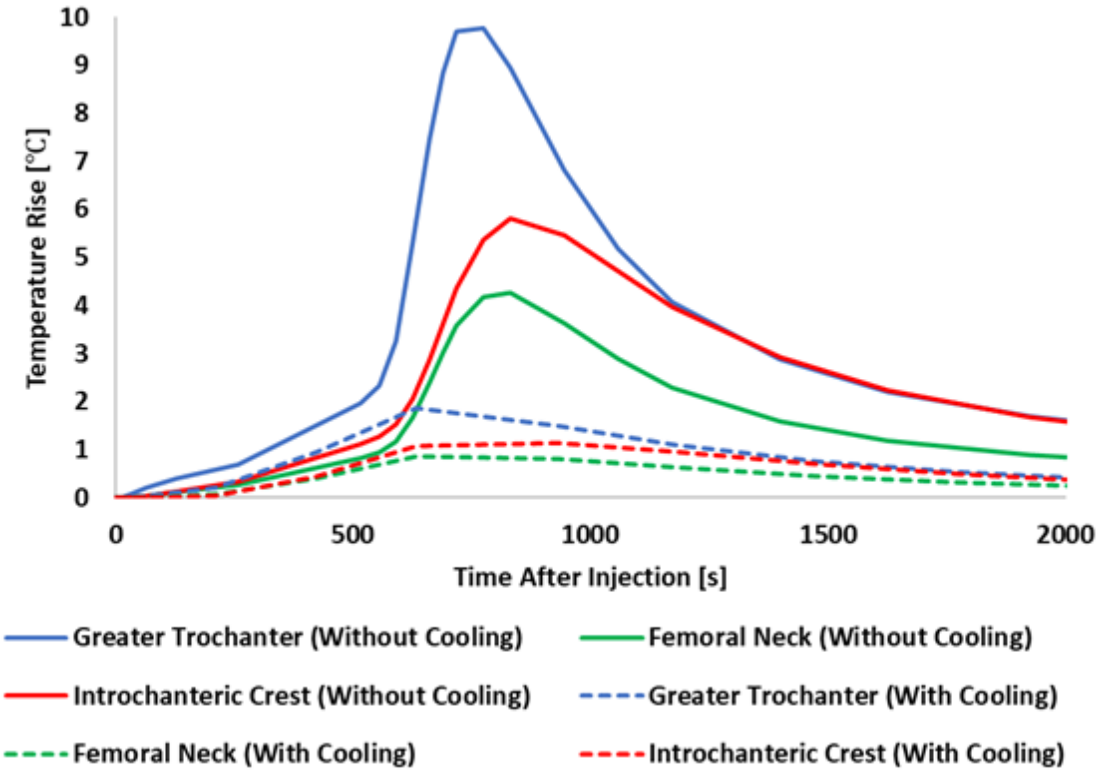

Figure 5.7: Predicted temperature of the specimen 1 for the first 3000 seconds after injection with and without the cooling

Both femoral bone specimens exhibit similar temperature distributions after the cement injection. In simulations, temperature-rise of the specimen with cooling was significantly lower than those without cooling. The Maximum temperature of both specimens are compared to those without cooling in Figure 5.8. The maximum temperature-rise in both models occured at the superior and inferior domains of the neck as well as superior posterior portion of the greater trochanter. Furthermore, Figure 5.9 compares the geometrical distribution of the temperature of the augmentation model with the cooling system against the model with no cooling at the time interval of 1050 seconds.

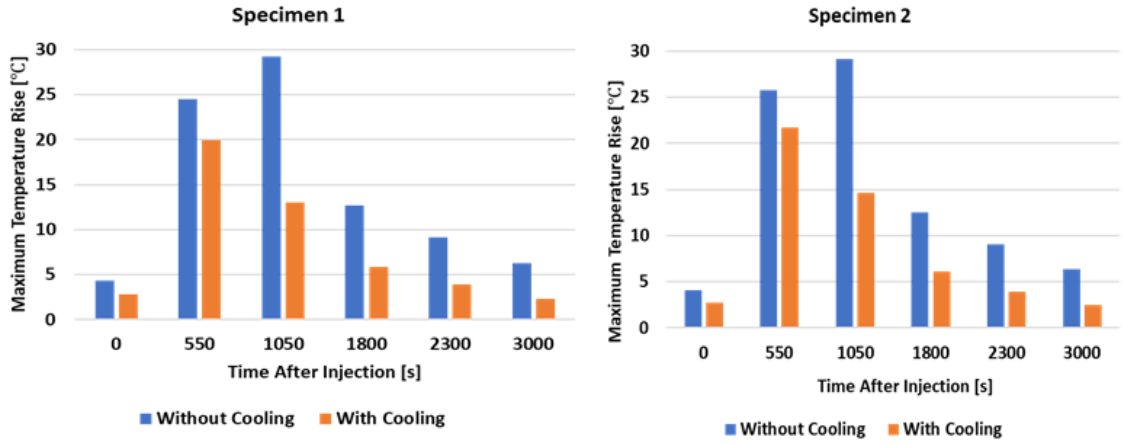

Figure 5.8: Simulated maximum temperature with cooling vs. without cooling

In the pilot sawbone experiments, fluoroscopic images were captured after augmentation and temperature values were measured using three K-type thermocouples at sawbone-cement interface in one second intervals (Figures 5.10 and 5.11). We performed two sets of experiment to investigate the effect of

rotating the K-wire on the temperature measurements. The investigation of temperature-rise profiles of thermocouples TC1, TC2, and TC3 confirms that the peak temperature of the sawbone-cement interface has been substantially decreased when cooling system was integrated to the bone augmentation setup (TC1 64%, TC2 34% and TC3 69%). Moreover, the corresponding time of the maximum temperature has also been reduced. Similarly, in the second experiment, when the k-wire rotated about its own axis, the peak temperatures were also substantially decreased in all three thermocouples. However, curing was delayed when compared to the first case and the pattern of injection is affected due to the speed of the rotation which can be controlled in the future.

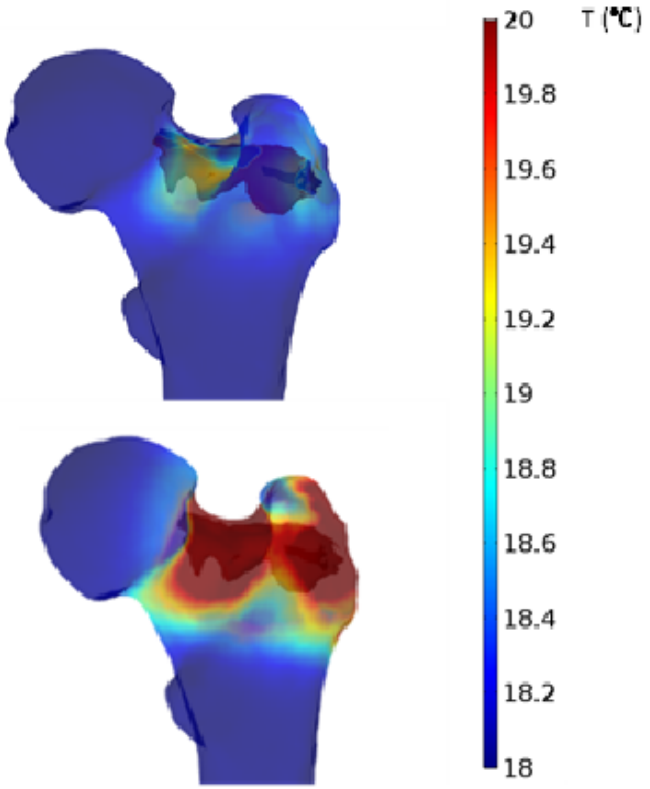

Figure 5.9: Temperature distribution of the femoral bone during PMMA polymerization with (top) and without (bottom) the cooling.

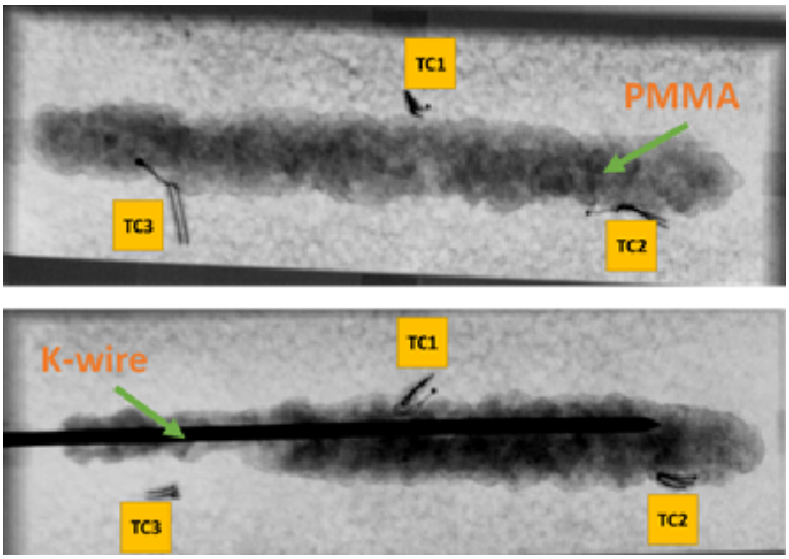

Figure 5.10: X-ray images of PMMA profile inside the open cell foam block (Sawbone) without cooling(top) vs. with cooling (bottom). Note that the location of thermocouples (TC1, TC2, and TC3) were the same in both experiments.

As shown in Figure 5.8, the temperature-rise of the simulation model with incorporated cooling system has been reduced about 80% in all three locations compared to those of the control augmentation with no cooling. Therefore, the simulation results confirm that the critical temperature-rise emerging at the femoral neck and greater trochanter has been reduced substantially when using the cooling system. Moreover, it is important to point out that the cooling is applied throughout the duration of the bone augmentation. In the future work, the duration of the cooling phase can be optimized to reduce the thermal effect of cement polymerization while maximizing the mechanical strength of the PMMA augmentation.

Both simulation and experimental findings reinforce the fact that integrat-

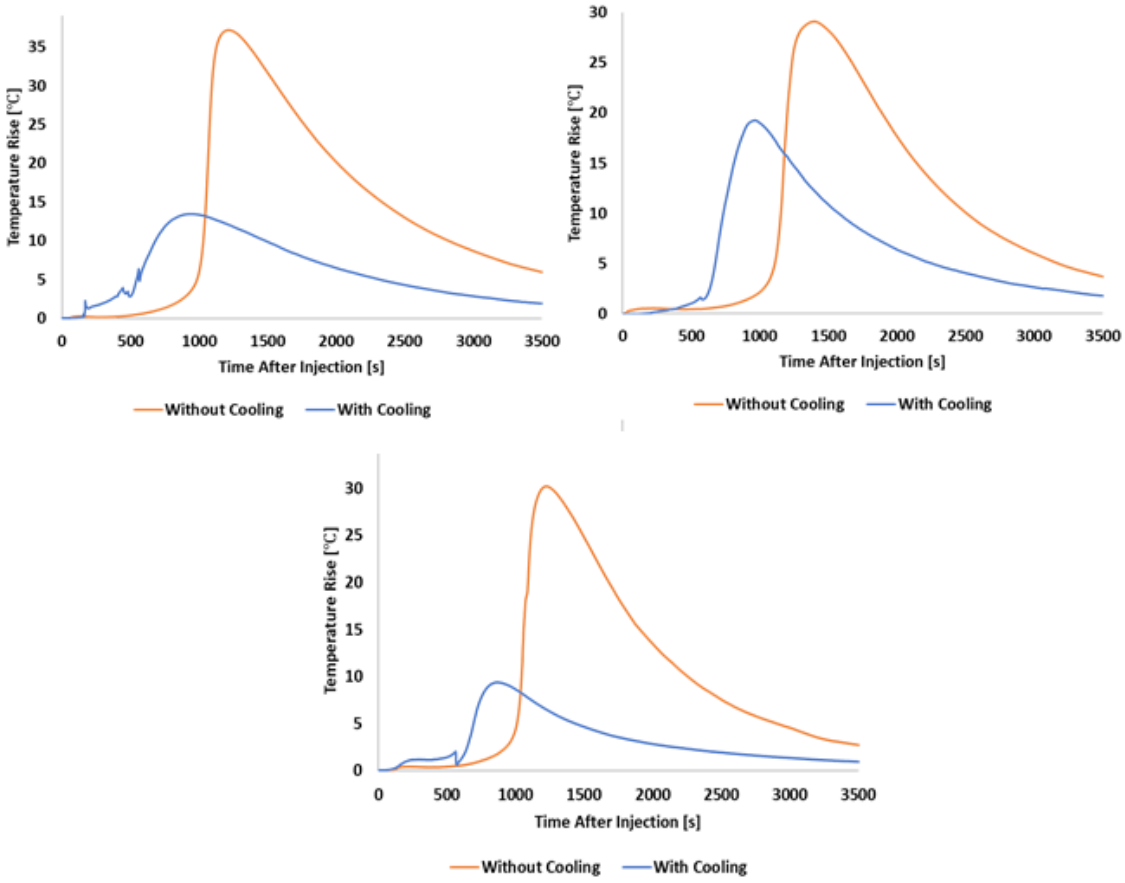

Figure 5.11: Temperature-rise measurement of the 3 thermocouples at saw-bone cement interface with cooling vs. without cooling: TC1 (left), TC2 (middle), and TC3 (right)

ing the cooling system to the bone augmentation set-up has noticeably declined the peak temperature-rise that usually occurs 10-12 minutes after the injection. In addition; it is also revealed that there are various criteria that affect the cooling system including but not limited to the duration of the cooling applied, the speed and frequency of rotation of the K-wire, all of which needs to be explored in more detail in the future experiments and simulations. Furthermore, due to the fact that points of temperature measurement are randomly

selected in the regions of the interest, importing the accurate locations of the K-wire in simulation is not possible. Moreover, the distance between the bone-cement interface and fixed positions of thermocouples can affect the peak temperature measurement during injection; therefore, the technique to place the K-wire in in-vitro experiments at regions of interest can be enhanced by 3D optical tracking and navigation. With navigation we could accurately locate the position of K-wire in the simulation to acquire a comprehensive understanding of the maximum temperature-rise.

The preliminary simulation of the cooling system demonstrates a promising agreement with in-vitro sawbone experiments. In the future, the proposed bone augmentation cooling system need to be experimentally validated through cadaveric femoral augmentation and evaluated against the simulation model.

5.4 Conclusion

We have developed an FE model capable of estimating the bone surface temperature based on a given pattern of injection. This model is validated through direct measurements via K-type thermocouples and can be used to avoid injection scenarios that may result in thermal necrosis. In future studies, this model can be integrated into the planning paradigm to lower the risk of tissue damage. In addition, we introduced a novel bone augmentation cooling scheme

for osteoporotic hip augmentation, capable of reducing the PMMA's curing temperature after the injection. FE heat transfer models were developed to integrate the cooling system with the augmentation. The proposed cooling system was tested through sawbone in-vitro experiments demonstrating the satisfactory performance and feasibility of the incorporated cooling systems for femoroplasty. The proposed bone augmentation cooling methodology can be used to reduce the risk of thermal necrosis due to the excessive temperature-rise.

5.5 Recapitulation of Contributions

The author's contributions in this chapter are as follows:

- Developing a 3D heat transfer model in COMSOL to simulate the effects of femoroplasty on surface temperature of the proximal femur.
- Validating the model performance through comparison of the simulation results with direct temperature recordings of the bone in two cadaver experiments.
- Introducing a conductive cooling approach to reduce the PMMA's curing temperature after cement injection.
- Conducting sawbone experiments to evaluate the efficacy of the cooling approach.

Ms. Mahsan Bakhtiarinejad helped the author in performing the injection experiments and analysis of the simulation results. Ms. Mahsan Bakhtiarinejad and Mr. Alireza Chamanni integrated the cooling mechanism to an early version of the heat transfer model developed by the author (results shown in Figure 5.8)

Chapter 6

Curved Injection Paths

6.1 Motivation

To this end, all femoroplasty studies, including the planning paradigm discussed in chapter 3 have considered injections that occur on a straight line (e.g. [16, 44, 46, 56, 58]). This, however, can significantly limit the overall match between the desired cement pattern and the injected volume. With new tools developed for Minimally Invasive Surgery (MIS), it has been made possible to plan and drill the bone based on a curved trajectory [79]. The goal of this study is to develop a new optimization algorithm for femoroplasty using a curved pattern of PMMA injection. We aim to test the proposed algorithm using a previously validated modeling technique described in section 3.2.1.[1]

[1] Majority of the work presented in this chapter is published as [80]

6.2 Methods

6.2.1 Optimization of the Injection Trajectory and Rate

Four pairs of cadaver femora were obtained from the Maryland State Anatomy Board. Specimens were cleaned of soft tissue and CT scanned (Toshiba Aquilion One, Canon Inc., Tochigi, Japan). We estimated the yield load of each femur using the FE modeling approach described in chapter 3 and selected the weaker bone of each pair for augmentation. Augmentation planning consisted of two main phases. Table 6.1 shows the samples demographics along with their yield loads.

Table 6.1: Sample demographics and predicted yield load of the selected femora for augmentation.

Sample	Age	Gender	Pre-injection yield load [N]
1	89	F	1495
2	69	F	1745
3	72	F	1165
4	92	F	1815

In the first step, the ideal cement distribution is defined with respect to the bone elements using a modified method of BESO [81]. This FE-based optimization algorithm estimates the yield load of the bone after each iteration and algorithm continued until the yield load drops below twice of its biomechanical state prior to augmentation. At that point, a list of cemented elements is

recorded. Figure 6.1 shows a potential region of the bone selected for augmentation.

Figure 6.1: Sagittal (left) and axial (right) view of FE mesh with desired cement elements (green) selected based on the method of BESO.

In the second step of planning, we use BESO results to determine the 3D trajectory and injection parameters required for the clinical practice. For this purpose, we start by creating a 3D virtual volume of the bone volume and assigning value of 1 where there are cement elements and zeros elsewhere. Next, we create an isosurface of the cement elements (Figure 6.2a). This can be coupled with a selection of a Region of Interest (ROI) to ignore cement elements in the lower part of the femur. Using coronal planes, we divide the cement volume into regions that are 5-7 mm thick (Figure 6.2b). After that, each region is represented with a single center-point defining the trajectory of drilling path (Figure 6.2c). Note that the points on the drilling trajectory would need to be

reached by the injection equipment (i.e. flexible needle). We define an injection blob between each of the trajectory points and apply a gradient descent algorithm to optimize the rate of injection between these points (Eq. 6.1). Optimization was initiated assuming a constant rate of injection throughout the injection trajectory (Figure 6.2d). The optimization is constrained so that the total volume of injection blobs is less than 10 ml (Eq. 6.1).

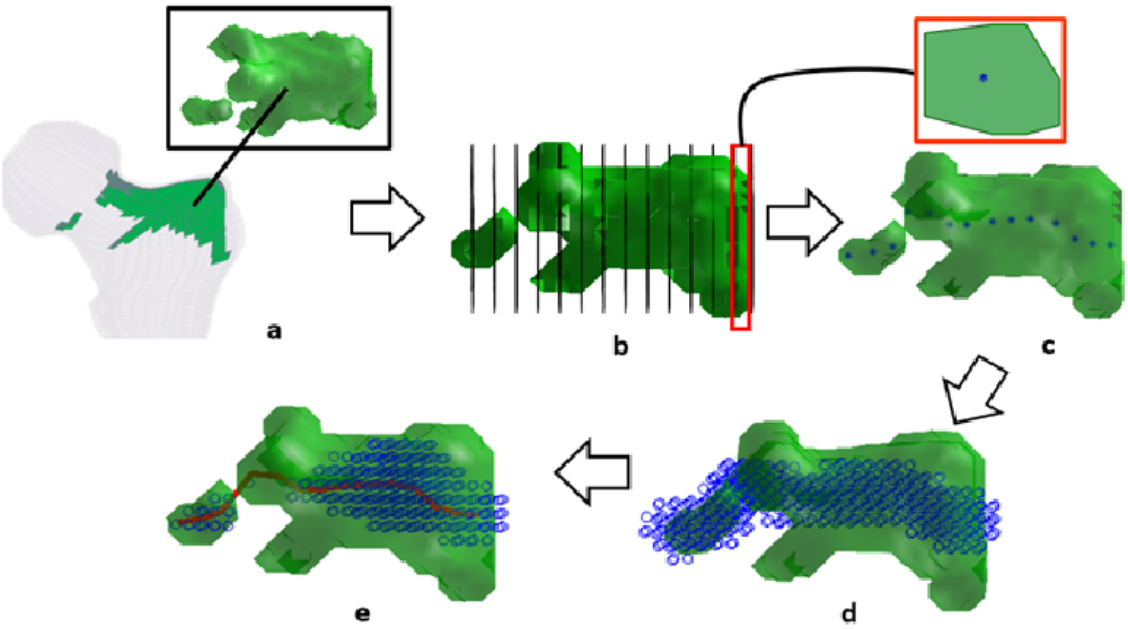

Figure 6.2: Overview of the optimization algorithm: Creating an isosurface of the cement elements from BESO (a), Dividing the cement volume into regions (b), finding the center points (c), initiating the optimization algorithm to find injection rates (d), and final drill trajectory and injection volume (e).

$$Min \ \frac{V_{BESO} \bigcup V_{Injection}}{V_{BESO} \bigcap V_{Injection}} \quad Subject\ to: \quad V_{Injection} < 10ml \tag{6.1}$$

Next, we can calculate the rate of injection distribution between the two

trajectory points:

$$i_n = \frac{V_n}{L_n} \tag{6.2}$$

Where i_n, V_n, and L_n represent the injection distribution (in ml / mm), volume of injection (in ml), and length of the injection blob (in mm) respectively.

6.2.2 Data Analysis and Validation

Planning was repeated for all 4 samples to find the best match between BESO and curved pattern of injection. To evaluate the injection outcome, we used the Smoothed Particle Hydrodynamics (SPH) method as described in chapter 3 (and also in [52]). SPH creates a porous model of the bone from CT scans and incorporates the extreme viscosities associated with the bone cement. We assumed injection rate of 0.1 ml / s for bone cement and modified the needle retraction rate to achieve the desired injection distribution (i_n) for each blob. In addition, we assumed the viscosity of 150 Pa.s for PMMA at the time of injection. Finally, we created a post-operative FE model of the bone from the SPH results to estimate the yield load. PMMA elements were assigned constant material properties with elastic modulus of 1.2 GPa and Poisson's ratio of 0.4. Assuming inhomogeneous material properties for the bone, a static FE analysis was performed on each model using ABAQUS (ABAQUS/Standard V6.8, SIMULIA, Providence, RI). We compared the results for yield load for

each specimen with its non-augmented state using a two-way ANOVA test with state significant level of 0.05.

6.3 Results and Discussion

It was determined from planning paradigm that only 7.2 ml of cement is required for augmentation on average. Consequently, FE analysis showed that curved injections results in an increase of 69% for the yield load. This is significantly lower than the volumes used in previous studies [12, 16, 44, 56]. Figure 6.3 shows the average yield load of the bone for the non-augmented (control) and augmented state of the bone. In study of Basafa et al. [15], yield load was increased by 33% with average injection of 9.5 ml . Moreover, in generalized injections proposed by Varga et al. [13], yield load was increased by 64% with approximately 12 ml of bone cement. Therefore, Curved drilling has allowed to reduce the average injection volume as compared to straight line injections. The biomechanical benefits of the injection (yield load) was found to be significant ($P < 0.01$) and comparable with those of the previous studies where higher volume of PMMA were injected along a straight path. Figure 6.4 shows the optimization convergence for the first two samples where objective function (Eq. 6.1) is calculated in each iteration. The algorithm converged within 30 iterations for all samples with an average objection value of 2.81 for the final

iteration.

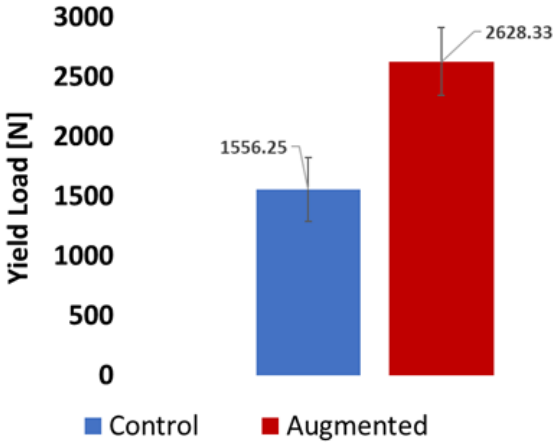

Figure 6.3: Bone yield load before and after injection.

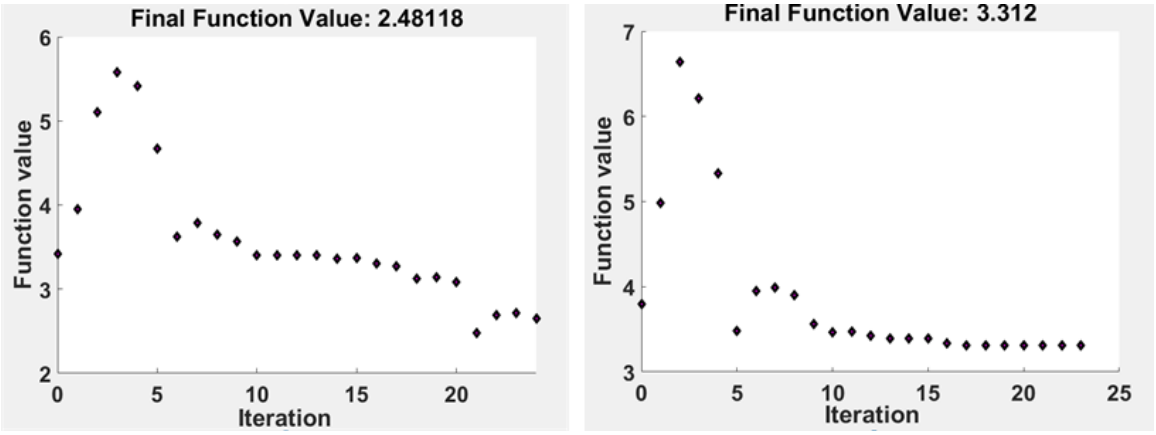

Figure 6.4: Results of the optimization convergence for sample 1 (left) and 2 (right).

In the proposed planning paradigm, thickness of the injection pattern changes throughout the needle path. The sudden significant increase in the thickness of the cement blob may increase the potential risk of cement leakage outside the desired path. However, SPH results showed no significant of cement leakage for the samples used in this study. Figure 6.5 shows the results of SPH for cement diffusion of sample 3. Although we have introduced a new approach for

cement injection, the feasibility of this approach remains to be verified via direct experiments where flexible tools are used for drilling and injection of bone cement. The results presented in this study assumed an ideal execution of the plan. Also, we have only considered the yield load to evaluate the biomechanical outcome of the injection. Including other biomechanical properties (i.e. yield energy) would be advantages to verify the superiority of the augmented bones.

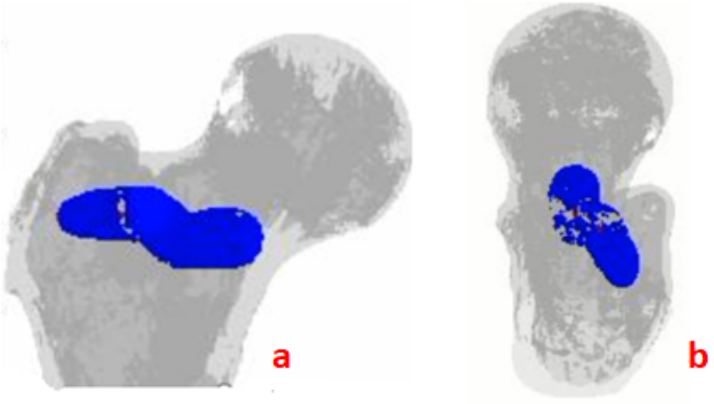

Figure 6.5: Sagittal (a) and axial (b) of SPH Results after cement injection for sample 3.

In the recent study of Alambeigi et al. [79], a novel cable-driven Continuum Dexterous Manipulator (CDM) was combined with flexible cutting tools to achieve curved-drilling. This technique was initially introduced for core decompression of osteonecrosis. The high dexterity of CDM can result in significant improvements for implementation of femoroplasty as compare to the rigid tools. Alambeigi's study showed that the dominant parameter in controlling the drill trajectory are the cable tension applied to the CDM and the

cutting feed rate [79]. Figure 6.6 shows an X-ray view of the flexible drill inside the femur. As shown by the results shown above, a major advantage of using curve-drilling in femoroplasty is reaching all regions that would benefit from cementation including some of which that are not possible with the rigid tools.

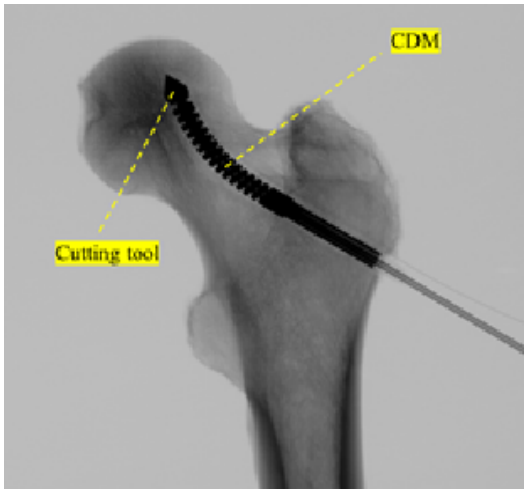

Figure 6.6: Curved-drilling of the proximal femur using a cable-driven CDM

6.4 Conclusion

This chapter presented a new planning paradigm for osteoporotic bone augmentation based on injection patterns that are achieved with curved-drilling. Through preliminary simulations, it was shown that using curved patterns for cementation can be highly advantageous and results in reduced volume of cement injection. This algorithm can be extended to other bone reinforcement applications to reduce the risk of thermal necrosis. Future works involves experimental validation of the algorithm in cadavers where invasive mechanical

testing is performed to evaluate the biomechanical outcome.

6.5 Recapitulation of Contributions

The author's contributions in this chapter are as follows:

- Implementing a new optimization algorithm for femoroplasty using curved paths for the injection profile.
- Performing simulation experiments to validate the algorithm's efficiency through FE and hydrodynamics analysis.

Chapter 7

Large Deflection Shape Sensing

7.1 Introduction

Flexible instruments and Continuum Dexterous Manipulators (CDMs) are commonly used in minimally-invasive surgery (MIS) due to their superior steerability and large operating space. Several groups have proposed a variety of surgical dexterous manipulators. Examples include active cannulae composed from a series of nested and curved tubes [82, 83], shape memory actuation units [84], and cable-driven manipulators such as one discussed in Section 6.3 [85–87].

Previous efforts in Biomechanical and Image-guided Surgical Systems (BIGSS) laboratory has led to development a cable-driven 2D CDM. This highly dexterous CDM was initially designed for MIS treatment of Osteolysis occurring

after total hip arthroplasties [88]. The goal of this procedure is to remove and replace the bone defect caused by polyethylene liner of an acetabular implant. Without removing the well-fixed acetabular implant, the MIS approach uses the holes in the implant to access the osteolytic lesion (Figure 7.1). This cable driven CDM with a 6 mm outer diameter was built from two nested nitinol tubes. The major features of this CDM for orthopedics applications include relatively large inner to outer diameter ratio (4mm / 6mm) and relative structural strength in the plane orthogonal to its bending plane. These features enable inserting custom-designed tools (e.g. flexible cutter, gripper, curette, flexible endoscope) through the lumen of the CDM for the proposed procedure as well as other similar MIS applications.

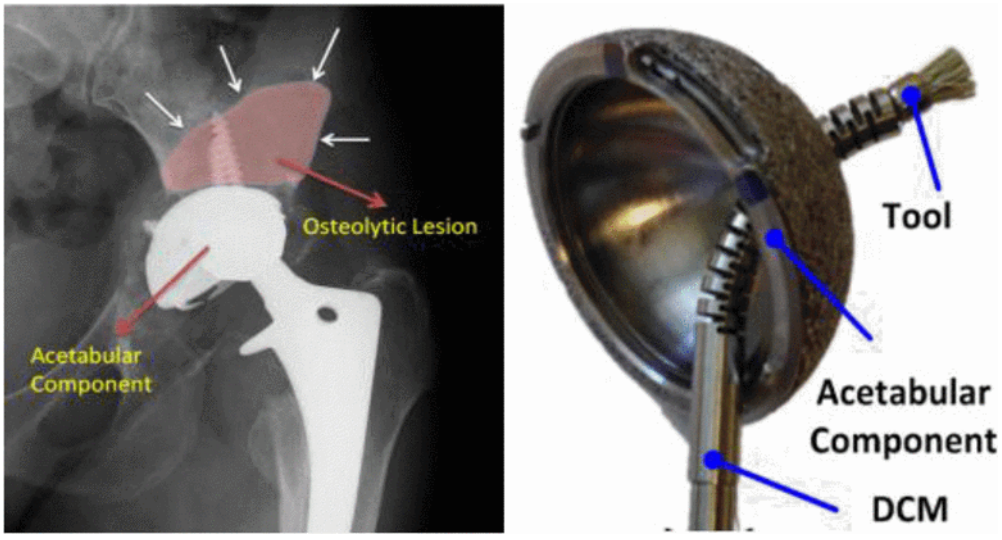

Figure 7.1: The (a) osteolysis and (b) CDM with a tool through screw hole on acetabular cup.

Previous efforts for intraoperative control of the CDM involved developing models for estimating the shape from cable-length measurements [89, 90], as well as the intermittent use of x-ray for updating the model estimation [91]. This approach would, however, require a trade-off between accurate real-time control and the amount of x-ray exposure to the patient. Real-time shape sensing would reduce the reliance on using intermittent x-rays for estimating the shape of the CDM.

Approaches for shape sensing may include the use of electromagnetic sensors. In the presence of metal implants and tools, however, electromagnetic interference will limit the accuracy of the sensors [92]. Also, these sensors usually have a rigid body and cannot adapt to the continuous bending of the instruments or robots, especially for a small continuum robot [90]. In addition, the tracking frequency is limited to less than 50Hz. Other competitive approaches for large deflection shape sensing include piezoelectric [93] and piezoresistive polymers [94]. However, their size, the stress-strain hysteresis of the piezoresistive polymer and the bias and drifting problem of PVDF are limitations that are difficult to overcome.

Fiber-optic sensors offer a number of advantages over conventional sensors, including the absence of electromagnetic interference, lightweight structures, stability, repeatability, high sensitivity, fast response, integrated structure, and a potentially low cost. Owing to their intrinsic characteristics, FBGs are par-

ticularly well suited for measuring strain with a high bending sensitivity. By analyzing the reflected wavelength from each fiber, the curvature and bending direction can be obtained.

Two different approaches are commonly used for curvature detection with FBG sensors: 1) integrating the sensor with a substrate to form an assembly (e.g. [95,96]), and 2) creating a bundle of sensors and optical fibers (e.g. [97,98]).

For both approaches, maximizing detection range has rarely been considered in the literature. For the osteolysis surgery or curved cementation discussed in Chapter 6, the largest bending radius can reach to approximately 6 mm, where the curvature is 166.7 m^{-1}. This value is much larger than what current methods of shape sensing can measure. To detect relatively large curvatures, it is not possible to directly connect the FBG sensor to the CDM (i.e. approach 1), because the bending strains of the CDM are much higher than what optical fibers can handle. Therefore, a special supporting structure may be required to reduce the bending strain of the optical fiber for large curvature bending. By using Multi-core fibers, eccentric-core fibers, and D-shape fibers (approach 2), we can reduce the bending strain to a fairly small value. This, however, may cause light interference for the multi-core fiber or reduce the stiffness of the D-shape sensor. It is also challenging to keep sensors bending in a specific direction.

This Chapter focuses on design a novel large curvature detecting Shape

Sensor Array (SSA) for the aforementioned CDM. Section 7.2 describes the conceptual design, SSA modeling, assembly and preliminary calibration results and an algorithm for getting the 2D shape of the CDM. The experiments and evaluation of the shape sensing performance is described in Section 7.3.

7.2 Shape Sensing Approach

7.2.1 Design Concept

Generally, the shape of the sensor is obtained from interpolation of discrete FBG strain data along the arc length. Because of this, the configuration of the FBG sensor should be properly designed to meet requirements of large curvature detection for our CDM. The basic principle of curvature detection is as follows [92–101]:

$$\Delta\lambda = k_\epsilon \epsilon + k_T \Delta T \tag{7.1}$$

$$\epsilon = \delta \times \rho \tag{7.2}$$

where ϵ is the strain for FBG sensor, δ is the bias distance of the optical fiber from the neutral plane of the sensor (Figure 7.2), k is the curvature of the body being tested, $\Delta\lambda$ is the wavelength shift, k is the strain coefficient, and k_T is the temperature coefficient.

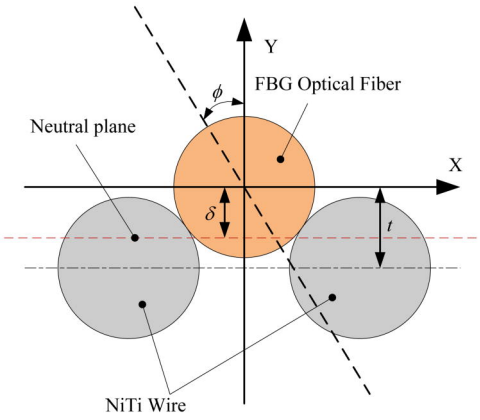

Figure 7.2: Sensor configuration for larger curvature detection.

If temperature is well compensated, the wavelength shift of FBG optical fiber is proportional to the strain as well as the curvature. Therefore, the maximum curvature is largely dependent on δ which should be kept as small as possible. In contrast to making the core biased or cladding asymmetrical within the optical fibers, our sensor is designed with one FBG optical fiber and two nitinol wires that are bonded together, as shown in Figure 7.2. The distance between the FBG core and the line connecting two nitinol wire centers is t and ϕ represents a certain bending direction which will be used later for evaluating the bending modulus.

The dimensional requirements are as follows:

- The FBG allowable strain requires the FBG fibers to be located near the neutral plane of the SSA. FBG fibers should work within certain strain range. Previously it was shown that optical fibers can handle strain values that are less than 0.5% [98]. In our study, we have used FBG fibers

that can measure up to 1% strain without breaking;

- In order to distinguish wavelengths for all FBG sensing points, the wavelength ranges must ideally have no overlap. The wave length range for the used interrogator was 40nm (Micron Optics, USA). However, some overlap will enable employing more FBG sensing points within the wavelength range and, therefore, provide higher shape sensing precision.

The nitinol wires prevent local stress concentration. Different materials can be used for this application, but considering the allowable strain under large deformation, nitinol is the most suitable choice for this application. As a result of its superelasticity property, nitinol works in its elastic region (with constant modulus) within the allowable strain range of the optical fiber.

The FBG center line to the SSA neutral plane distance can be adjusted to a small value by changing the relative distance of two nitinol wires, as shown in Figure 7.3. The triangular cross section of the SSA (shown in Figure 7.2) has a non-uniform elastic bending modulus which keeps the SSA from twisting.

7.2.2 Shape Sensing Scheme

The CDM in this paper can bend in a plane, called bending plane. The CDM's bending modulus in this plane is much smaller than that of other planes. Therefore, 2D shape sensing is sufficient to track the position of the CDM. Fig-

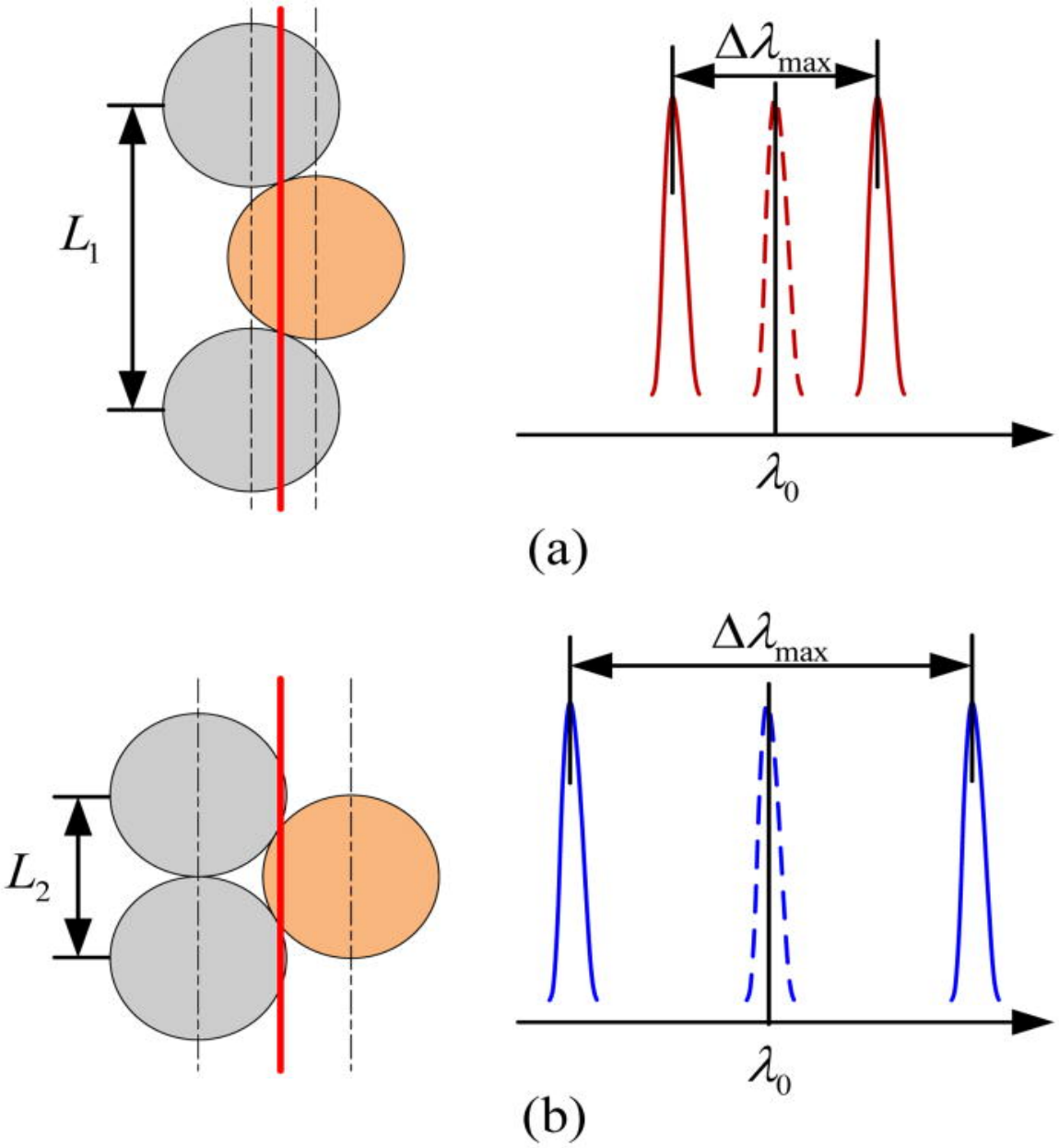

Figure 7.3: Strategy to reduce the range of wavelength shift by increasing the center distance between nitinol wires (L1 > L2) a) reduced wavelength shift and b) larger wavelength shift.

ure 7.4 shows the overall design, in which two SSAs are inserted through the channels within the CDM wall. At the distal end of the CDM, the SSAs are attached to the CDM body keeping their neutral planes perpendicular to the CDM bending plane. In our proposed design, the SSAs are allowed to freely move parallel to the CDM bending plane. At the proximal end, there is a sliding support with tiny triangular holes in it, through which the SSA will be inserted.

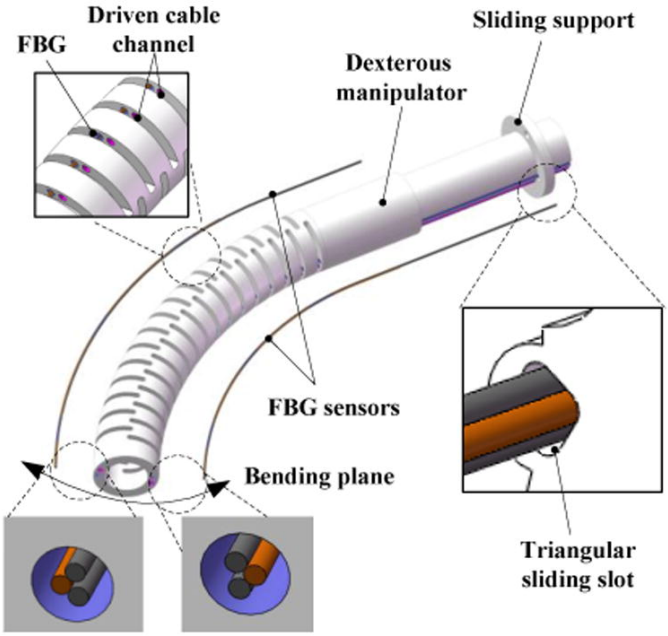

Figure 7.4: Shape sensing for osteolysis dexterous manipulator.

The design features of the CDM sensors are shown in Fig. 4 and described in the following:

- The CDM has an inner lumen for the surgical instruments, such as a cutter, or a brush to get through. Sensors cannot occupy this lumen since

they may interfere with those instruments. Also, we cannot place the sensors on the outer surface of the CDM since that increases its overall size. Therefore the sensor is inserted in the channels through the wall of the CDM.

- The SSA can freely move along the CDM. A single sensor on one side of the CDM is either in tension or compression. This will result in a biased length for the sensor. By using two SSAs in opposite sides, we can compensate for the changes in lengths due to tension and compression effects.

- The twisting of the SSA will affect the results of shape sensing to a great extent [102]. Since the SSAs are flexible, they can easily twist as the CDM bends. To prevent torsion, a sliding support was added to the proximal end of the CDM. This, together with the non-uniform bending modulus of the SSA will prevent the sensor from twisting.

- The CDM is a segmented structure. The nitinol fibers allow the SSA to maintain a continuous curvature through the CDM channels in order to prevent the FBG fiber from breaking.

7.2.3 Modeling

To develop a theoretical model for the SSA, it is necessary to find its neutral plane (Figure 7.2). We assume the SSA is a composite beam with a different material at each section. The neutral plane can be obtained from the equilibrium equation of forces:

$$\int_{A_1} \sigma_1 dA_1 + 2\int_{A_2} \sigma_2 dA_2 = F_N = 0 \tag{7.3}$$

$$\sigma_i = E_i(y - \delta)/\rho \tag{7.4}$$

where σ_i, A_i and E_i (i = 1,2) are the stress, cross sectional area and Young's modulus for optical fiber and nitinol wire (Figure 7.2), therefore the location of neutral plane is:

$$\delta = \frac{2E_2{D_2}^2 t}{E_1{D_1}^2 + 2E_2{D_2}^2} \tag{7.5}$$

where

$$t \in [\frac{d_{core}}{2}, \frac{\sqrt{(D_1 + D_2)^2 - {D_2}^2}}{2}] \tag{7.6}$$

d_{core} is the radius of the optical fiber core and D_i (i = 1,2) are the outer diameter of optical fiber and nitinol wire.

7.2.4 Shape Sensor Assembly

The optical fiber used in this study contains an array of 3 FBG sensors distributed 10 mm apart. The length of the active area for each sensor is 3 mm (Technica SA, China). LOCTITE 3101. A modified acrylate UV glue (Henkel, Germany) was used to glue two nitinol wires with oxide surface (NDC Technologies, USA) to the FBG optical fiber. An assembly device was designed to precisely maintain the relative position between the optical fiber and these wires. Figure 7.5 shows the SSA assembly under microscope (ZEISS, Germany) at 25 times magnification. After the assembly, the SSA was placed inside the CDM wall channels. The optical fiber was fixed at the distal end, and a triangular slot (shown in Figure 7.4) was manufactured by laser cutting (Laserage Technology Corporation, USA) to maintain its orientation at the proximal end.

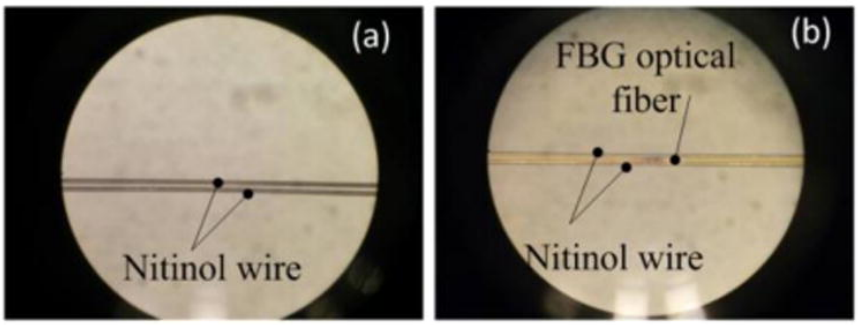

Figure 7.5: The (a) Parallel nitinol wires and (b) whole assembly under microscope.

7.2.5 Sensor Calibration

To validate the linearity of the curvature-wavelength relationship, a multi-channel calibration board with different curvatures was designed and 3D printed (Figure 7.6). For this experiment, two clamps with triangular slots were fabricated to preserve the orientation of the SSA on both sides. Figure 7.7 illustrates the results of calibration for all 3 sensors within the SSA. The slopes of the fitting lines are slightly different. This may be due to the precision of the assembly or the use of a varying amount of glue. Fig. 7 shows the calibration results for 3 FBG sensors.

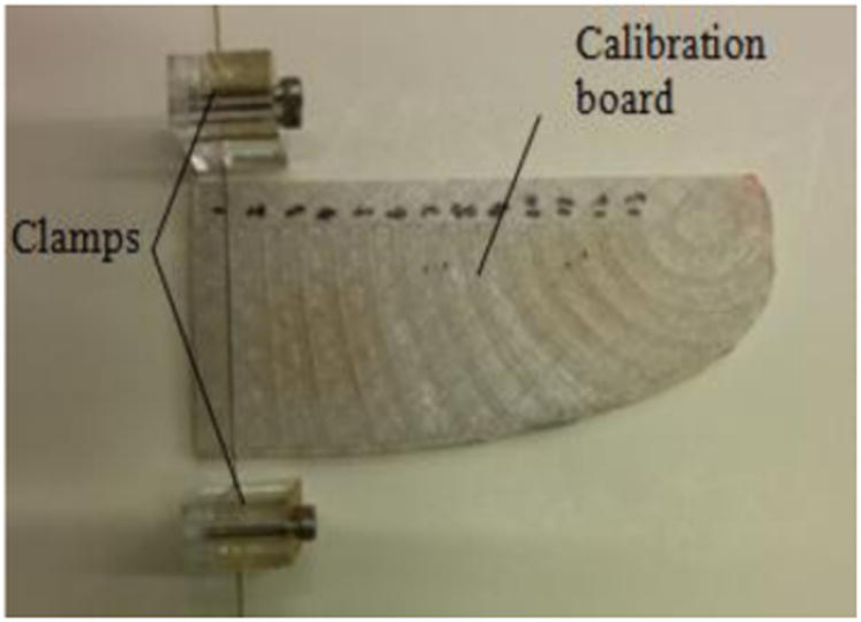

Figure 7.6: Calibration board for 2D Shape Sensor Array.

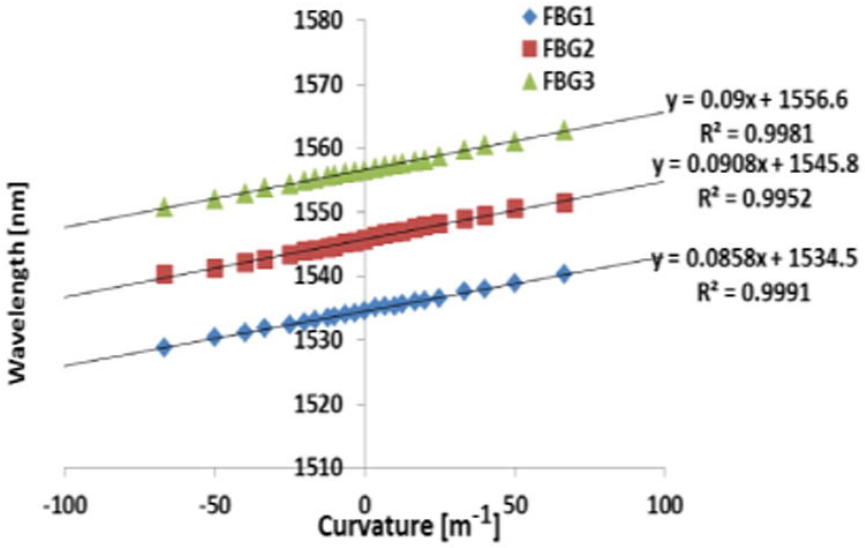

Figure 7.7: Calibration board for 2D Shape Sensor Array.

The relationship between curvature and wavelength shift are shown below:

$$\Delta\lambda_1 = 0.091 \times k_1 + 1556$$

$$\Delta\lambda_2 = 0.103 \times k_2 + 1545$$

$$\Delta\lambda_3 = 0.093 \times k_3 + 1533$$

7.2.6 2D Shape Reconstruction

The wavelength range for each FBG sensor, and the number of FBG sensors that we can use are limited due to the wavelength range of the interrogator. In this case, within the 40 nm wavelength range of the interrogator, 3 FBG sensors were placed along the optical fiber. For the 2D shape reconstruction, a linear relationship was assumed between curvature and the arc length so linear interpolation is done for two segments connecting these three FBG sensors.

Usually, the coordinate system is built at one end of the shape sensor and the tangential direction at the end is set to be and the Y axis.

The tangential angle with respect to X axis, θ is calculated from the integral of curvature and the coordinates can be calculated numerically using the equations below:

$$\theta(s) = \int_0^s k(s)ds + \theta_0 \tag{7.7}$$

$$\begin{cases} \Delta x = cos\theta(s) \cdot \Delta s \\ \Delta y = sin\theta(s) \cdot \Delta s \end{cases} \tag{7.8}$$

where θ_0 is the tangential angle at the starting point, s is arc length and Δx and Δy are the increments for an arc length infinitesimal Δs.

7.2.7 Shape Sensing Scheme of CDM

Figure 7.8 shows the arrangement of the FBG sensors (yellow dots) on SSA along the CDM. There are two segments without sensor covered. The curvatures are assumed to be constant. When the CDM bends, the arc length for the side where SSA 1 is located increases and the 3 FBG sensors cannot cover the whole length of the CDM. On the other hand, the arc length for the side where SSA 2 is located decreases and its 3 FBG sensors can cover the arc length.

When the CDM bends towards the opposite side, the opposite is true about these sensors. Therefore, the two SSAs are highly complementary and by using the combination of their shape in their coordinate system $\Sigma 1$ and $\Sigma 2$, we can construct the 2D shape for the CDM's centerline.

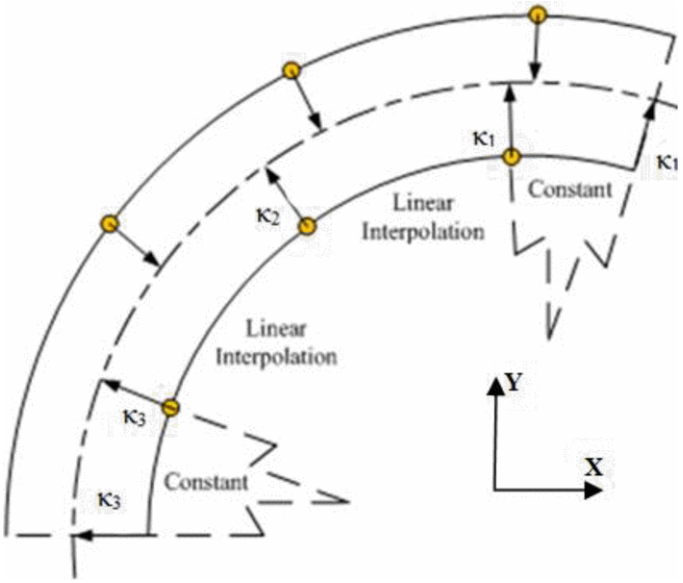

Figure 7.8: Arrangement of the FBG sensors for Shape reconstruction.

7.2.8 Sensor Calibration inside the CDM

For reconstructing the shape of the CDM in real-time, we first found the wavelength-curvature relationship for SSA inside the channels within the walls of the CDM. For this purpose, we designed and manufactured a calibration board that contained 5 slots with different curvatures, ranging from 15.6 m^{-1} to 50.8 m^{-1}. These slots were built according to the dimensions of the CDM (6 mm outer diameter and 35 mm length) such that it could fix the position of the

CDM within a constant curvature. The CDM was manually placed in the slots and wavelength data were recorded for all of the FBG sensors. This process was repeated 10 times for each slot. Figure 7.9 shows the constant curvature bending of the CDM inside the slot. Since the curvature was constant, the wavelength shifts for all of the FBG sensors within SSA were expected to be the same.

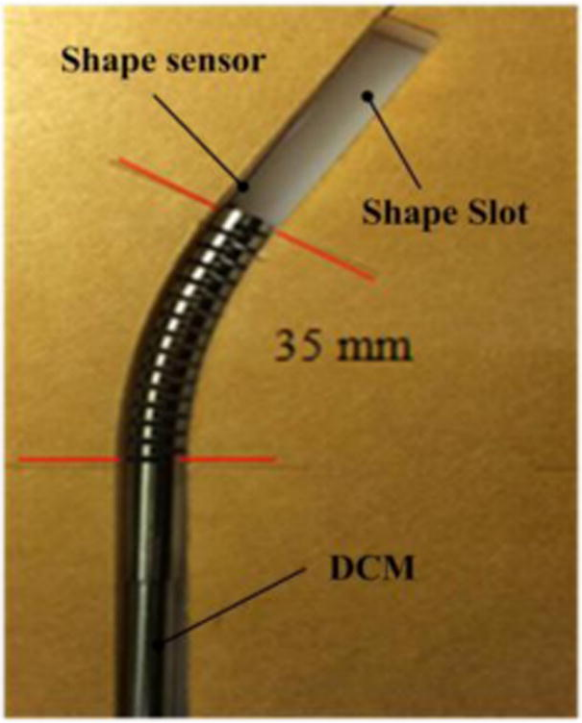

Figure 7.9: Shape sensing with constant curvature bending.

7.2.9 Results and Error Analysis

For a preliminary verification of our proposed method, we generated the calibration curve from wavelength data obtained from four of the slots at each

time. The wavelength data from the fifth slot was then used for predicting the curvature of that slot (leave-one-out experiments). The leave-one-out verification experiments were performed for the three middle slots. The mean error was found to be 7.14% for the 16.7 m^{-1} curvature, 1.02% for 23.5 m^{-1} curvature, and 1.25% for 30.1 m^{-1} curvature. Figure 7.10 shows the mean wavelength shift of the FBG sensors for different curvatures. In this case, the verification was done for the slot with a 23.5 m^{-1} curvature.

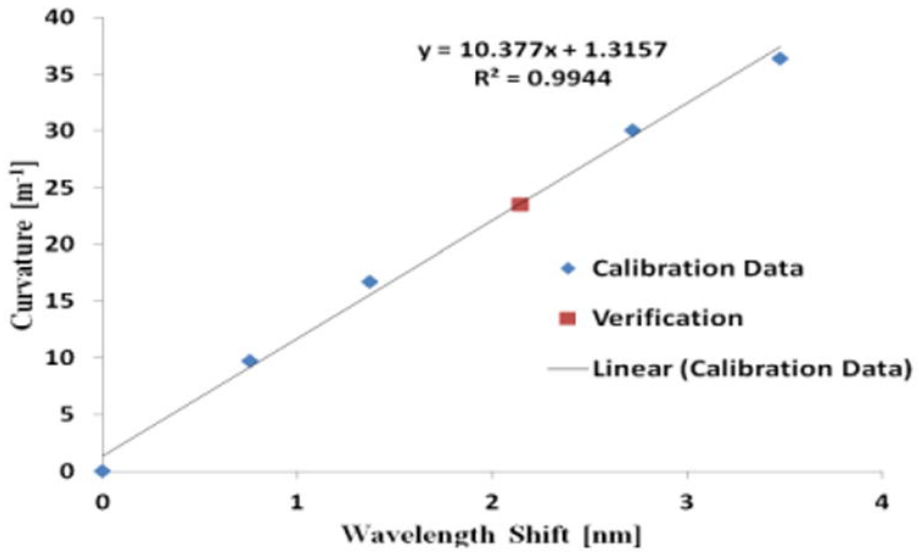

Figure 7.10: Wavelength shift for different curvatures, calibration (blue) and verification (red).

7.3 Dynamic Shape Tracking

7.3.1 Experimental Platform

Experiments evaluated the accuracy of the shape tracking during the manipulator's motion. Figure 7.11 shows the experimental platform, which included a custom actuation unit, FBG interrogator (Micron Optics, USA), and PL-B741 camera (PixelLink, USA). Three types of experiments were performed: 1) free bending (i.e., no external loads applied to the CDM), 2) bending in the presence of an obstacle, and 3) bending in the presence of a tool inside the inner-lumen. The FBG interrogator recorded the wavelengths of each FBG sensor during the experiment and also the estimated tip position based on these wavelengths. The calibrated overhead camera captured planar images of the CDM at 0.5 mm increments of cable displacement to analyze and compare to the shape sensor data as a ground truth. The CDM actuation unit used a 3 mm diameter, 1 mm lead ball screw assembly (Steinmeyer, Germany) to actuate both drive-cables during each bending cycle [103]. Custom C++ software controlled the CDM and collected synchronized data from the shape sensors and the camera.

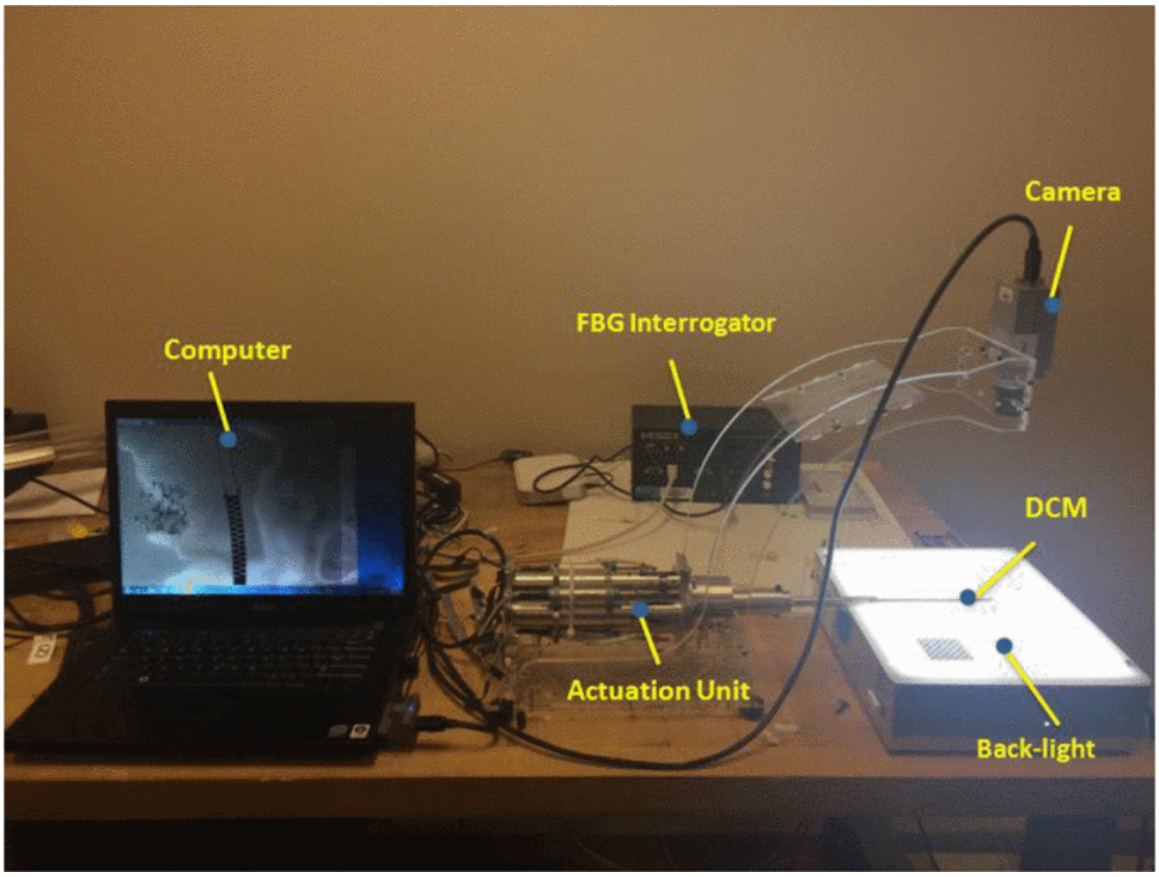

Figure 7.11: Overall view of the experimental setup.

7.3.2 Case I: Free Bending

A total of 3 free bending experiments with variable cable displacement rates (0.5 mm / s, 0.75 mm / s, and 1 mm / s) were performed. With these rates, the CDM can bend to the maximum cable displacement of 3 mm in 6, 4, and 3 seconds, respectively. Prior to each experiment, a manual calibration procedure defined the zero cable position. Zero position is the point where the cable is in tension and if a small delta is applied to the cable position, the CDM starts to bend [103]. In each experiment, the CDM was actuated for 5 bending cycles.

Each cycle included free-bends to 3 mm cable displacement and return to the zero position on both bending directions. Although this manipulator is capable of larger bends, this threshold was set to avoid potential damage to the shape sensors. Figure 7.12 shows the CDM configuration during a free bending test captured by the camera.

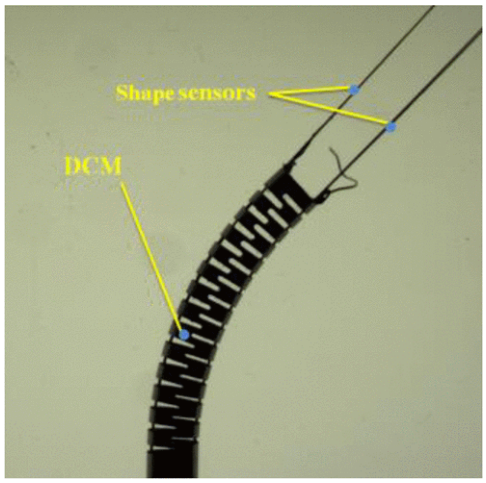

Figure 7.12: Free bending configuration of the CDM at 2 mm cable displacement.

7.3.3 Case II: Bending with an Obstacle

Two bending experiments were carried out at 0.5 mm / s and 1.0 mm / s cable displacement rates. Similar to the free bending case, CDM actuated for 5 cycles, starting and ending at the zero position. In this case, however, maximum cable displacement was set to 2 mm. To create an obstructed environment for the CDM, a rigid path obstacle with diameter of 25 mm was fixed on one side. Figure 7.13 shows the CDM configuration during its contact with the obstacle.

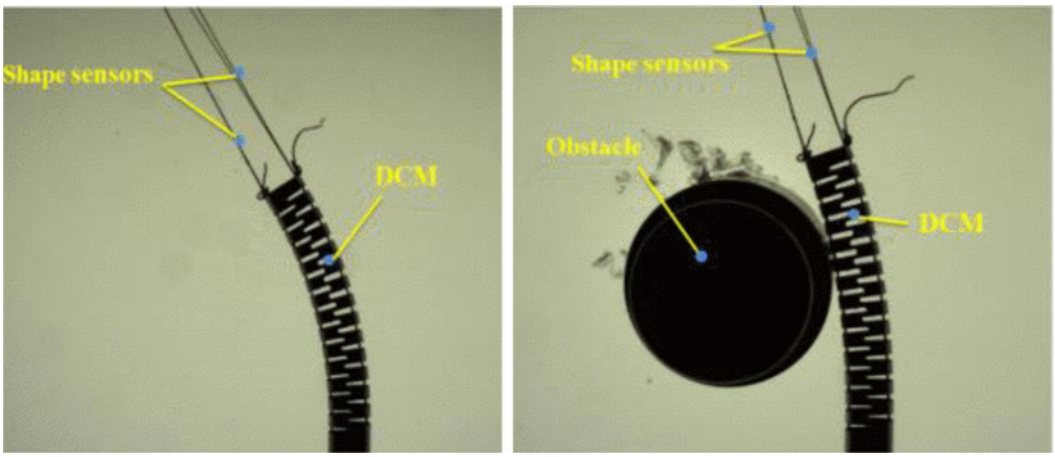

Figure 7.13: CDM bending configurations at 2.0 mm cable displacement in free bending (left), and bending in the presence of an obstacle.

7.3.4 Case III: Bending with a Tool

A recent surgical tool developed for osteolysis treatment utilizes a flexible torque coil [104]. In this experiment, a torque coil (Asahi Int. USA, Inc.) with a 3.3 mm outer diameter was inserted in the lumen of the CDM to evaluate FBG-based shape sensing similar to the experiment for case I (Figure 7.14). Each experiment ran for 5 cycles with the cable displacement rate at 0.5 mm / s and maximum cable displacement of 2 mm.

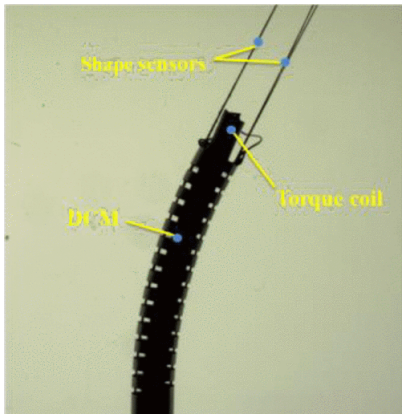

Figure 7.14: CDM bending configuration in a presence or a torque coil inside its lumen.

7.3.5 Data Analysis

Prior to data collection, camera calibration using a square chessboard identified the intrinsic parameters. A previously validated 2D-3D registration algorithm developed by Otake et al. [105] processed each image to provide a ground truth CDM shape. This method outputs the shape curve associated with the CDM's centerline, given a planar image of the CDM. The method optimizes a normalized gradient information similarity metric between a reconstructed 2D image and the raw camera data. Registration results served as the ground truth to evaluate the tracking accuracy of the sensors. For this purpose, the timestamp of each camera image is used to associate each ground truth measurement with the appropriate FBG data. Linear interpolation of the FBG measurements is performed when an image timestamp lies between two FBG measurements. We compared the ground truth coordinates with the corresponding values measured by the shape sensors to measure error. ANOVA analysis of variance was performed to compare different experimental groups.

7.4 Results

The average and standard deviation of the tip tracking errors of all experimental cases are shown in Table 7.1. In the free-bending case with a 0.5 mm / s cable displacement rate, mean error was 1.14$\pm$0.77 mm. This value increased

to 3.49±1.3 mm when the cable displacement rate changed from 0.5 mm/s to 1.0 mm/s. These values correspond to 3.25% and 9.9% of the CDM's length, respectively. In the case of bending with an obstacle, the average error was 2.77±0.77mm which is 7.8% of the CDM's length. In the case of bending with a tool, the average error was 0.93±0.59mm or 2.6% of the CDM's length. ANOVA analysis of variance shows that free bending accuracy is significantly different with those of bending with an obstacle ($p > 0.99$). However, these is no significant difference ($p = 0.96$) between the shape sensing accuracy with and without a tool.

Table 7.1: Summary of tip tracking results for all experimental groups.

Case	Free Bending			Bending with an Obstacle		Bending with a tool
Cable displacement [mm/s]	0.5	0.75	1.0	0.5	1.0	0.5
Max cable displacement [mm]	3.0	3.0	3.0	2.0	2.0	2.0
number of images per cycle	24	24	24	16	16	16
Mean trajectory error [mm]	1.14	0.81	3.49	2.73	0.96	0.93
SD of error [mm]	0.77	0.99	1.30	0.77	0.35	0.59

Using the extracted coordinates of the tip position from the images and sensor data, planar trajectories of the tip position were plotted for 3 cases of free bending, bending with an obstacle, and bending with a tool (Figure 7.15).

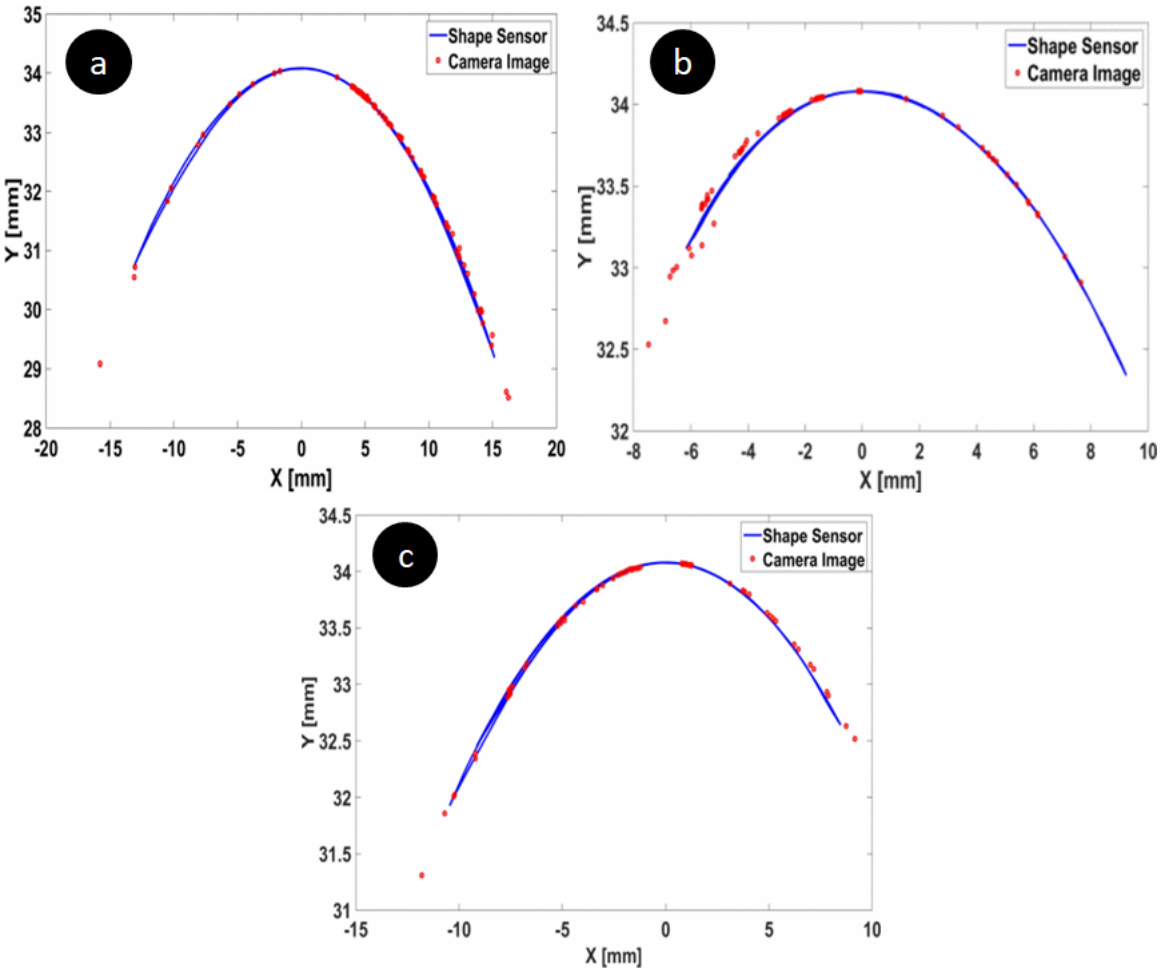

Figure 7.15: This figure shows (a) Comparison of shape sensing trajectory with the trajectory extracted from images in free bending, (b) bending with an obstacle (Figure 7.13), and (c) bending with a tool.

To find the exact sources of error, we have considered a free bending experiment with the cable displacement rate of 0.75 mm / s and examined the tip position on the x-axis and y-axis separately 7.16. In this case, tip tracking had an error of 0.76$\pm$0.92 mm in the x-direction and a mean error of 0.25$\pm$0.36 mm in the y-direction.

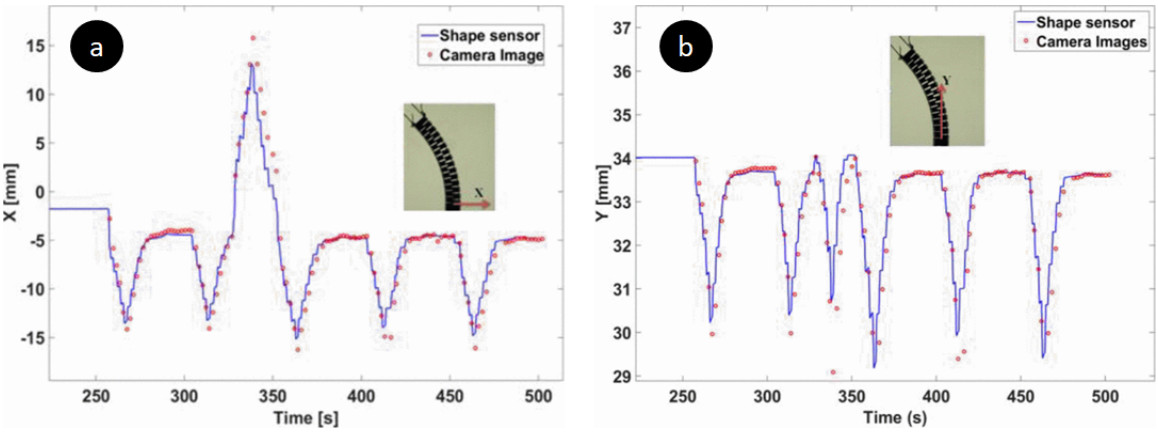

Figure 7.16: Tip position on the x-axis (a) and y-axis (b)-free bending case at 0.75 mm/s cable displacement rate.

7.5 Discussion

This chapter demonstrates the feasibility of large deflection shape tracking for a 35mm length CDM using two shape sensors. For this purpose, we used FBG fibers along with nitinol wires as the supporting substrate to form a triangular cross section. The neutral plane of the SSA assembly was adjusted to reduce the wavelength shift of the FBG sensors. In addition, the bending modulus was kept non-uniform causing the SSA bend in the same direction as the CDM. The calibration curves in Section 7.2.9 showed a fairly linear curvature-wavelength relationship for SSA sensors.

Furthermore, we considered dynamic case when the CDM is undergoing continuous bends. It showed, through 120 captured images during the free bending test (rate = 0.75 mm / s), that if the CDM is moving, the average error increases to 2.31% of the CDM's length. In each of the bending cycles, the

maximum error occurred at the maximum cable displacement. Due to a higher range of motion in the direction of x-axis (Figure 7.8), tip tracking experienced a larger error in this direction, compared to errors of the y-axis. Considering the immediate application of this CDM for osteolysis treatment, the 2.31% error will not jeopardize the safety since there are no critical tissues or organs in the operating space of the CDM. We have also seen that if the CDM bends twice as fast (1 mm / s), the error increases to about 10% of the CDM's length. Therefore, it is important to identify obstacles and if we want to consider the feedback from FBG sensors in the control loop. We do not, however, foresee a requirement for fast motion of CDM when debriding osteolytic defects behind the acetabular implant.

One of the main characteristics of the operating space in treatment of osteolysis is the presence of obstacles. Therefore, it is important to evaluate shape sensing capabilities of the FBG-sensors in those environments. When the CDM is in contact with an obstacle (Figure 7.13), it begins to deform and the linear interpolation of the curvature between sensing nodes may not be accurate. For this reason, the increased error of 7.8% of the CDM's length was expected. One way to avoid this error is to increase the number of sensing nodes on each sensor. However, given the limited range of the interrogator, adding more sensing nodes is challenging. Further studies are required to evaluate shape sensing with an increased number of sensing nodes, as well as the optimization algo-

rithms to find the optimum location of the FBG sensing nodes along the CDM. To avoid potential damages to the CDM and FBG-sensors maximum cable displacement was reduced to 2 mm in these experiments.

A major advantage of the osteolysis CDM is the 6 mm inner-lumen. In the treatment procedure, surgeons can use the CDM to introduce flexible tools to the operating area. The tools, however, may alter the trajectory of the CDM by changing the system stiffness [106]. To address the issue, shape sensing accuracy was evaluated when a torque coil was inserted inside the CDM lumen. Results indicate that there is no significant difference (P = 0.96) between the shape sensing accuracy with and without a tool. Due to increased stiffness of the CDM in the presence of a tool, these experiments were also conducted with maximum cable displacement of 2 mm.

For these experiments,the 2D/3D registration algorithm of Otake et al. [105] was as the ground truth. However, the mean error of 0.4 mm associated with this technique may affect the analysis. In addition, lower frequency of images compare to FBG data collection may introduce an error while considering the experimental cases with faster cable displacement rate. Although all experiments were performed at the room temperature, small temperature changes may introduce an error in our calculations. In addition, accuracy of the shape sensors is dependent on the reference wavelengths which are defined as the wavelengths of the sensors at zero position. Potential changes to the CDM

configuration during the initialization, is another source of error for these experiments.

7.6 Conclusion

This chapter introduced a novel shape sensing technique and evaluated its capability in a 35 mm length CDM in 3 dynamic cases. Results have shown that FBG sensors can track the tip position with an average error of 0.81 mm. It was also shown that there's no significant difference between the accuracy of free bending with those of bending with a tool (P = 0.96). However, we have observed a significant increase of mean error in the presence of an obstacle (P $>$ 0.99).

It is important to note the developments presented in this chapter were part of early efforts for real-time tracking of the CDM. After these efforts and motivated by less-invasive treatment of pelvic osteolysis during total hip revision surgery, Sefati et al. [107] proposed a new design for the sensing unit that eliminates fabrication challenges by embedding the FBG array and NiTi wires inside the tube in a more robust, repeatable, and time-efficient manner. Sefati et al. [108] also developed an optimization-based algorithm based on FBG tip position feedback to control the CDM when interacting with obstacles and used a data-driven approach to estimate FBG-based position of the CDM from raw

wavelength data [109].

7.7 Recapitulation of Contributions

The author's contributions in this chapter are as follows:

- Proposing and fabricating a novel, large deflection, shape sensor to track the shape of a 35 mm CDM originally designed for a less invasive treatment of osteolysis.
- Conducting calibration experiments for verification of successful sensor fabrication and its integration into the CDM.
- Conducting dynamic shape sensing experiments to evaluate the sensor accuracy in three cases of free bending, bending with an obstacle, and bending with a tool.

The original idea and initial testings for the design of the the shape sensor used in CDM were introduced by Dr. Hao Liu and Dr. Iulian Iordachita. Dr. Ryan Murphy contributed to the shape sensing experiments discussed in section 7.3 by implementing the CDM control software. Dr. Robert Grupp performed the analysis of imaging data and Dr. Sahba Aghajani Pedram contributed to the design of the calibration board showed in Figure 7.6.

Chapter 8

Conclusion

8.1 Summary

This dissertation described the methods and tools developed for multi-physics planning and execution of femoroplasty. Computational models were developed to simulate how bone augmentation effects the biomechanical properties of bone. These models were used to plan the injections for cadaveric specimens and showed the superiority of planed-based augmentation over generic injection strategies. Experimental tests confirmed the findings of simulations and showed significant increase in fracture-related biomechanical properties of the augmented femora as compared to those left intact. The outcomes for the yield load and yield energy improved by respectively 27% and 16% in the current study as compared to the previous generation of the patient-specific plans

while the injection volume was reduced to 9.1 ml. In addition to biomechanical studies for femoroplasty, a heat-transfer model was developed to estimate bone temperatures during augmentation and a conducting cooling mechanism was proposed to lower the risk of thermal damage. Furthermore, a curved injection strategy was introduced and validated in simulations.

Chapter 7 introduced a novel shape sensing technique and evaluated its capability in a 35 mm length continuum manipulator in 3 dynamic cases. Results have shown that the optical sensors can track the tip position with an average error of 0.81 mm. It was also shown that there's no significant difference between the accuracy of free bending with those of bending with a tool inserted. While the immediate application of the manipulator was in hip revision surgery, integration of the device with an injection unit can be used in various augmentation surgeries including a minimally invasive femoroplasty.

8.2 Limitations and Future Work

The following is a list of major limitations and possible future directions towards the ultimate goal of making femoroplasty a clinical orthopaedic procedure:

- The experimental validation of the femoroplasty (discussed in chapter 4) was carried out prior to the development of the robot-assisted framework

to execute the procedure. Therefore, the drilling and injection tasks were performed manually by the author with the aid of a navigation system. As a result, the average shape error between the injected and planned path of cementation remains relatively large in this study (6.2 mm average distance error for the bone cement). Repeat of these tests using the recently developed robotic system can improve the system's accuracy in executing the plan.

- To show the safety of the system, in-vivo tests on animal subjects have been suggested. These tests can not only help investigate the feasibility of the robotics system, it can evaluate the long-term effects of femoroplasty including the risk of thermal damage in a live tissue.

- The heat transfer analysis discussed in chapter 5 involves semi-autonomous segmentation of the bone. Furthermore, the postoperative scans of the bones used in model validation went through a semi-autonomous segmentation for the injected cement. Automating these task could lead to a faster heat transfer analysis for the femoroplasty candidate and easier integration of the results with the proposed planning paradigm. In addition, integration of the heat transfer analysis with the biomechanically-guided plan introduced in 3 can improve the overall safety of the procedure.

- The preliminary simulation of the cooling system demonstrates a promising agreement with in-vitro sawbone experiments. However, in the future, the proposed bone augmentation cooling system need to be experimentally validated through cadaveric femoral augmentation and evaluated against the simulation model.

- We simulated curved injection approach. Future work may include development of the experimental procedure and experimental evaluation of the curved injection approach.

- The developments and modeling in this dissertation focused on the prevention of fracture in osteoporotic hip. These capabilities, however can be extended to the augmentation of other bones susceptible to fracture such as the proximal humerus, the distal radius and the pelvis, as well as treatments involving filling bone defects such as osteosarcoma and osteonecrosis.

Bibliography

[1] J. Who and F. E. Consultation, "Diet, nutrition and the prevention of chronic diseases," *World Health Organ Tech Rep Ser*, vol. 916, no. i-viii, 2003.

[2] G. Campbell, J. Compston, and A. Crisp, *The management of common metabolic bone disorders*. Cambridge University Press, 1993.

[3] C. Cooper, G. Campion, and L. r. Melton, "Hip fractures in the elderly: a world-wide projection," *Osteoporosis international*, vol. 2, no. 6, pp. 285–289, 1992.

[4] M. J. Goldacre, S. E. Roberts, and D. Yeates, "Mortality after admission to hospital with fractured neck of femur: database study," *Bmj*, vol. 325, no. 7369, pp. 868–869, 2002.

[5] R. S. Braithwaite, N. F. Col, and J. B. Wong, "Estimating hip fracture morbidity, mortality and costs," *Journal of the American Geriatrics Society*, vol. 51, no. 3, pp. 364–370, 2003.

BIBLIOGRAPHY

[6] S. Schnell, S. M. Friedman, D. A. Mendelson, K. W. Bingham, and S. L. Kates, "The 1-year mortality of patients treated in a hip fracture program for elders," *Geriatric orthopaedic surgery & rehabilitation*, vol. 1, no. 1, pp. 6–14, 2010.

[7] M. Mariconda, G. Costa, S. Cerbasi, P. Recano, E. Aitanti, M. Gambacorta, and M. Misasi, "The determinants of mortality and morbidity during the year following fracture of the hip: a prospective study," *The bone & joint journal*, vol. 97, no. 3, pp. 383–390, 2015.

[8] J. Magaziner, E. M. Simonsick, T. M. Kashner, J. R. Hebel, and J. E. Kenzora, "Predictors of functional recovery one year following hospital discharge for hip fracture: a prospective study," *Journal of gerontology*, vol. 45, no. 3, pp. M101–M107, 1990.

[9] A. Dinah, "Sequential hip fractures in elderly patients," *Injury*, vol. 33, no. 5, pp. 393–394, 2002.

[10] P. F. Heini, T. Franz, C. Fankhauser, B. Gasser, and R. Ganz, "Femoroplasty-augmentation of mechanical properties in the osteoporotic proximal femur: a biomechanical investigation of pmma reinforcement in cadaver bones," *Clinical biomechanics*, vol. 19, no. 5, pp. 506–512, 2004.

[11] E. G. Sutter, S. J. Wall, S. C. Mears, and S. M. Belkoff, "The effect of

cement placement on augmentation of the osteoporotic proximal femur," *Geriatric Orthopaedic Surgery & Rehabilitation*, vol. 1, no. 1, pp. 22–26, 2010.

[12] J. Beckmann, R. Springorum, E. Vettorazzi, S. Bachmeier, C. Lüring, M. Tingart, K. Püschel, O. Stark, J. Grifka, T. Gehrke *et al.*, "Fracture prevention by femoroplasty—cement augmentation of the proximal femur," *Journal of Orthopaedic Research*, vol. 29, no. 11, pp. 1753–1758, 2011.

[13] P. Varga, J. A. Inzana, J. Schwiedrzik, P. K. Zysset, B. Gueorguiev, M. Blauth, and M. Windolf, "New approaches for cement-based prophylactic augmentation of the osteoporotic proximal femur provide enhanced reinforcement as predicted by non-linear finite element simulations," *Clinical biomechanics*, vol. 44, pp. 7–13, 2017.

[14] A. Freitas, L. C. D. Silva, N. D. V. Godinho, A. Farvardin, M. Armand, and A. P. D. Paula, "Evaluation of a bone reinforcement technique using finite element analysis," *Acta ortopedica brasileira*, vol. 26, no. 1, pp. 59–62, 2018.

[15] E. Basafa and M. Armand, "Subject-specific planning of femoroplasty: a combined evolutionary optimization and particle diffusion model approach," *Journal of biomechanics*, vol. 47, no. 10, pp. 2237–2243, 2014.

BIBLIOGRAPHY

[16] E. Basafa, R. J. Murphy, Y. Otake, M. D. Kutzer, S. M. Belkoff, S. C. Mears, and M. Armand, "Subject-specific planning of femoroplasty: an experimental verification study," *Journal of biomechanics*, vol. 48, no. 1, pp. 59–64, 2015.

[17] J. Compston and A. Crisp, *The Management of Common Metabolic Bone Disorders*. Cambridge University Press, 1993.

[18] B. Gullberg, O. Johnell, and J. Kanis, "World-wide projections for hip fracture," *Osteoporosis international*, vol. 7, no. 5, pp. 407–413, 1997.

[19] W. S. G. on Prevention, M. of Osteoporosis, and W. H. Organization, *Prevention and management of osteoporosis: report of a WHO scientific group*. World Health Organization, 2003, no. 921.

[20] A. Oden, A. Dawson, W. Dere, O. Johnell, B. Jonsson, and J. Kanis, "Lifetime risk of hip fractures is underestimated," *Osteoporosis international*, vol. 8, no. 6, pp. 599–603, 1998.

[21] O. Johnell, J. Kanis, A. Odén, I. Sernbo, I. Redlund-Johnell, C. Petterson, C. De Laet, and B. Jönsson, "Fracture risk following an osteoporotic fracture," *Osteoporosis international*, vol. 15, no. 3, pp. 175–179, 2004.

[22] J. A. Stevens and S. Olson, "Reducing falls and resulting hip fractures

among older women," *Home care provider*, vol. 5, no. 4, pp. 134–141, 2000.

[23] J. A. Kanis, P. Delmas, P. Burckhardt, C. Cooper, and D. o. Torgerson, "Guidelines for diagnosis and management of osteoporosis," *Osteoporosis international*, vol. 7, no. 4, pp. 390–406, 1997.

[24] E. Chrischilles, T. Shireman, and R. Wallace, "Costs and health effects of osteoporotic fractures," *Bone*, vol. 15, no. 4, pp. 377–386, 1994.

[25] A. Farvardin, C. L. Reed, and M. A. Ardini, "Bone loading in the upper extremities (blue)," 2014.

[26] L. Mortensen, P. Charles, P. J. Bekker, J. Digennaro, and C. C. Johnston Jr, "Risedronate increases bone mass in an early postmenopausal population: two years of treatment plus one year of follow-up," *The Journal of Clinical Endocrinology & Metabolism*, vol. 83, no. 2, pp. 396–402, 1998.

[27] S. Boonen, M. R. McClung, R. Eastell, G. El-Hajj Fuleihan, I. P. Barton, and P. Delmas, "Safety and efficacy of risedronate in reducing fracture risk in osteoporotic women aged 80 and older: implications for the use of antiresorptive agents in the old and oldest old," *Journal of the American Geriatrics Society*, vol. 52, no. 11, pp. 1832–1839, 2004.

[28] C. H. Wilkins and S. J. Birge, "Prevention of osteoporotic fractures in the elderly," *The American journal of medicine*, vol. 118, no. 11, pp. 1190–1195, 2005.

[29] T.-P. van Staa, J. A. Kanis, P. Geusens, A. Boonen, H. G. Leufkens, and C. Cooper, "The cost-effectiveness of bisphosphonates in postmenopausal women based on individual long-term fracture risks," *Value in Health*, vol. 10, no. 5, pp. 348–357, 2007.

[30] M. Ishijima, Y. Sakamoto, M. Yamanaka, A. Tokita, K. Kitahara, H. Kaneko, and H. Kurosawa, "Minimum required vitamin d level for optimal increase in bone mineral density with alendronate treatment in osteoporotic women," *Calcified Tissue International*, vol. 85, no. 5, p. 398, 2009.

[31] A. Courtney, E. Wachtel, E. Myers, and W. Hayes, "Effects of loading rate on strength of the proximal femur," *Calcified tissue international*, vol. 55, no. 1, pp. 53–58, 1994.

[32] A. Harada, M. Mizuno, M. Takemura, H. Tokuda, H. Okuizumi, and N. Niino, "Hip fracture prevention trial using hip protectors in japanese nursing homes," *Osteoporosis International*, vol. 12, no. 3, pp. 215–221, 2001.

BIBLIOGRAPHY

[33] I. D. Cameron, "Hip protectors: Prevent fractures but adherence is a problem," 2002.

[34] N. M. van Schoor, J. H. Smit, J. W. Twisk, L. M. Bouter, and P. Lips, "Prevention of hip fractures by external hip protectors: a randomized controlled trial," *Jama*, vol. 289, no. 15, pp. 1957–1962, 2003.

[35] C. R. Kessenich, "Nonpharmacological prevention of osteoporotic fractures," *Clinical Interventions in Aging*, vol. 2, no. 2, p. 263, 2007.

[36] S. R. Cummings, D. M. Black, M. C. Nevitt, W. S. Browner, J. A. Cauley, H. K. Genant, S. R. Mascioli, J. C. Scott, D. G. Seeley, P. Steiger *et al.*, "Appendicular bone density and age predict hip fracture in women," *Jama*, vol. 263, no. 5, pp. 665–668, 1990.

[37] R. Hedlund and U. Lindgren, "Trauma type, age, and gender as determinants of hip fracture," *Journal of orthopaedic research*, vol. 5, no. 2, pp. 242–246, 1987.

[38] T. Pinilla, K. Boardman, M. Bouxsein, E. Myers, and W. Hayes, "Impact direction from a fall influences the failure load of the proximal femur as much as age-related bone loss," *Calcified tissue international*, vol. 58, no. 4, pp. 231–235, 1996.

[39] C. M. Ford, T. M. Keaveny, and W. C. Hayes, "The effect of impact di-

rection on the structural capacity of the proximal femur during falls," *Journal of Bone and Mineral Research*, vol. 11, no. 3, pp. 377–383, 1996.

[40] J. H. Keyak, H. B. Skinner, and J. A. Fleming, "Effect of force direction on femoral fracture load for two types of loading conditions," *Journal of Orthopaedic Research*, vol. 19, no. 4, pp. 539–544, 2001.

[41] M. Bessho, I. Ohnishi, T. Matsumoto, S. Ohashi, J. Matsuyama, K. Tobita, M. Kaneko, and K. Nakamura, "Prediction of proximal femur strength using a ct-based nonlinear finite element method: differences in predicted fracture load and site with changing load and boundary conditions," *Bone*, vol. 45, no. 2, pp. 226–231, 2009.

[42] C. Turner, "Biomechanics of bone: determinants of skeletal fragility and bone quality," *Osteoporosis international*, vol. 13, no. 2, pp. 97–104, 2002.

[43] R. Huiskes, H. Weinans, H. Grootenboer, M. Dalstra, B. Fudala, and T. Slooff, "Adaptive bone-remodeling theory applied to prosthetic-design analysis," *Journal of biomechanics*, pp. 1135–1150, 1987.

[44] P. Varga, L. Hofmann-Fliri, M. Blauth, and M. Windolf, "Prophylactic augmentation of the osteoporotic proximal femur—mission impossible?" *BoneKEy reports*, vol. 5, 2016.

[45] P. M. De Bakker, "Hip fractures: understanding the mechanism and

seeking prevention through prophylactic augmentation of the proximal femur," Ph.D. dissertation, University of British Columbia, 2006.

[46] J. Beckmann, S. J. Ferguson, M. Gebauer, C. Luering, B. Gasser, and P. Heini, "Femoroplasty–augmentation of the proximal femur with a composite bone cement–feasibility, biomechanical properties and osteosynthesis potential," *Medical engineering & physics*, vol. 29, no. 7, pp. 755–764, 2007.

[47] E. G. Sutter, S. C. Mears, and S. M. Belkoff, "A biomechanical evaluation of femoroplasty under simulated fall conditions," *Journal of orthopaedic trauma*, vol. 24, no. 2, p. 95, 2010.

[48] J. Lundskog, "Heat and bone tissue. an experimental investigation of the thermal properties of bone and threshold levels for thermal injury," *Scand J Plast Reconstr Surg*, vol. 9, pp. 72–74, 1972.

[49] A. Eriksson and T. Albrektsson, "Temperature threshold levels for heat-induced bone tissue injury: a vital-microscopic study in the rabbit," *Journal of prosthetic dentistry*, vol. 50, no. 1, pp. 101–107, 1983.

[50] T. Van der Steenhoven, W. Schaasberg, A. de Vries, E. Valstar, and R. Nelissen, "Augmentation with silicone stabilizes proximal femur fractures: an in vitro biomechanical study," *Clinical Biomechanics*, vol. 24, no. 3, pp. 286–290, 2009.

[51] L. Fliri, A. Sermon, D. Wähnert, W. Schmoelz, M. Blauth, and M. Windolf, "Limited v-shaped cement augmentation of the proximal femur to prevent secondary hip fractures," *Journal of biomaterials applications*, vol. 28, no. 1, pp. 136–143, 2013.

[52] E. Basafa, R. J. Murphy, M. D. Kutzer, Y. Otake, and M. Armand, "A particle model for prediction of cement infiltration of cancellous bone in osteoporotic bone augmentation," *PloS one*, vol. 8, no. 6, p. e67958, 2013.

[53] J. Kok, A. Širka, L. Grassi, D. B. Raina, Š. Tarasevičius, M. Tägil, L. Lidgren, and H. Isaksson, "Fracture strength of the proximal femur injected with a calcium sulfate/hydroxyapatite bone substitute," *Clinical Biomechanics*, vol. 63, pp. 172–178, 2019.

[54] M. D. Kutzer, E. Basafa, Y. Otake, and M. Armand, "An automatic injection device for precise cement delivery during osteoporotic bone augmentation," in *International Design Engineering Technical Conferences and Computers and Information in Engineering Conference*, vol. 54808, 2011, pp. 821–827.

[55] Y. Otake, M. Armand, O. Sadowsky, R. S. Armiger, M. D. Kutzer, S. C. Mears, P. Kazanzides, and R. H. Taylor, "An image-guided femoroplasty system: development and initial cadaver studies," in *Medical Imaging*

2010: Visualization, Image-Guided Procedures, and Modeling, vol. 7625. International Society for Optics and Photonics, 2010, p. 76250P.

[56] M. E. Santana Artiles and D. T. Venetsanos, "A new evolutionary optimization method for osteoporotic bone augmentation," *Computer methods in biomechanics and biomedical engineering*, vol. 20, no. 7, pp. 691–700, 2017.

[57] E. Basafa, R. S. Armiger, M. D. Kutzer, S. M. Belkoff, S. C. Mears, and M. Armand, "Patient-specific finite element modeling for femoral bone augmentation," *Medical engineering & physics*, vol. 35, no. 6, pp. 860–865, 2013.

[58] A. Farvardin, E. Basafa, M. Bakhtiarinejad, and M. Armand, "Significance of preoperative planning for prophylactic augmentation of osteoporotic hip: A computational modeling study," *Journal of biomechanics*, vol. 94, pp. 75–81, 2019.

[59] G. Dhondt, *The finite element method for three-dimensional thermomechanical applications*. John Wiley & Sons, 2004.

[60] G. H. Van Lenthe, J. van Den Bergh, A. Hermus, and R. Huiskes, "The prospects of estimating trabecular bone tissue properties from the combination of ultrasound, dual-energy x-ray absorptiometry, microcomputed

tomography, and microfinite element analysis," *Journal of Bone and Mineral Research*, vol. 16, no. 3, pp. 550–555, 2001.

[61] E. F. Morgan, H. H. Bayraktar, and T. M. Keaveny, "Trabecular bone modulus–density relationships depend on anatomic site," *Journal of biomechanics*, vol. 36, no. 7, pp. 897–904, 2003.

[62] T. S. Keller, "Predicting the compressive mechanical behavior of bone," *Journal of biomechanics*, vol. 27, no. 9, pp. 1159–1168, 1994.

[63] T. Van Der Steenhoven, W. Schaasberg, A. De Vries, E. Valstar, and R. Nelissen, "Elastomer femoroplasty prevents hip fracture displacement: in vitro biomechanical study comparing two minimal invasive femoroplasty techniques," *Clinical Biomechanics*, vol. 26, no. 5, pp. 464–469, 2011.

[64] A. Farvardin, M. Bakhtiari Nejad, M. Pozin, and M. Armand, "A biomechanical and thermal analysis for bone augmentation of the proximal femur," in *ASME International Mechanical Engineering Congress and Exposition*, vol. 52026. American Society of Mechanical Engineers, 2018, p. V003T04A061.

[65] K. R. Diller, "Analysis of skin burns," in *Heat transfer in medicine and biology*. Springer, 1985, pp. 85–134.

BIBLIOGRAPHY

[66] K. Buettner, "Effects of extreme heat and cold on human skin. ii. surface temperature, pain and heat conductivity in experiments with radiant heat," *Journal of Applied Physiology*, vol. 3, no. 12, pp. 703–713, 1951.

[67] P. J. Besl and N. D. McKay, "Method for registration of 3-d shapes," in *Sensor fusion IV: control paradigms and data structures*, vol. 1611. International Society for Optics and Photonics, 1992, pp. 586–606.

[68] E. Gautier, K. Ganz, N. Krügel, T. Gill, and R. Ganz, "Anatomy of the medial femoral circumflex artery and its surgical implications," *The Journal of bone and joint surgery. British volume*, vol. 82, no. 5, pp. 679–683, 2000.

[69] S. Sevitt and R. Thompson, "The distribution and anastomoses of arteries supplying the head and neck of the femur," *The Journal of bone and joint surgery. British volume*, vol. 47, no. 3, pp. 560–573, 1965.

[70] M. R. Karagas, G. L. Lu-Yao, J. A. Barrett, M. L. Beach, and J. A. Baron, "Heterogeneity of hip fracture: age, race, sex, and geographic patterns of femoral neck and trochanteric fractures among the us elderly," *American journal of epidemiology*, vol. 143, no. 7, pp. 677–682, 1996.

[71] R. Chavali, R. Resijek, S. K. Knight, and I. S. Choi, "Extending polymerization time of polymethylmethacrylate cement in percutaneous ver-

tebroplasty with ice bath cooling," *American journal of neuroradiology*, vol. 24, no. 3, pp. 545–546, 2003.

[72] J. D. Stroncek, J. L. Shaul, D. Favell, R. S. Hill, B. M. Huber, J. G. Howe, and M. L. Bouxsein, "In vitro injection of osteoporotic cadaveric femurs with a triphasic calcium-based implant confers immediate biomechanical integrity," *Journal of Orthopaedic Research®*, vol. 37, no. 4, pp. 908–915, 2019.

[73] B. Baliga, P. L. Rose, and A. Ahmed, "Thermal modeling of polymerizing polymethylmethacrylate, considering temperature-dependent heat generation," 1992.

[74] E. Hansen, "Modelling heat transfer in a bone–cement–prosthesis system," *Journal of biomechanics*, vol. 36, no. 6, pp. 787–795, 2003.

[75] M. Bakhtiarinejad, A. Farvardin, A. Chamani, and M. Armand, "A conductive cooling scheme for bone augmentation of the proximal femur with pmma: An experimental and finite element study," in *ASME International Mechanical Engineering Congress and Exposition*, vol. 59407. American Society of Mechanical Engineers, 2019, p. V003T04A045.

[76] S. Li, S. Chien, and P.-I. Brånemark, "Heat shock-induced necrosis and apoptosis in osteoblasts," *Journal of orthopaedic research*, vol. 17, no. 6, pp. 891–899, 1999.

[77] A. J. Langdown, N. Tsai, J. Auld, W. R. Walsh, P. Walker, and W. J. Bruce, "The influence of ambient theater temperature on cement setting time," *The Journal of arthroplasty*, vol. 21, no. 3, pp. 381–384, 2006.

[78] P.-L. Lai, C.-L. Tai, I.-M. Chu, T.-S. Fu, L.-H. Chen, and W.-J. Chen, "Hypothermic manipulation of bone cement can extend the handling time during vertebroplasty," *BMC musculoskeletal disorders*, vol. 13, no. 1, pp. 1–6, 2012.

[79] F. Alambeigi, Y. Wang, S. Sefati, C. Gao, R. J. Murphy, I. Iordachita, R. H. Taylor, H. Khanuja, and M. Armand, "A curved-drilling approach in core decompression of the femoral head osteonecrosis using a continuum manipulator," *IEEE Robotics and Automation Letters*, vol. 2, no. 3, pp. 1480–1487, 2017.

[80] A. Farvardin and M. Armand, "Osteoporotic bone augmentation utilizing curved pattern of pmma injection: A combined finite element and optimization investigation," in *ASME International Mechanical Engineering Congress and Exposition*, vol. 59407. American Society of Mechanical Engineers, 2019, p. V003T04A043.

[81] E. Basafa and M. Armand, "Cement placement optimization in femoral augmentation using an evolutionary algorithm," in *International Design Engineering Technical Conferences and Computers and Information in*

Engineering Conference, vol. 55911. American Society of Mechanical Engineers, 2013, p. V004T08A009.

[82] P. Sears and P. E. Dupont, "Inverse kinematics of concentric tube steerable needles," in *Proceedings 2007 IEEE International Conference on Robotics and Automation*. IEEE, 2007, pp. 1887–1892.

[83] R. J. Webster III, J. M. Romano, and N. J. Cowan, "Mechanics of precurved-tube continuum robots," *IEEE Transactions on Robotics*, vol. 25, no. 1, pp. 67–78, 2008.

[84] D. Reynaerts, J. Peirs, and H. Van Brussel, "Shape memory microactuation for a gastro-intestinal intervention system," *Sensors and Actuators A: physical*, vol. 77, no. 2, pp. 157–166, 1999.

[85] K. Ikuta, K. Yamamoto, and K. Sasaki, "Development of remote microsurgery robot and new surgical procedure for deep and narrow space," in *2003 IEEE International Conference on Robotics and Automation (Cat. No. 03CH37422)*, vol. 1. IEEE, 2003, pp. 1103–1108.

[86] D. B. Camarillo, C. F. Milne, C. R. Carlson, M. R. Zinn, and J. K. Salisbury, "Mechanics modeling of tendon-driven continuum manipulators," *IEEE transactions on robotics*, vol. 24, no. 6, pp. 1262–1273, 2008.

[87] C. Taylor and A. Colchester, *Medical Image Computing and Computer-*

Assisted Intervention-MICCAI'99: Second International Conference, Cambridge, UK, September 19-22, 1999, Proceedings. Springer, 2006.

[88] M. D. Kutzer, S. M. Segreti, C. Y. Brown, M. Armand, R. H. Taylor, and S. C. Mears, "Design of a new cable-driven manipulator with a large open lumen: Preliminary applications in the minimally-invasive removal of osteolysis," in *2011 IEEE International Conference on Robotics and Automation*. IEEE, 2011, pp. 2913–2920.

[89] S. M. Segreti, M. D. Kutzer, R. J. Murphy, and M. Armand, "Cable length estimation for a compliant surgical manipulator," in *2012 IEEE International Conference on Robotics and Automation*. IEEE, 2012, pp. 701–708.

[90] R. J. Murphy, M. D. Kutzer, S. M. Segreti, B. C. Lucas, and M. Armand, "Design and kinematic characterization of a surgical manipulator with a focus on treating osteolysis," *Robotica*, vol. 32, no. 6, p. 835, 2014.

[91] Y. Otake, J. W. Stayman, W. Zbijewski, R. J. Murphy, M. Kutzer, R. H. Taylor, J. H. Siewerdsen, and M. Armand, "Model-based cone-beam ct reconstruction for image-guided minimally invasive treatment of hip osteolysis," in *Medical Imaging 2013: Image-Guided Procedures, Robotic Interventions, and Modeling*, vol. 8671. International Society for Optics and Photonics, 2013, p. 86710Y.

[92] A. M. Franz, T. Haidegger, W. Birkfellner, K. Cleary, T. M. Peters, and L. Maier-Hein, "Electromagnetic tracking in medicine—a review of technology, validation, and applications," *IEEE transactions on medical imaging*, vol. 33, no. 8, pp. 1702–1725, 2014.

[93] M. Cianchetti, F. Renda, A. Licofonte, and C. Laschi, "Sensorization of continuum soft robots for reconstructing their spatial configuration," in *2012 4th IEEE RAS & EMBS International Conference on Biomedical Robotics and Biomechatronics (BioRob)*. IEEE, 2012, pp. 634–639.

[94] Y. Shapiro, G. Kósa, and A. Wolf, "Shape tracking of planar hyper-flexible beams via embedded pvdf deflection sensors," *IEEE/ASME Transactions on Mechatronics*, vol. 19, no. 4, pp. 1260–1267, 2014.

[95] Y.-L. Park, S. Elayaperumal, B. Daniel, S. C. Ryu, M. Shin, J. Savall, R. J. Black, B. Moslehi, and M. R. Cutkosky, "Real-time estimation of 3-d needle shape and deflection for mri-guided interventions," *IEEE/ASME Transactions On Mechatronics*, vol. 15, no. 6, pp. 906–915, 2010.

[96] W. N. MacPherson, M. Silva-Lopez, J. S. Barton, A. Moore, J. Jones, D. Zhao, L. Zhang, I. Bennion, N. Metje, D. Chapman *et al.*, "Tunnel monitoring using multicore fibre displacement sensor," *Measurement Science and Technology*, vol. 17, no. 5, p. 1180, 2006.

[97] X. Chen, C. Zhang, D. J. Webb, K. Kalli, and G.-D. Peng, "Highly sensitive

bend sensor based on bragg grating in eccentric core polymer fiber," *IEEE photonics technology letters*, vol. 22, no. 11, pp. 850–852, 2010.

[98] F. Araújo, L. Ferreira, J. Santos, and F. Farahi, "Temperature and strain insensitive bending measurements with d-type fibre bragg gratings," *Measurement Science and Technology*, vol. 12, no. 7, p. 829, 2001.

[99] X. Yi, J. Qian, L. Shen, Y. Zhang, and Z. Zhang, "An innovative 3d colonoscope shape sensing sensor based on fbg sensor array," in *2007 International Conference on Information Acquisition*. IEEE, 2007, pp. 227–232.

[100] R. J. Roesthuis, M. Kemp, J. J. van den Dobbelsteen, and S. Misra, "Three-dimensional needle shape reconstruction using an array of fiber bragg grating sensors," *IEEE/ASME transactions on mechatronics*, vol. 19, no. 4, pp. 1115–1126, 2013.

[101] X. He, J. Handa, P. Gehlbach, R. Taylor, and I. Iordachita, "A submillimetric 3-dof force sensing instrument with integrated fiber bragg grating for retinal microsurgery," *IEEE Transactions on Biomedical Engineering*, vol. 61, no. 2, pp. 522–534, 2013.

[102] J. P. Moore and M. D. Rogge, "Shape sensing using multi-core fiber optic cable and parametric curve solutions," *Optics express*, vol. 20, no. 3, pp. 2967–2973, 2012.

[103] R. J. Murphy, Y. Otake, R. H. Taylor, and M. Armand, "Predicting kinematic configuration from string length for a snake-like manipulator not exhibiting constant curvature bending," in *2014 IEEE/RSJ International Conference on Intelligent Robots and Systems*. IEEE, 2014, pp. 3515–3521.

[104] F. Alambeigi, S. Sefati, R. J. Murphy, I. Iordachita, and M. Armand, "Design and characterization of a debriding tool in robot-assisted treatment of osteolysis," in *2016 IEEE International Conference on Robotics and Automation (ICRA)*. IEEE, 2016, pp. 5664–5669.

[105] Y. Otake, R. J. Murphy, M. Kutzer, R. H. Taylor, and M. Armand, "Piecewise-rigid 2d-3d registration for pose estimation of snake-like manipulator using an intraoperative x-ray projection," in *Medical Imaging 2014: Image-Guided Procedures, Robotic Interventions, and Modeling*, vol. 9036. International Society for Optics and Photonics, 2014, p. 90360Q.

[106] R. J. Murphy, Y. Otake, K. C. Wolfe, R. H. Taylor, and M. Armand, "Effects of tools inserted through snake-like surgical manipulators," in *2014 36th Annual International Conference of the IEEE Engineering in Medicine and Biology Society*. IEEE, 2014, pp. 6854–6858.

[107] S. Sefati, M. Pozin, F. Alambeigi, I. Iordachita, R. H. Taylor, and M. Ar-

mand, “A highly sensitive fiber bragg grating shape sensor for continuum manipulators with large deflections,” in *2017 IEEE SENSORS*. IEEE, 2017, pp. 1–3.

[108] S. Sefati, R. J. Murphy, F. Alambeigi, M. Pozin, I. Iordachita, R. H. Taylor, and M. Armand, “Fbg-based control of a continuum manipulator interacting with obstacles,” in *2018 IEEE/RSJ International Conference on Intelligent Robots and Systems (IROS)*. IEEE, 2018, pp. 6477–6483.

[109] S. Sefati, R. Hegeman, F. Alambeigi, I. Iordachita, and M. Armand, “Fbg-based position estimation of highly deformable continuum manipulators: Model-dependent vs. data-driven approaches,” in *2019 International Symposium on Medical Robotics (ISMR)*. IEEE, 2019, pp. 1–6.

Vita

Amirhossein Farvardin received a B.S. degree in Biomedical Engineering from the Worcester Polytechnic Institute in 2014 and a M.S.E degree in Robotics from Johns Hopkins University in 2017. He is currently a Ph.D. candidate at the Department of Mechanical Engineering, working with Prof. Mehran Armand in the Biomechanical and Image-Guided Surgical Systems (BIGSS) laboratory, part of the Laboratory for Computational Sensing and Robotics (LCSR). His research interests include computer-assisted surgery, biomechanics, robotics and surgical simulation. Amirhossein was supported through a Johns Hopkins Applied Physics Laboratory Graduate Fellowship from 2016 until 2020. Following graduation, he will continue research in the area of computer-assisted orthopaedic surgery and robotics at the department of Orthopaedic Surgery, Johns Hopkins Medical Institutions.